

Seismic data correction and dynamic impact evaluation for assessing coal burst risks in underground mines

Author:

Wang, Changbin

Publication Date:

2021

DOI:

<https://doi.org/10.26190/unsworks/1617>

License:

<https://creativecommons.org/licenses/by/4.0/>

Link to license to see what you are allowed to do with this resource.

Downloaded from <http://hdl.handle.net/1959.4/100017> in <https://unsworks.unsw.edu.au> on 2024-04-25

UNSW



Seismic data correction and dynamic impact evaluation for assessing coal burst risks in underground mines

Changbin Wang

A thesis in fulfilment of the requirements for the degree of
Doctor of Philosophy

*School of Minerals and Energy Resources Engineering
University of New South Wales*

Faculty of Engineering

September 2021

1. THESIS TITLE & ABSTRACT

Thesis Title

Seismic data correction and dynamic impact evaluation for assessing coal burst risks in underground mines

Thesis Abstract

Coal bursts and rockbursts are one of the most formidable mining hazards in underground mines, causing the dynamic failure of coal and/or rock mass and violent ejection of material into mine openings. The mechanisms of coal bursts and rockbursts are not yet fully understood because of the large variability and uncertainty in the causal factors.

The seismic monitoring technique has been widely used in burst-prone mines, which provides a powerful means to detect dynamic rock failure and understand the burst damage mechanism. However, as dynamic impacts in underground coal mines have been rarely studied, the triggering mechanism of seismic waves for coal bursts is poorly understood. Apart from that, the recorded seismic data may have high location errors and low data integrity, which significantly limits the accuracy of the seismic methods.

Therefore, this thesis investigated the dynamic impacts of mining-induced seismicity in underground mines and enhanced the seismic data quality in assessing the associated risks. The study of this thesis is based on seismic data in a burst-prone coal mine in China. The ground motion characteristics of the study longwall indicate that coal bursts are usually triggered by the dynamic impacts when the coal and rock mass are already under critical stress levels. The roadway zones that have experienced more intensive ground motions are more susceptible to coal bursts. The location errors of the seismic monitoring system were evaluated, which are highly anisotropic and vary along with the geophone movement. A modified seismic clustering method was proposed to eliminate the influence of location errors on the results. The detection probabilities of the seismic monitoring system were investigated to study the data integrity in the longwall. The detection probability results were used to correct the data integrity, which shows more event counts and seismic energy release in the longwall. The "reinforced seismic data" concept was proposed to correct location errors in the raw seismic data and improve data integrity. It is found that seismic energy has a strong correlation with coal burst damage, which can be used as an essential precursor of impending burst hazards.

The outcome of this thesis can provide insights on the burst damage mechanism and evaluation of seismic data quality in underground coal mines. The proposed seismic methods can be used individually or together to improve burst hazard forecasting.

2. ORIGINALITY, COPYRIGHT AND AUTHENTICITY STATEMENTS

ORIGINALITY STATEMENT

☒ I hereby declare that this submission is my own work and to the best of my knowledge it contains no materials previously published or written by another person, or substantial proportions of material which have been accepted for the award of any other degree or diploma at UNSW or any other educational institution, except where due acknowledgement is made in the thesis. Any contribution made to the research by others, with whom I have worked at UNSW or elsewhere, is explicitly acknowledged in the thesis. I also declare that the intellectual content of this thesis is the product of my own work, except to the extent that assistance from others in the project's design and conception or in style, presentation and linguistic expression is acknowledged.

COPYRIGHT STATEMENT

☒ I hereby grant the University of New South Wales or its agents a non-exclusive licence to archive and to make available (including to members of the public) my thesis or dissertation in whole or part in the University libraries in all forms of media, now or here after known. I acknowledge that I retain all intellectual property rights which subsist in my thesis or dissertation, such as copyright and patent rights, subject to applicable law. I also retain the right to use all or part of my thesis or dissertation in future works (such as articles or books).

For any substantial portions of copyright material used in this thesis, written permission for use has been obtained, or the copyright material is removed from the final public version of the thesis.

AUTHENTICITY STATEMENT

☒ I certify that the Library deposit digital copy is a direct equivalent of the final officially approved version of my thesis.

3. INCLUSION OF PUBLICATIONS STATEMENT

UNSW is supportive of candidates publishing their research results during their candidature as detailed in the UNSW Thesis Examination Procedure.

Publications can be used in the candidate's thesis in lieu of a Chapter provided:

- The candidate contributed **greater than 50%** of the content in the publication and are the "primary author", i.e. they were responsible primarily for the planning, execution and preparation of the work for publication.
- The candidate has obtained approval to include the publication in their thesis in lieu of a Chapter from their Supervisor and Postgraduate Coordinator.
- The publication is not subject to any obligations or contractual agreements with a third party that would constrain its inclusion in the thesis.

☒ The candidate has declared that **their thesis has publications - either published or submitted for publication - incorporated into it in lieu of a Chapter/s. Details of these publications are provided below.**

Publication Details #1

Full Title:	Location error based seismic cluster analysis and its application to burst damage assessment in underground coal mines
Authors:	Changbin Wang, Guangyao Si, Chengguo Zhang, Anye Cao, Ismet Canbulat
Journal or Book Name:	International Journal of Rock Mechanics and Mining Sciences
Volume/Page Numbers:	143: 104784
Date Accepted/Published:	22 April 2021
Status:	published
The Candidate's Contribution to the Work:	Changbin Wang is the method provider also responsible for the paper writing.
Location of the work in the thesis and/or how the work is incorporated in the thesis:	The main content of this paper was used in Chapter 5 of the thesis.

Publication Details #2

Full Title:	A statistical method to assess the data integrity and reliability of seismic monitoring systems in underground mines
Authors:	Changbin Wang, Guangyao Si, Chengguo Zhang, Anye Cao, Ismet Canbulat
Journal or Book Name:	Rock Mechanics and Rock Engineering
Volume/Page Numbers:	Available online
Date Accepted/Published:	28 July 2021
Status:	published
The Candidate's Contribution to the Work:	Changbin Wang is the method provider also responsible for the paper writing.
Location of the work in the thesis and/or how the work is incorporated in the thesis:	The main content of this paper was used in Chapter 6 of the thesis.

Publication Details #3

Full Title:	A new method to assess coal burst risks using dynamic and static loading analysis
Authors:	Changbin Wang, Anye Cao, Chengguo Zhang, Ismet Canbulat
Journal or Book Name:	Rock Mechanics and Rock Engineering
Volume/Page Numbers:	53: 1113–1128
Date Accepted/Published:	7 September 2019
Status:	published
The Candidate's Contribution to the Work:	Changbin Wang is the method provider also responsible for the paper writing.
Location of the work in the thesis and/or how the work is incorporated in the thesis:	Some contents of this paper were used in Chapter 2 of the thesis.

Publication Details #4

Full Title:	Ground motion characteristics and their cumulative impacts to burst risks in underground coal mines
Authors:	Changbin Wang, Guangyao Si, Chengguo Zhang, Anye Cao, Ismet Canbulat
Journal or Book Name:	geomechanics and geophysics for geo-energy and geo-resources
Volume/Page Numbers:	
Date Accepted/Published:	
Status:	submitted
The Candidate's Contribution to the Work:	Changbin Wang is the method provider also responsible for the paper writing.
Location of the work in the thesis and/or how the work is incorporated in the thesis:	The main content of this paper was used in Chapter 4 of the thesis.

Publication Details #5

Full Title:	Ground motion characteristics in an underground burst-prone coal mine
Authors:	Changbin Wang, Guangyao Si, Chengguo Zhang, Ismet Canbulat
Journal or Book Name:	39th International Conference on Ground Control in Mining
Volume/Page Numbers:	64–68
Date Accepted/Published:	
Status:	published
The Candidate's Contribution to the Work:	Changbin Wang is the method provider also responsible for the paper writing.
Location of the work in the thesis and/or how the work is incorporated in the thesis:	The main content of this paper was used in Chapter 4 of the thesis.

Publication Details #6

Full Title:	Intensity quantification of coal and rock burst risk - a review
Authors:	Changbin Wang, Chengguo Zhang, Ismet Canbulat, Dongsheng Zhang, Gangwei Fan
Journal or Book Name:	Proceedings The Fourth Australasian Ground Control in Mining Conference (AusRock)
Volume/Page Numbers:	223-233
Date Accepted/Published:	
Status:	published
The Candidate's Contribution to the Work:	Changbin Wang is the method provider also responsible for the paper writing.
Location of the work in the thesis and/or how the work is incorporated in the thesis:	The main content of this paper was used in Chapter 1 and 2 of the thesis.

Publication Details #7

Full Title:	Variation of seismicity using reinforced seismic data for coal burst risk assessment in underground mines
Authors:	Changbin Wang, Guangyao Si, Chengguo Zhang, Anye Cao, Ismet Canbulat
Journal or Book Name:	International Journal of Rock Mechanics and Mining Sciences
Volume/Page Numbers:	
Date Accepted/Published:	
Status:	submitted
The Candidate's Contribution to the Work:	Changbin Wang is the method provider also responsible for the paper writing.
Location of the work in the thesis and/or how the work is incorporated in the thesis:	The main content of this paper was used in Chapter 7 of the thesis.

Candidate's Declaration



I confirm that where I have used a publication in lieu of a chapter, the listed publication(s) above meet(s) the requirements to be included in the thesis. I also declare that I have complied with the Thesis Examination Procedure.

Abstract

With the increasing mining depth in recent decades, the high in-situ stress and challenging environments in deep underground mines result in multiple mining hazards. Coal bursts and rockbursts are one of the most formidable mining hazards in underground mines, causing the dynamic failure of coal and/or rock mass and violent ejections of material into mine openings. After more than half a century of research, the mechanisms of coal bursts and rockbursts are not yet fully understood because of the large variability and uncertainty in the causal factors.

Seismic monitoring is the most popular technique to help forecast, prevent and control burst hazards. It uses seismic waves generated from coal and rock mass to locate internal damage, which provides a powerful means to detect dynamic rock failure and understand the burst damage mechanism. The dynamic impact from seismic waves is an essential cause of rock failure. However, as dynamic impacts in underground coal mines have been rarely studied, the triggering mechanism of seismic waves for coal bursts is poorly understood. Apart from that, due to the complex underground environment, the recorded seismic data may have high location errors and low data integrity, which significantly limits the accuracy of the seismic methods.

Therefore, this thesis investigated dynamic impacts of mining-induced seismicity in underground mines and enhanced the seismic data quality in assessing the associated risks. Based on seismic data in a burst-prone coal mine in China, the research investigated the ground motion characteristics in the target longwall blocks. It is found that coal bursts are usually triggered by the dynamic impacts when the coal and rock mass are already under critical stress levels. The roadway zones that have experienced more intensive ground motions are more susceptible to coal bursts.

The characteristics of location error in the studied longwall were investigated, and a modified seismic clustering method was proposed to assess burst risks. The result revealed that location errors are highly anisotropic and vary along with the geophone movement. The proposed seismic clustering method that considers the influence of location errors had a strong correlation with coal burst damage.

The characteristics of seismic data integrity in the studied longwall were investigated by assessing the detection probabilities of the seismic monitoring system. Geophones had various capabilities to detect seismic events at different locations and energy magnitudes. Based on the detection probability results, a method was proposed to correct the integrity of seismic data, which shows more event counts and seismic energy release in front of the longwall face.

The concept of “reinforced seismic data” was proposed to correct location errors in the raw seismic data and improve data integrity. The relationship between the spatial variation of seismicity and burst risks was also investigated by using reinforced seismic data. It is found that seismic energy has a strong correlation with coal burst damage, which can be used as an essential precursor of impending burst hazards.

The outcome of this thesis can provide insights on the burst damage mechanism and evaluation of seismic data quality in underground coal mines. The proposed seismic methods identify burst risks in terms of ground motions, seismic clusters and variations of seismicity, which can be used individually or together to improve burst hazard forecasting.

Acknowledgements

First and foremost, I wish to express my sincere gratitude to my esteemed supervisors: Professor Ismet Canbulat, Dr Guangyao Si, Dr Chengguo Zhang and Professor Bruce Hebblewhite. Their supervision, support and guidance were invaluable during my PhD study. Their profound knowledge and extensive experience have inspired me throughout my academic research. I would also like to thank Professor Anye Cao and Associate Professor Wu Cai from China University of Mining and Technology for their great help in my research. I also acknowledge the financial support of the University of New South Wales and the China Scholarship Council.

My sincere thanks to my dear friends in the School of Minerals and Energy Resources Engineering: Dr Chunchen Wei, Dr Onur Vardar, Dr Faham Tahmasebinia, Mr Feng Zhang, Dr Hao Zhai, Dr Huasheng Lin, Mr Yu Shu, Mr Xu Li and Mr Sarvesh Singh. Their help and care were invaluable for my research at UNSW. In addition, I would like to thank my other friends, who have accompanied me through a beautiful life in Australia. They are: Dr Mingzhe Wang, Dr Jing Li, Dr Lie Kong, Dr Hongyan Quan, Dr Junjie Shi, Dr Jiahui Qian, Dr Yueyi Pan, Dr Lei Bai, Dr Qian Zhang, Mr Gaochao Lin and Miss Rong Mu.

Finally, I am extremely grateful to my parents, Mr Zhong Wang and Mrs Fang Li, for their love, encouragement and support.

Table of Contents

Abstract	i
Acknowledgements	iii
Table of Contents	iv
List of Figures	viii
List of Tables	xvi
List of Symbols	xvii
List of Publications	xx
Chapter 1. Introduction.....	1
1.1 Background	1
1.1.1 Dynamic impacts from seismic waves	3
1.1.2 Defective seismic data.....	3
1.1.3 Seismic precursors prior to coal bursts	4
1.2 Objectives and scope of the research	5
1.3 Thesis structure	6
Chapter 2. Literature review	8
2.1 Introduction	8
2.2 Mining-induced seismicity and burst damage classification	8
2.2.1 Mining-induced seismicity	8
2.2.2 Classifications of coal burst and rockburst damage.....	13
2.3 Dynamic impacts of seismicity	20
2.3.1 Near-field and far-field zones of a seismic source	20
2.3.2 Ground motions.....	23
2.3.3 Ejection velocity	27
2.4 Variations of mining-induced seismicity and applications in assessing dynamic failure risks.....	30
2.4.1 Event counts and seismic energy variations	30

2.4.2	Seismic clusters	35
2.5	Seismic monitoring capability.....	40
2.5.1	Location errors	40
2.5.2	Completeness of seismicity catalogue	42
2.6	Summary	46
Chapter 3. Geological and seismic characteristics of the study site-Huating Coal Mine.....		49
3.1	Introduction	49
3.2	Geological and mining conditions	49
3.3	Seismic monitoring system	52
3.4	Mining-induced seismicity	55
3.5	Coal bursts	57
3.6	Summary	61
Chapter 4. Ground motion characteristics and their cumulative impacts on coal burst risks in underground mines.....		63
4.1	Introduction	64
4.2	Background	65
4.2.1	Ground motions in far-field zones.....	65
4.2.2	Ground motions in near-field zones.....	66
4.3	Ground motion characteristics in LW250105.....	67
4.3.1	Ground motions in far-field zones.....	67
4.3.2	Ground motions in near-field zones.....	72
4.3.3	Dynamic stresses	75
4.4	Correlation between historical ground motions and burst damage	77
4.4.1	Number of high ground motions	77
4.4.2	Back analysis.....	78
4.5	Summary	82
Chapter 5. Location error based seismic cluster analysis and its application to coal burst assessment		83
5.1	Introduction	84

5.2	Location error assessment	85
5.2.1	Location error emulation test.....	85
5.2.2	Location error analysis	88
5.3	Seismic clustering based on source radius and location error corrections.....	93
5.3.1	Location error correction and clustering possibility	93
5.3.2	Number of possible clustered events ($NPCE$)	94
5.4	Seismic clusters and coal burst damage.....	99
5.5	Summary	106
Chapter 6. A statistical method to assess data integrity and reliability of seismic monitoring systems.....		108
6.1	Introduction	109
6.2	Methodology of the probability of detecting earthquakes (PDE).....	111
6.2.1	Wave picking capability of individual geophones (P_D).....	111
6.2.2	Event detection probability of the monitoring system (P_E)	117
6.2.3	Correction of event counts and seismic energy based on detection probability	120
6.3	Detection probability assessment in LW250105.....	121
6.3.1	Wave picking capabilities of geophones (P_D).....	121
6.3.2	Event detection probability of the seismic monitoring system (P_E).....	124
6.3.3	Energy magnitude distribution at different event detection probabilities.....	128
6.4	Discussion	130
6.4.1	Seismic data correction in LW250105.....	130
6.4.2	Determination of the minimum number of sample events at a grid point (N_{min}).....	134
6.5	Detection probability evolution of the seismic monitoring system in LW250105	136
6.6	Summary	140

Chapter 7. Spatial variation of seismicity using reinforced seismic data and its application in coal burst prediction	142
7.1 Introduction	142
7.2 Methodology	143
7.2.1 Potential damage zone (<i>PDZ</i>)	143
7.2.2 Reinforced seismic data	146
7.3 Spatial variation of seismicity in LW250105 using reinforced seismic data	149
7.3.1 <i>PDZ</i> identification in LW250105	149
7.3.2 Results of spatial variation of seismicity using reinforced seismic data	152
7.3.3 Guidelines for method application	157
7.4 Summary	158
Chapter 8. Conclusions and recommendations	160
8.1 Conclusions	160
8.2 Recommendations for future research	164
References	167

List of Figures

Figure 1-1 A schematic diagram of seismic monitoring applied in longwall coal extraction to trace shear slipping along a failure plane (Cai et al., 2019). The blue line denotes a seismic wave, and the yellow rectangle denotes a seismic sensor.....	2
Figure 2-1 Model of a shear slipping along a plane (Shearer, 2009).....	9
Figure 2-2 Diagram of the relationship between shear stress, resisting stress (friction) and displacement of a fault plane during an earthquake (McGarr, 1993). The shaded area is the dissipated energy during the process, and the stippled area is the radiated seismic energy available for ground motions.	11
Figure 2-3 Principal stresses around (a) thrust fault (vertical plane), (b) normal fault (vertical plane) and (c) strike-slip fault (horizontal plane) (Jaeger et al., 2009)	12
Figure 2-4 Mohr–Coulomb diagram illustrating the reactivation of (a) thrust fault, (b) normal fault and (c) strike-slip fault (Jaeger et al., 2009)	12
Figure 2-5 A simplified model of recurring earthquakes. τ_1 and τ_2 are the shear stress levels before and after earthquakes, respectively (Shearer, 2009).	13
Figure 2-6 Two types of coal burst classified in the Ostrava-Karvina Coal Field (Ptáček, 2017).....	15
Figure 2-7 Fault induced coal burst mechanism: (a) the mining operation is far away from the fault, (b) the mining operation is approaching the fault, (c) the mining operation is leaving the fault, and (d) the direction of the mining operation is parallel to the fault (Cai et al., 2020b).....	16
Figure 2-8 Visualisation of stable and unstable states of equilibrium in rock mass (Galvin, 2016).....	17
Figure 2-9 Stress–strain curves (blue line) of the rock mass with (a) controlled failure and (b) uncontrolled failure. The red line is the stiffness of the loading system (Galvin, 2016).	18
Figure 2-10 Complete load–deformation curves with different strain rates for (a) sandstone (Bieniawski, 1970) and (b) Tennessee marble (Peng, 1973)	19

Figure 2-11 Characteristics of displacement and ground motion in rock mass at the near-field and far-field zones, modified from Shearer (2009).....	21
Figure 2-12 Schematic diagram of a compressive seismic wave superimposed on a tunnel (Roberts and Brummer, 1988)	24
Figure 2-13 A schematic diagram of slab flexure (McGarr, 1997). Slab thickness is h , slab length is L , and the loaded stress is S	28
Figure 2-14 A schematic diagram of the ejection path of a rock fragment on the side wall (Tannant et al., 1993). D and H are the horizontal and vertical distances of the ejected material, respectively, θ is the initial angle of motion measured upwards from the horizontal plane, and g is the gravitational acceleration.....	29
Figure 2-15 Variation of seismic event counts before a rockburst in a hard rock mine (Brady and Leighton, 1977).....	32
Figure 2-16 Variation of event count and seismic energy before a coal burst in an underground coal mine (Cao et al., 2016).....	32
Figure 2-17 Density contours of seismic event counts around a tunnel (Liu et al., 2018)	33
Figure 2-18 Spatial evolution of seismic energy before a coal burst occurred in a longwall (Wang et al., 2018).....	34
Figure 2-19 Four micro-seismic examples of rock mass failure (Vasak et al., 2004): (a) stress related, (b) excavation intersecting weak planes, (c) weak plane propagation, (d) rock bridge failure. The black rectangle is the excavation boundary, red dots are induced seismic events, and the orange line is the discontinuity in the rock mass.....	36
Figure 2-20 Relationship of the cluster index function with the distance between two events and the source size (Falmagne, 2002).....	37
Figure 2-21 An example of data clusters using DBSCAN (Rezaei, 2016)	38
Figure 2-22 Mining-induced seismicity in a tested mine clustered by the modified DBSCAN method (Woodward et al., 2018). Blue dots are the noise events, dots with other colours are events in different clustering groups.	38
Figure 2-23 Five seismic clusters identified in the stoping area by using the CSEC method (Hudyma, 2008)	39

Figure 2-24 An example of the temporal evolution of seismic clusters by using the sequential spatial clustering method (Cortolezzis and Hudyma, 2018)	39
Figure 2-25 Three sensor arrays in a tunnel: (a) axial-extended array, (b) lateral extended array, and (c) twin-tube array (Zhang et al. (2019)	41
Figure 2-26 <i>FMD</i> and cumulative <i>FMD</i> of an earthquake catalogue recorded by the Northern California Seismic Network (Woessner and Wiemer, 2005)	44
Figure 2-27 Cumulative <i>FMD</i> in an Australian underground mine using (a) all seismic events and (b) the seismic events from two different sources (Woodward and Tierney, 2017)	46
Figure 3-1 Stratigraphic column in LW250105 area (Wang et al., 2021)	50
Figure 3-2 An example illustrating the goaf-side entry driving (GED) method (Wu et al., 2018)	51
Figure 3-3 LW250105 layout and geophone distribution in Huating Coal Mine (Wang et al., 2021)	52
Figure 3-4 Distribution of roadway geophones in LW250105 from April to December 2014. The grey zone is the longwall chainage during the period.	54
Figure 3-5 Examples of (a) truncated waveforms captured by a roadway geophone and (b) blurred waveforms captured by a distant geophone	55
Figure 3-6 Percentage of seismic events at different energy levels in LW250105 recorded during 2014	56
Figure 3-7 Spatial distribution of seismic events with different energy levels in LW250105	57
Figure 3-8 Number of daily seismic events and seismic energy ahead of LW250105 face during 2014 (with a distance interval of 20 m)	57
Figure 3-9 Spatial distribution of coal bursts and burst damage zones during the retreat of LW250105 in 2014. The blue line links the epicentres of the coal bursts and the corresponding burst damage zones.	59
Figure 4-1 (a) Schematic diagram of source mechanism of a seismic event, <i>ppv</i> readings in different geophones and ground motion response in the roadway, (b) Example of <i>ppvR</i> results of a seismic event from different geophones	66

Figure 4-2 Relationship between seismic energy and $ppvR$ of seismic events and coal bursts in LW250105	68
Figure 4-3 Average ground motion intensities in far-field zones of seismic events in (a) LW250105 and (b) gold mines in Klerksdorp Goldfield (Glazer, 2018). Red dashed line indicates the overlapping area of (a) and (b)	69
Figure 4-4 Relationship between $ppvR$ and seismic energy of LW250105 coal bursts (marked with red), coal bursts in Upper Silesian Coal Basin, referred as USCB (marked with green) and strong seismic events in hard rock mines (marked with blue)	70
Figure 4-5 Far-field ground motions from seismic events (marked as blue dots) and coal bursts (marked as red dots) at different event–roadway distances (d)	72
Figure 4-6 Relationship between seismic energy and near-field ground motions. The blue line denotes the upper bound limit of $ppv_{near-field}$ at 90% confidence.	73
Figure 4-7 Ground motions in near-field zones of LW250105 coal bursts (red dots) and East Rand Proprietary Mines in South Africa, referred as ERPM (blue dots)	74
Figure 4-8 Average far-field and near-field ground motions and number of events at different event–roadway distances.....	75
Figure 4-9 Ground motions and equivalent dynamic stresses that seismic events impart to LW250105 roadway	76
Figure 4-10 $NHGM$ distribution on the tailgate before coal burst occurred on 6 September 2014. Red line marks the burst damage position.	78
Figure 4-11 R_{NHGM} distributions in LW250105 tailgate before coal bursts occurred	80
Figure 4-12 R_{NHGM} in burst damage zones in LW250105	80
Figure 4-13 Magnitude of completeness before the occurrence of coal bursts in LW250105	81
Figure 5-1 (a) Example of 2000 emulation testing results of a point at $X=-850$ m and $Y=400$ m. δ_L is 20.05 m, and a and b of the error ellipse are 29 m and 15 m, respectively. (b) Probability density of Gaussian distribution based on emulation test results of (a).	88

Figure 5-2 Roadway geophones layout, δ_L contours (unit: m) and error ellipses distribution in four time periods during LW250105 recovery in 2014. The blue square is a roadway geophone, the arrow is the mining direction and the longwall chainage during the time period, and the shadow area is the goaf behind the panel face.....	92
Figure 5-3 Three cases for a pair of seismic events to be considered in clustering probability analysis. Two seismic events at their original locations are represented by filled dots, and their distance is d . The dashed circle shows the zone with two times the source radius ($2r_0$) of each seismic event. After relocating, the new locations of the seismic events are represented by unfilled dots, and their distance becomes d'	94
Figure 5-4 An example of the $NPCE$ calculation for seismic event #0 (marked in red). Blue dots are the seismic events adjacent to event #0. The ellipse is the location error ellipse of the seismic event, a filled dot is the original event location, an unfilled dot is the possible location of the event within the error ellipse.....	96
Figure 5-5 An example of $NPCE$ results with different $\eta c_{threshold}$	97
Figure 5-6 Examples of clustering results of LW250105 without (left) and with (right) considering location errors. The red zone is the coal burst damage which occurred in the next week, and the contours are the number of clustered events.	99
Figure 5-7 Results of (a) $NPCE$ scatter, (b) $NPCE$ contour and (c) R_{NPCE} for 9-15 September 2014	101
Figure 5-8 Coal burst damage zones and the latest tailgate R_{NPCE} distribution ahead of the longwall face in LW250105. The red zone is the coal burst damage zone. The blue line is the longwall face position.	102
Figure 5-9 Minimum, average and maximum R_{NPCE} in burst damage zones in LW250105	103
Figure 5-10 Distances from the longwall face to the nearest geophone (triangle) and damage zone (circle). The filled zone indicates coal bursts with maximum R_{NPCE} lower than 0.5. The arrow means the first coal burst before geophone location changes.....	104
Figure 5-11 Accuracy (marked as red columns) and efficiency (marked as blue line) for hazard prediction when using different R_{NPCE} as the risk threshold in LW250105	105

Figure 6-1 Example of pickable (a) and unpickable (b) seismic waves.....	112
Figure 6-2 Example of (a) D-M map showing distributions of picked (marked with green) and unpicked (marked with red) seismic events by a geophone, (b) P_D distribution calculated from (a), and (c) P_D distribution after applying physical constraints	112
Figure 6-3 In a D-M map: (a) distance (R_M) between two seismic events (marked in blue), (b) selected seismic events (marked in red) for P_D calculation at a point ($\log E_i, R_i$) within the radius R_{MT} (marked in blue dashed lines), and (c) selected seismic events for P_D calculation at a point ($\log E_i, R_i$) within the radius R_{MT} and the extended zone (marked in yellow). Dashed dots are the unselected events.....	114
Figure 6-4 Flow chart of sample events selecting procedure for $P_D(\log E_i, R_i)$ calculation	116
Figure 6-5 Event detection probability of a seismic event by three geophones in a monitoring system with five geophones (P_E^3). (a) P_D of individual geophones for a seismic event. (b) The second geophone combination (geophones #1, #2 and #4) is taken as an example to calculate the probability of the seismic event picked by them. The green-shaded zone marks the parameters of geophones that have picked the seismic waves (geophones #1, #2 and #4), and the yellow-shaded zone marks the parameters of geophones that have not picked the seismic waves (geophones #3 and #5). (c) Calculation of the event detection probability by geophones #1, #2 and #4 ($P_E^{3(k=2)}$) and the summation of detecting probability by three geophones (P_E^3).	119
Figure 6-6 Distribution of picked (marked with green) and unpicked (marked with red) events in the D-M map of five active geophones in LW250105 ...	122
Figure 6-7 Wave picking capability P_D of five active geophones in LW250105...	124
Figure 6-8 Detection probability P_E for seismic events with different energy magnitudes in LW250105. White squares denote active roadway geophones, the shaded zone is the retreat area, and the arrow indicates the mining direction.	126
Figure 6-9 Event detection probability in LW250105 at specific locations of (I) solid coal, (II) ahead of the retreat area, (III) retreat area, (IV) behind the longwall face in the goaf, and (V) with the goaf of the previous longwall panel	127

Figure 6-10 Distribution of energy magnitudes with P_E thresholds of 100%, 95% and 90%. White squares denote the active roadway geophones, the shaded zone is the chainage zone, and the arrow indicates the mining direction.	129
Figure 6-11 FMD and cumulative FMD of seismic events in LW250105 from 1 July to 29 September 2014. Energy magnitude of completeness (m_c), marked by a red dot, is calculated using the maximum curvature method.....	130
Figure 6-12 Spatial distribution of seismic events in LW250105 during September 2014 based on (a) original data, (b) data after correction, and (c) data over m_c . Shaded area indicates the chainage zone, and arrow indicates the mining direction.	132
Figure 6-13 (a) Average daily counts and (b) daily seismic energy of seismic events ahead of LW250105 face during September 2014 based on (i) original data (black line), (ii) data over m_c (blue line) and (iii) corrected data (red line).	133
Figure 6-14 Average <i>Cumulative Grids Number Ratio</i> R_C (black line) and <i>Sample Events Ratio</i> R_T (red line) of the six active geophones in LW250105	135
Figure 6-15 Recalculation of P_D results for geophone #7 after its relocation in LW250105 from 7 April to 12 May 2014.....	137
Figure 6-16 P_E distribution in LW250105 during 2014 for the seismic events with $\log E=5$ before (a) and after (b) the relocation of geophone #2.....	138
Figure 6-17 P_E distribution in LW250105 during 2014 for the seismic events with $\log E=5$ before (a) and after (b) the relocation of geophone #13 and geophone #16	138
Figure 6-18 Similarity of P_E results for the seismic monitoring system in LW250105 for 12 April to 8 December 2014. Red dots are the last PE result before the relocation of geophones.	139
Figure 7-1 (a) R_{NPCE} and (b) $\max R_{NPCE}$ results in LW250105 for 28 May to 3 June 2014. The grey zone is the goaf behind the longwall face.	144
Figure 7-2 PDZ identification in LW250105 for 5–11 November using the (a) R_{NPCE} results and (b) $\max R_{NPCE}$ results. The red zone indicates a roadway section damaged by an impending coal burst which occurred in the following week. Black rectangles outline the identified PDZ . The grey zone is the goaf.....	145

Figure 7-3 Event count distributions in LW250105 on 21 September 2014 using reinforced seismic data (Rm_{reinf}) (a) and raw seismic data (Rm_{raw}) (b). The red zone is the roadway section damaged by an impending coal burst which occurred in the following week. The grey zone is the goaf.	148
Figure 7-4 Seismic energy distributions in LW250105 on 11 September 2014 using reinforced seismic data (RE_{reinf}) (a) and raw seismic data (RE_{raw}) (b). The red zone is the roadway section damaged by an impending coal burst which occurred on 12 September 2014. The grey zone is the goaf.	148
Figure 7-5 Coal burst damage zones and the latest <i>PDZ</i> in the tailgate ahead of the longwall face in LW250105. The red zone is the coal burst damage zone. The blue line is the longwall face position. The yellow zone is the <i>PDZ</i> calculated per production date.	150
Figure 7-6 Efficiency of coal burst prediction using <i>PDZ</i> identification (with $k=0.5$) in LW250105.	151
Figure 7-7 Number of coal bursts in LW250105 above different thresholds of Rm_{reinf} (red) and Rm_{raw} (blue)	153
Figure 7-8 Number of coal bursts in LW250105 above different thresholds of RE_{reinf} (red) and RE_{raw} (blue)	153
Figure 7-9 Coal burst prediction efficiency using Rm_{reinf} (a) and RE_{reinf} (b) with different thresholds. Each blue dot is the prediction efficiency for one coal burst case at a given Rm_{reinf} or RE_{reinf} threshold, and red line is the average prediction efficiency at different Rm_{reinf} or RE_{reinf} thresholds.	154
Figure 7-10 Coal burst prediction efficiency using Rm_{raw} (a) and RE_{raw} (b) with different thresholds. Each blue dot is the prediction efficiency for one coal burst case at a given Rm_{raw} or RE_{raw} threshold, and red line is the average prediction efficiency at different Rm_{raw} or RE_{raw} thresholds.	155
Figure 7-11 Accuracy and efficiency of using Rm_{reinf} in predicting coal burst hazard with different thresholds.	157
Figure 7-12 Accuracy and efficiency of using RE_{reinf} in predicting coal burst hazard with different thresholds.	157

List of Tables

Table 2-1 Indicators of the size range of seismic events (Ortlepp, 2005)	10
Table 2-2 Classification of burst sources in South Africa (Ortlepp and Stacey, 1994)	14
Table 2-3 Classifications of coal bursts and rockbursts in underground mines	20
Table 2-4 Relationship of ppv with distance and charge mass in blasting. R is the hypocentral distance in metres, Q is the charge mass in kilograms.	24
Table 2-5 Typical ppv estimations in underground mines using seismic monitoring	25
Table 2-6 ppv intensity range of seismic sources with different distance and magnitude (Owen, 2005).....	25
Table 2-7 ppv of significant seismic events with different local magnitudes and hypocentral distance in a gold mine in South Africa (Glazer, 2018).....	26
Table 2-8 Kinetic energy and damage intensity as a function of mass and velocity in hard rock mines (Kaiser et al., 1996a)	30
Table 3-1 Mechanical properties and coal burst liability of No. 5 Coal Seam in Huating Coal Mine (China University of Mining and Technology, 2016)	50
Table 3-2 Characteristics of coal bursts in LW250105 during 2014	60
Table 5-1 Input parameters for assessing seismic location error in LW250105	89

List of Symbols

Symbol	Description	Units
A	Area of a fault plane	m^2
D	Distance from a seismic event to the nearest roadway	m
D_τ	Dynamic failure duration	s
d	Distance between two seismic events	m
d_{max}	Twice the sum of radii of two seismic events	m
E	Elastic modulus	Pa
E_S	Seismic energy	J
E_{sum}	Total seismic energy after corrections by the <i>PDE</i> method	J
E_{reinf}	Seismic energy using reinforced seismic data	
E_{raw}	Seismic energy using raw seismic data	
f_c	Corner frequency of seismic wave	s^{-1}
G	Shear modulus	Pa
g	Acceleration of gravity	m/s^2
K_E	Bursting energy index	
$\log E$	Energy magnitude	
M_L	Local (Richter) magnitude	
M_0	Seismic moment	$\text{N} \cdot \text{m}$
m_c	Magnitude of completeness	
m'	Number of seismic events after corrections by the <i>PDE</i> method	
m_{reinf}	Event counts using reinforced seismic data	
m_{raw}	Event counts using reinforced seismic data	
$NHGM$	Number of high ground motions on roadways	
$NPCE$	Number of possible clustered events	
NCE	Number of clustered events	
N_m	Number of emulation tests	

$ppv_{far-field}$	Ground motion in far-field zones	m/s
$ppv_{near-field}$	Ground motion in near-field zones	m/s
$ppvR$	Peak particle velocity (ppv) multiplied by the hypocentral distance R	m ² /s
ppa	Peak particle acceleration	m/s ²
P_D	Wave picking capability of individual geophones	
P_E	Event detection probability of a monitoring system	
Q	Charge mass for blasting	kg
r_0	Source radius	m
R	Hypocentral distance between a seismic event and a seismic sensor	m
R_{NHGM}	Normalised $NHGM$	
R_{NPCE}	Normalised $NPCE$	
RE_{reinf}	Normalised E_{reinf}	
RE_{raw}	Normalised E_{raw}	
Rm_{reinf}	Normalised m_{reinf}	
Rm_{raw}	Normalised m_{raw}	
T	Travel time of a seismic wave from a seismic source to a seismic sensor	s
$v_{ejection}$	Ejection velocity of materials	m/s
V_A	Apparent volume	m ³
W	Total released energy during a fault slip	J
W_{ET}	Elastic strain energy	J
Z	Cover depth	m
δ_p	Random location scatter error	s
δ_v	Wave velocity error	m/s
δ_L	Location error	m
$\Delta\sigma^d$	Dynamic stress induced by ground motions	Pa
η	Seismic efficiency	
ηc	Clustering probability of two seismic events	
η_k	Burst hazard prediction efficiency	

θ	Initial angle of material ejection measured upwards from the horizontal plane	$^{\circ}$
μ	Material rigidity	N/m^2
ν	Poisson's ratio	
ρ	Material density	kg/m^3
σ_1	Maximum principal stress	Pa
σ_2	Intermediate principal stress	Pa
σ_3	Minimum principal stress	Pa
σ_c	Uniaxial compression strength	Pa
Y	Young's modulus	Pa
ψ	Angle between σ_1 and fault plane	$^{\circ}$

List of Publications

The following publications are related to the work of this thesis:

- Wang C, Cao A, Zhang C, Canbulat I (2020) A new method to assess coal burst risks using dynamic and static loading analysis. *Rock Mechanics and Rock Engineering* 53: 1113–1128.
- Wang C, Si G, Zhang C, Cao A, Canbulat I (2021) Location error based seismic cluster analysis and its application to burst damage assessment in underground coal mines. *International Journal of Rock Mechanics and Mining Sciences* 143: 104784.
- Wang C, Si G, Zhang C, Cao A, Canbulat I (2021) A statistical method to assess the data integrity and reliability of seismic monitoring systems in underground mines. *Rock Mechanics and Rock Engineering*. Available online.
- Wang C, Zhang C, Si G, Canbulat I (2021) Ground motion characteristics in an underground burst-prone coal mine. 39th International Conference on Ground Control in Mining, pp 64–68.
- Wang C, Zhang C, Canbulat I, Zhang D, Fan G (2018) Intensity quantification of coal and rock burst risk – a review. Proceedings The Fourth Australasian Ground Control in Mining Conference (AusRock), pp 223-233.

Chapter 1. Introduction

1.1 Background

Notwithstanding progress in developing clean energy technologies in the last decade, coal is still an essential energy source that cannot be easily replaced in emerging economies. In 2019, coal accounted for 27% of global primary energy consumption and 36.4% of global electricity production (BP, 2020). Extensive coal production still occurs in Australia, China, Indonesia and South Africa, and annual production is estimated to increase from a total of 5 billion tonnes in 2021 to 5.5 billion tonnes in 2025 (International Energy Agency, 2020). After more than a century of intensive extraction, shallow coal sources are gradually being exhausted, and coal mining occurs at greater depths. Due to the high in-situ stress and challenging environment in deep rock mass, mining hazards like rockbursts, gas outbursts and large-scale ground caving frequently occur in deep underground coal mines, posing significant threats to personnel, equipment and infrastructure.

Rockbursts are one of the most formidable mining hazards in underground mines. A rockburst is normally referred to as a coal burst when hazards are reported in coal mines. A coal burst is defined as the dynamic failure of coal or rock mass involving a sudden release of strain energy, which causes violent material ejections to the mine opening (Cook, 1965; Zhang et al., 2017). In recent decades, frequent coal bursts have occurred in most mining countries. In the United States, 337 coal bursts reported from 1983 to 2003 caused 20 deaths and 240 injuries (Iannacchione and Tadolini, 2016). In Poland, 42 coal bursts were recorded in the Upper Silesian Coal Basin between 2001 and 2015 (Patyńska et al., 2018). In China, coal mines experienced about 2,000 coal bursts between 1949 to 2015, and 300 casualties were recorded from 2006 to 2013 (Jiang et al., 2014; Zhang et al., 2017). For more than half a century, considerable progress has been made in investigating the occurrence

mechanism of coal bursts and prevention strategies (Gibowicz and Kijko, 1994; Ortlepp and Stacey, 1994; Ortlepp, 2005). However, due to the large variability and uncertainty in their causal factors, coal bursts (and rockbursts) are still the least understood and most formidable type of mining hazard (Ortlepp, 2005).

In coal burst studies, the seismic monitoring technique provides a powerful means of detecting dynamic rock failure and understanding the fundamental mechanism of the burst damage in underground mines (Figure 1-1). The rock fracturing during the mining process, i.e. the mining-induced seismicity, is the normal response of rock mass to underground mining activities. Seismic monitoring can use seismic waves emitted from mining-induced seismicity to determine various source parameters, such as the location, onset time and seismic energy. Routine seismic monitoring enables the rock damage to be quantified and provides a logistical tool to assist forecast, prevention and control of coal bursts. It has become a standard practice in burst-prone mines (Gibowicz and Kijko, 1994; Vasak et al., 2004).

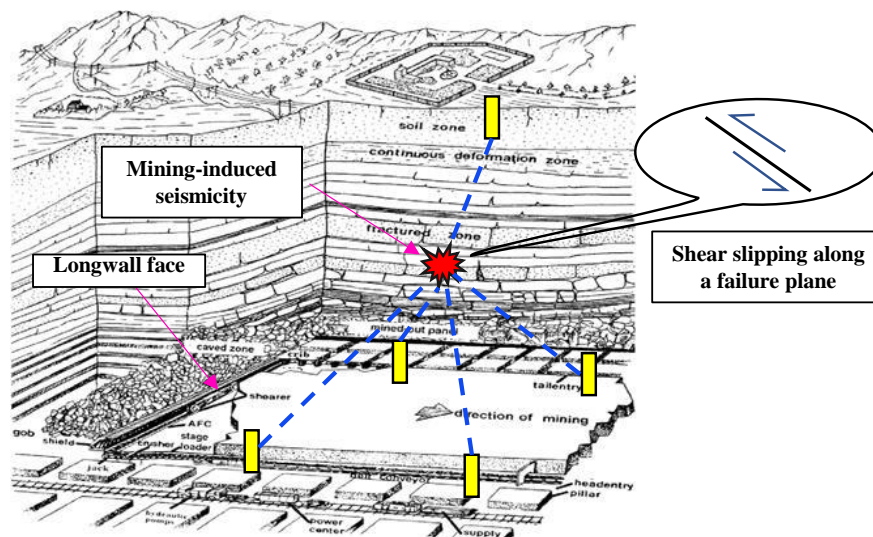


Figure 1-1 A schematic diagram of seismic monitoring applied in longwall coal extraction to trace shear slipping along a failure plane (Cai et al., 2019). The blue line denotes a seismic wave, and the yellow rectangle denotes a seismic sensor

1.1.1 Dynamic impacts from seismic waves

In underground mines, the dynamic impacts caused by the seismic waves of mining-induced seismicity are one of the main factors triggering coal bursts (Cai et al., 2020a). The ground motions induced by the seismic waves can generate transient dynamic stresses to the surrounding materials, which may break the unstable equilibrium in the highly stressed coal and rock mass and trigger dynamic failure (Ortlepp and Stacey, 1994; Kaiser and Cai, 2013a). Seismic events with significant seismic energy (like burst events) can cause strong ground motions to accelerate the dynamic failure of the rock mass. Excavations may also experience much greater ground motions than expected if a seismic event occurs nearby.

To investigate the triggering mechanism of seismic waves for burst damage, previous studies have mainly focused on quantifying ground motion using seismic monitoring systems. In hard rock mines, the analysis of ground motions is also used to design ground support, which aims to absorb the energy stimulated by seismic waves and withstand the deformation of excavations. Compared with hard rock mines, coal mines have different mining methods and mechanical properties of rock material, which may present different ground motion intensities and triggering conditions for burst damage. However, few studies have been conducted to explore ground motion characteristics in coal mines, and limited knowledge is available about support design under the seismic impacts from coal bursts.

1.1.2 Defective seismic data

Defective seismic data refers to inaccurate data recordings in underground mines. Due to the varying mechanical properties of rock material and numerous geological structures, the underground environment is highly anisotropic. Also, the existence of mined voids (e.g., goafs in coal mines) further increases the complexity. Under such conditions, seismic waves may have complicated transmission pathways

with strong signal attenuation before being received by seismic sensors. As most algorithms that seismic monitoring systems use are based on simplified wave velocity models, errors are inevitable in calculating source parameters of mining-induced seismicity, such as event locations and seismic energy. It is also hard for a seismic monitoring system to record the complete spectrum of seismic data in underground mines. The integrity of the monitored seismic data, referred to as the seismic data integrity, has a close relationship with the locations of seismic sensors. Since seismic sensors are commonly installed around mine excavations, the spatial distribution of seismic sensors is limited by the excavation layout. A system is more likely to detect a seismic event if its location is encircled by the seismic sensors. Inversely, the seismic monitoring system may miss seismic events if they are located outside the sensor-enclosed area.

Compared with hard rock mines, underground coal mines face more challenges from defective seismic data. Since the cleats in the coal seam lead to extra variations in the structural and mechanical properties, more complicated wave transmission paths and lower signal-to-noise ratio are encountered, which brings more difficulties in locating seismic events. In addition, the tabular excavations in longwalls significantly limit the flexibility of the sensor layout, which makes it hard to cover the area of interest spatially. Under these unfavourable monitoring conditions, underground coal mines can have higher location errors and lower seismic data integrity. Therefore, how to evaluate seismic data quality and eliminate the impact of defective data have become the key issues in improving the performance of seismic monitoring in coal mines.

1.1.3 Seismic precursors prior to coal bursts

A seismic wave from mining-induced seismicity cannot only generate dynamic impacts on rock mass, but also contains extensive information to be used as precursors of impending burst hazards. The methods that use source parameters to

analyse rock stabilities and assess hazard potential are called ‘seismic methods’ in this thesis. It has been observed in laboratory tests that the appearance of massive fractures with increased energy release is commonly present in fully loaded rock before its failure. Therefore, many seismic methods have been developed to locate the potential dynamic failure zones by mapping the spatial and/or temporal concentrations of seismic events and seismic energy. Also, as the failure of geological structures is commonly formed by the coalescence of fractures, seismic clustering analyses were conducted as one of seismic methods to investigate the connections between seismic events, which are used for detecting invisible faults and dykes which have damage potential.

The real-time updating of seismic data allows seismic methods to provide timely burst risk assessments that best meet specific in-situ conditions. However, as seismic methods are completely dependent on seismic monitoring data, the data quality directly affects the accuracy and efficiency of analysis and results. Compared with hard rock mines, the lower seismic data quality in coal mines significantly limits the performance of seismic methods in forecasting burst hazards. Therefore, it is essential to consider seismic data quality before applying seismic methods and eliminate the impact of poor data quality on hazard assessment results.

1.2 Objectives and scope of the research

The research goal of this thesis is to investigate the dynamic impacts of mining-induced seismicity on coal burst damage and evaluate seismic data quality in seismic methods, aiming to improve performance in assessing coal burst risks in underground mines. To achieve this goal, the following research scope and objectives were set:

- Review the occurrence mechanism of rockbursts, the dynamic impacts caused by mining-induced seismicity and popular seismic methods for evaluating burst risks.
- Quantify ground motions at roadways induced by mining-induced seismicity and investigate their impacts on impending coal burst damage in roadways.
- Develop a method to evaluate locating accuracies of seismic events in longwalls for a specific layout of geophones.
- Propose a method to assess the integrity of seismic data and the detection capability of a seismic monitoring system.
- Propose a seismic data correction method to improve the performance of seismic methods in assessing coal burst risks.

1.3 Thesis structure

This thesis contains eight chapters.

Chapter 2 presents a detailed literature review on the fundamentals of coal bursts and rockbursts and the dynamic impacts of mining-induced seismicity in underground mines, followed by an extensive review of seismic analysing methods for evaluating burst risks in coal and hard rock mines.

Chapter 3 presents an overview of the case study site, the Longwall (LW) 250105 panel in Huating Coal Mine, Gansu Province, China. The details of the geological and mining conditions of the studied longwall are introduced, and a survey is conducted on the seismic monitoring system and the seismic activities during the study period. The characteristics of coal bursts and the induced damage in roadways are also illustrated.

Chapter 4 analyses the ground motion characteristics to study the relationship between seismically induced impacts and coal burst damage. Intensities of ground motions from seismic events and the induced dynamic stresses are quantified. The historical ground motions that roadways have experienced are linked with the cumulative damage to coal and rock mass. A ground motion-based method is also proposed to assess the coal burst damage potential in roadways.

Chapter 5 evaluates the location error evolutions in a longwall for a seismic monitoring system with varying geophone layouts. The size and orientation characteristics of location errors are investigated and the probability density of locating seismic events is demonstrated. A modified seismic clustering method is proposed to consider the influence of location errors when assessing coal burst risks in a longwall.

Chapter 6 develops a statistical method to quantify the seismic data integrity and detection capability of the seismic monitoring system in a longwall. The capability of each geophone to detect seismic events is first evaluated according to different energy and hypocentral distances. Then, the detection probability characteristics of the seismic monitoring system are investigated. Finally, a method based on the seismic detection probability is proposed to correct event counts and seismic energy in longwalls.

Chapter 7 develops a method to reinforce the raw seismic data, aiming to reduce the influence of unfavourable location errors and detection probabilities on seismic analyses. The performance of seismic methods in assessing coal burst risks by using raw seismic data and reinforced seismic data is compared. The spatial variations of seismicity using reinforced seismic data are calculated to investigate their correlation with coal burst damage in the studied longwall.

Finally, Chapter 8 summarises the main conclusions from the previous chapters and makes recommendations for future studies.

Chapter 2. Literature review

2.1 Introduction

In underground coal mines, the key challenge for quantitatively assessing coal burst hazards is to identify the critical condition of coal and rock mass in energy and/or stress terms. It requires clear understanding of mining-induced seismicity and the burst damage mechanism linked to observations from real cases of massive accidents. Therefore, this chapter first provides a background review on the mechanism of mining-induced seismicity, classifications of coal burst and rockburst damage, and seismic impacts on rock mass failure. To demonstrate the relationship between seismic information and coal burst and rockburst hazards, this chapter also reviews some popular seismicity-based analysis methods for assessing burst risks and their latest developments. Finally, the deficiencies of current seismic monitoring systems and their impacts on analysing burst risks are introduced.

2.2 Mining-induced seismicity and burst damage classification

2.2.1 Mining-induced seismicity

Mining-induced seismicity is the response of coal and rock mass to mining activities, which is associated with rock failures resulting from stress redistribution in the rock mass near mine openings (Cook, 1976; Hudyma, 2008). The generation of mining-induced seismicity is strongly affected by the local geology and tectonics, such as the interactions of material inhomogeneities and discontinuities during mining, and lithostatic and residual tectonic stress in the local area (Ortlepp, 1985).

Gibowicz and Kijko (1994) distinguished two broad types of mining-induced seismicity: seismicity directly related to mining activities and seismicity caused by the slipping of geological faults. Since coal seams are blocky structures with a

number of cleats inside, the major mechanism for both types of mining-induced seismicity in coal seams is the shear failure, including bedding plane shear, reactivation of shear plane and fault slip (Galvin, 2016). Similar to earthquakes, the shear-related mining-induced seismicity can be explained as the elastic rebound theory, which demonstrates the stick-slip behaviour of a shear slipping along a discontinuity. Earthquakes occur due to the sudden release of shear stress and strain by the fault movement (Shearer, 2009). This mechanism can be illustrated by a simple model with a block pulled by a spring, as shown in Figure 2-1. When the force imparted by the spring to the block is larger than the static friction, the block will slip along the plane until the force decreases to be equal to or less than the dynamic friction.

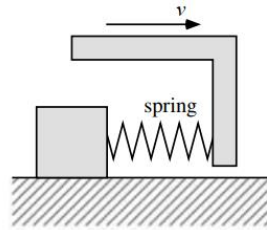


Figure 2-1 Model of a shear slipping along a plane (Shearer, 2009)

The variations of shear stresses and energy during the slipping of a geological discontinuity are well interpreted in Figure 2-2 (McGarr, 1993). A fault with area A is loaded to failure from the initial shear stress τ_1 . The plane slips D in the distance and the shear stress drops linearly from τ_1 to τ_2 . The total released energy W during the process is:

$$W = \left(\frac{\tau_1 + \tau_2}{2} \right) DA \quad (2-1)$$

where $\bar{\tau}$ is the average of τ_1 and τ_2 . The apparent stress, τ_a , is defined as the difference between $\bar{\tau}$ and the average resisting stress $\bar{\tau}_r$:

$$\tau_a = \bar{\tau} - \bar{\tau}_r = \eta \bar{\tau} \quad (2-2)$$

where η is the ratio of τ_a to $\bar{\tau}$, which is also called seismic efficiency. The seismic energy E_s is thus calculated as:

$$E_s = \tau_a DA \quad (2-3)$$

In Eq. (2-2), seismic efficiency η is commonly only at the order of 0.01 (Cook, 1963; McGarr, 1976). McGarr (1999) found that nearly all energy released by faulting is consumed in overcoming friction with a seismic efficiency of about 0.06. The results from McGarr (1994) indicated that seismic efficiencies range from 0.002 to 0.028. It demonstrates that most of the energy generated during the fault slipping process is dissipated by the resisting stress, the shaded area in Figure 2-2. Only a small proportion is radiated in the form of seismic energy, the stippled area in Figure 2-2. Table 2-1 shows the seismic energy range of mining-induced seismicity, extending seven orders of magnitude from superficial strain burst to the extensive collapse of a tabular mine (Ortlepp, 2005).

Table 2-1 Indicators of the size range of seismic events (Ortlepp, 2005)

Local Magnitude (ML)	Kinetic (seismic) Energy (MJ)	Explosive Equivalent (kg)	Radius of Source Rupture (m)
-1	0.002	0.04	0.8
0	0.06	1.2	2.6
1	2.0	40	8.5
2	60	1,200	26
3	2,000	40,000	84
4	60,000	1,200,000	270

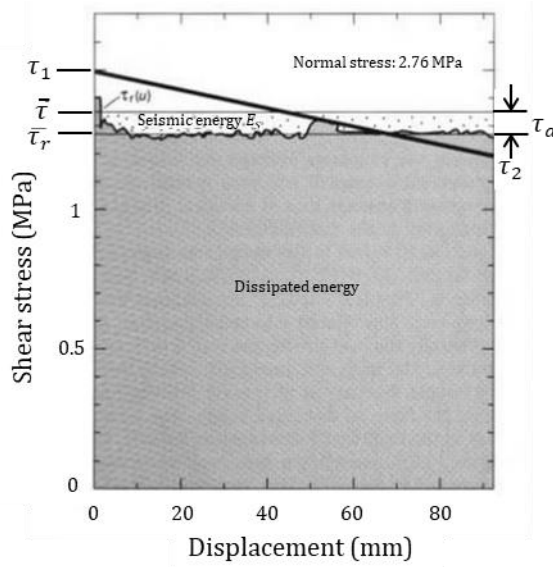


Figure 2-2 Diagram of the relationship between shear stress, resisting stress (friction) and displacement of a fault plane during an earthquake (McGarr, 1993). The shaded area is the dissipated energy during the process, and the stippled area is the radiated seismic energy available for ground motions.

According to the different types of geological discontinuities, the triggering of mining-induced seismicity, i.e. the activation of discontinuity slipping, requires different stress conditions. Jaeger et al. (2009) demonstrated the failure criteria of three typical faulting types based on Mohr's circle analysis, which is shown in Figure 2-3 and Figure 2-4. For a thrust fault with the minimum principal stress σ_3 in vertical equivalent to $\rho g Z$ (see Figure 2-3a), the maximum principal stress σ_1 in the horizontal direction has to increase until the Mohr's circle intersects with the failure line (see Figure 2-4a). For the slipping of a normal fault loaded by the maximum principal stress σ_1 in the vertical plane with a value of $\rho g Z$, the minimum principal stress σ_3 in the horizontal plane should be reduced to a point where the Mohr's circle can intersect with the failure line (see Figure 2-3b and Figure 2-4b). For a strike-slip fault, the intermediate principal stress σ_2 of $\rho g Z$ is applied, and the faulting movement will be triggered if the minimum principal stress σ_3 in the vertical plane decreases to point A or the maximum principal stress σ_3 in the horizontal plane increases to point B (see Figure 2-3c and Figure 2-4c). It

demonstrates that occurrence of mining-induced seismicity depends on the discontinuity types and loading paths of the mining activities, which is related to the mining intensity, mining direction and mining method.

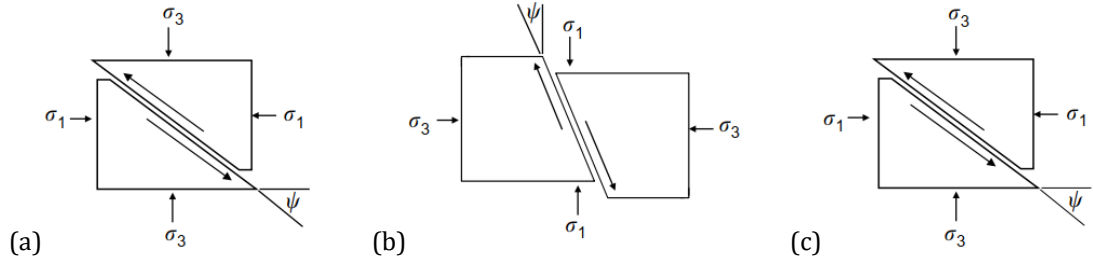


Figure 2-3 Principal stresses around (a) thrust fault (vertical plane), (b) normal fault (vertical plane) and (c) strike-slip fault (horizontal plane) (Jaeger et al., 2009)

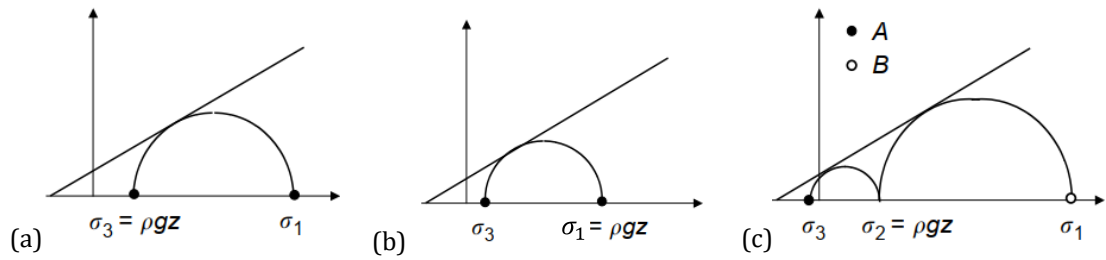


Figure 2-4 Mohr-Coulomb diagram illustrating the reactivation of (a) thrust fault, (b) normal fault and (c) strike-slip fault (Jaeger et al., 2009)

In underground mines, hazardous mining-induced seismicity may periodically occur during the mining process when major faults are nearby. This phenomenon can be explained by the recurring earthquake model developed by Shimazaki and Nakata (1980), which is shown in Figure 2-5. In this model, τ_1 is the triggering stress threshold of the fault slipping, which is related to the static friction on the fault; τ_2 is the stress level of the fault after a slipping, which is related to the dynamic friction on the fault. If the dynamic friction and static friction are constants, both earthquake occurrence time and intensity are predictable. If either dynamic friction or static friction is known, it is possible to forecast the time or intensity of the earthquake. However, due to the significant variations in the stress distribution and

faulting condition induced by mining operation, both dynamic and static frictions of mining-induced seismicity are variables. Therefore, an accurate prediction of hazardous mining-induced seismicity requires a deep understanding of the source mechanism and comprehensive information on faulting parameters.

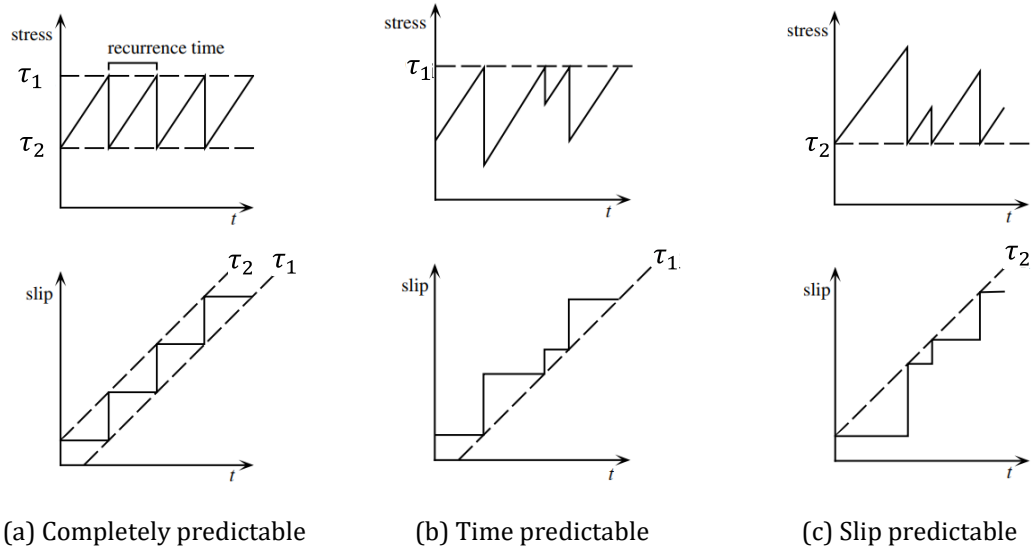


Figure 2-5 A simplified model of recurring earthquakes. τ_1 and τ_2 are the shear stress levels before and after earthquakes, respectively (Shearer, 2009).

2.2.2 Classifications of coal burst and rockburst damage

The definition and classification of coal bursts have not yet been unified around the world. In countries like Australia and the United States, the terminology “coal burst” is particularly used in coal mines, while “rockburst” is mainly used in hard rock mines (Mark, 2016; Hebblewhite and Galvin, 2017). However, in other countries like China, Poland and South Africa, “rockburst” is used in both coal mines and hard rock mines (Blake and Hedley, 2003; Stec, 2007; Ptáček, 2017). To distinguish differences in geological conditions and damage intensities between coal mines and hard rock mines, the term “coal burst” is adopted in this study to specifically refer to the burst damage that occurs in coal mines.

Many researchers have classified coal bursts and rockbursts based on the intensity of the energy source, damage mechanism and burst location. Ortlepp and Stacey (1994) classified burst sources based on the data from coal and hard rock mines in South Africa, which shows a wide range of burst source intensity from -0.2 to as much as 5.0 in Richter magnitude M_L (see Table 2-2). The classification was based on the first motion of seismic records, the event magnitude and the source mechanism. The first three types of rockbursts indicate coincident locations of the seismic source and burst damage, and a relatively low intensity of burst source is present with M_L between -0.2 to 2.5. The last two types have shear failures on the seismic source, which can be hundreds of metres away from the burst damage area, and a more intensive burst source is present with M_L from 2.0 to 5.0.

Table 2-2 Classification of burst sources in South Africa (Ortlepp and Stacey, 1994)

Rockburst type	Postulated source mechanism	First motion from seismic records	Richter Magnitude M_L
Strainbursts	Superficial spalling with violent ejection of fragments	Usually undetected, could be implosive	-0.2 to 0
Buckling	Outward expulsion of larger slabs pre-existing parallel to surface of opening	Probably implosive	0 to 1.5
Pillar or face crush	Sudden collapse of stope pillar, or violent expulsion of large volume rock from tabular stope face or tunnel face	Possibly complex, implosive and shear	1.0 to 2.5
Shear rupture	Violent propagation of shear fracture through intact rock mass	Double-couple shear	2.0 to 3.5
Fault-slip	Sudden movement along existing fault	Double-couple shear	2.5 to 5.0

In Poland's Ostrava-Karvina Coal Field, coal bursts were roughly classified in terms of the source of additional stress that is imparted to the rock mass in the bursting location: (1) additional stress from the mining edge or residual pillars, (2) unstable isolated coal pillars, (3) pre-coal face pressures in front of the longwall face, (4) additional stress generated by old workings, and (5) intentionally triggered rockburst by blasting work (Ptáček, 2017). Similarly, these coal bursts can also be divided into two groups: those with seismic sources in the coal seam and those with

seismic sources in the overburdened rock strata, which are in accordance with strainbursts and fault-slip bursts, respectively (see Figure 2-6).

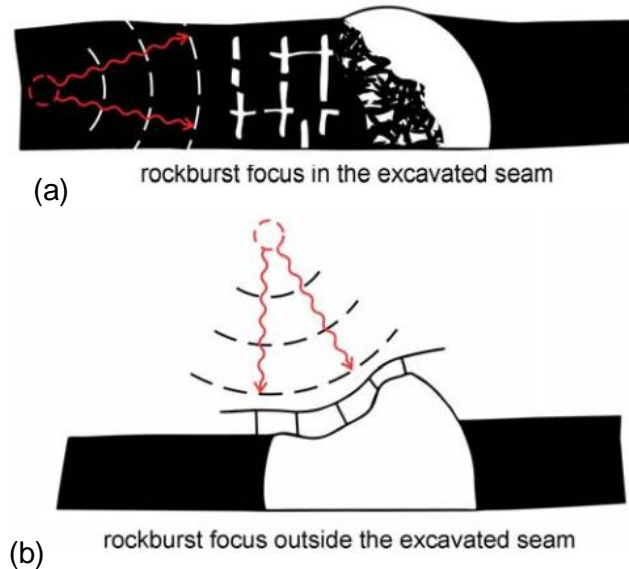


Figure 2-6 Two types of coal burst classified in the Ostrava-Karvina Coal Field (Ptáček, 2017)

For fault-related coal bursts, Cai et al. (2020b) classified them into mining-induced static stress (FRMSS)-dominated and seismic-based dynamic stress (FRSDS)-dominated based on the relationship between fault location and mining layout, as shown in Figure 2-7. It is rare to trigger a fault-slip coal burst when the longwall is far away from the fault (see Figure 2-7a). When a longwall face approaches a fault pillar, the fault-slip coal burst is FRMSS-dominated, which shows abutment stress increases vertically but decreases horizontally (see Figure 2-7b). When a longwall face is moving away from a fault pillar, the abutment stress increase in the horizontal direction and decrease in the vertical direction will also result in an FRMSS-dominated fault-slip coal burst (see Figure 2-7c). In an FRSDS-dominated fault-slip coal burst, the longwall is retreating in parallel to a fault. A critical stress concentration in the pillar will occur, and mining-induced seismicity can easily trigger a fault-slip burst (see Figure 2-7d).

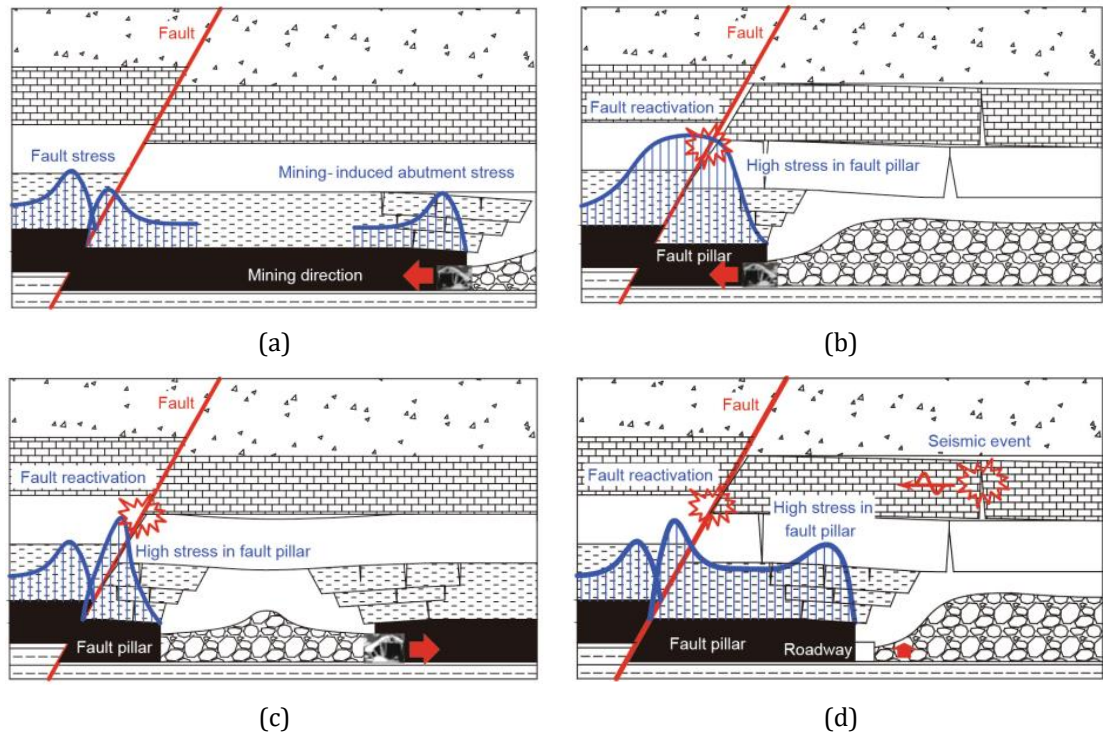


Figure 2-7 Fault induced coal burst mechanism: (a) the mining operation is far away from the fault, (b) the mining operation is approaching the fault, (c) the mining operation is leaving the fault, and (d) the direction of the mining operation is parallel to the fault (Cai et al., 2020b)

Kaiser and Cai (2013a) categorised rockbursts into three types according to the source of energy that can induce damage in hard rock mines: strainbursts, pillar bursts and fault-slip bursts. This classification emphasised the important role of stiffness on the loading system in triggering rock bursting, which is often ignored in support design. They also pointed out that whether ground motions can trigger burst damage depends on the local energy level in the bursting rock and the mine stiffness. This view is also discussed by Bräuner (2017), who stated that even a small seismic disturbance may trigger violent burst hazards with no extra energy input if the coal or rock mass is already in a state of unstable equilibrium. An example illustrating the stable and unstable equilibrium of the rock mass is given in Figure 2-8. Also, rare cases supported that a seismic load is strong enough to induce rockburst damage where the static load is at a low level (Bräuner, 2017).

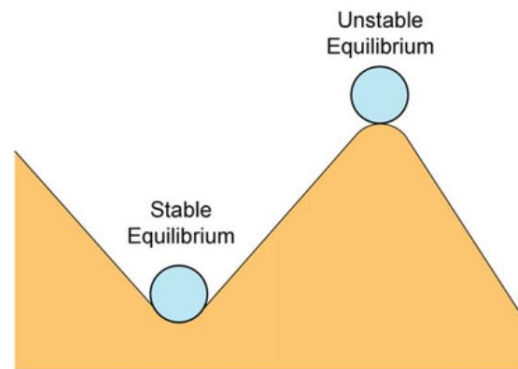


Figure 2-8 Visualisation of stable and unstable states of equilibrium in rock mass (Galvin, 2016)

Similar to the work by Kaiser and Cai (2013a), many researchers agreed that apart from critically stressed rocks, the strain energy released from the surroundings of the mine opening with low stiffness, i.e. the additional energy from the soft loading system, is another primary energy source for coal or rock bursting (Jaeger and Ryder, 1999; Galvin, 2016; Xu and Cai, 2017). The violent rock failure induced by the soft loading system is commonly observed in laboratory tests. A rock sample loaded in a non-stiff testing machine usually fails in an uncontrolled and violent manner, which is similar to the phenomena of rockbursts. Such unstable sample collapse is caused by the rapid energy flowing into the sample from the loading system (Jaeger et al., 2009).

In underground mines, the strain energy stored in the loading system, such as the roof and floor, will be released to loaded coal or rock mass after reaching the peak strength. The relationship between the stiffness of the loading system and the post-failure stiffness of the loaded rock mass controls the failure stability of the coal or rock mass (Galvin, 2016). If the loading system is larger than the post-failure rock mass in stiffness, the rock mass will fully dissipate the strain energy released from the loading system and fail in a controlled manner (Figure 2-9a). Otherwise, the undissipated additional energy will transfer to kinetic energy, resulting in uncontrolled coal mass failure (Figure 2-9b).

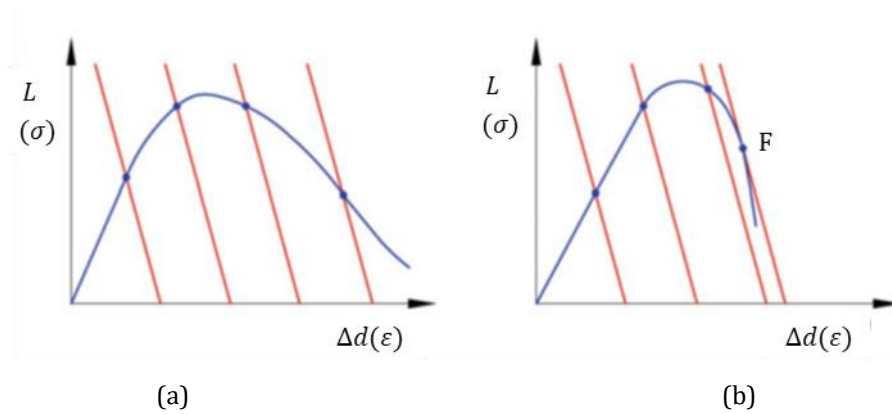


Figure 2-9 Stress-strain curves (blue line) of the rock mass with (a) controlled failure and (b) uncontrolled failure. The red line is the stiffness of the loading system (Galvin, 2016).

The stiffness of the loading system and post-failure stiffness of coal and rock mass is not only a material property but also a function of several factors:

- (i) Geometry of the loading system. For the overlying strata, the stiffness decreases when its thickness decreases or span increases (Gu, 2013; Galvin, 2016).
- (ii) Structure of the loading system. When mining intersects a tectonic structure like a fault or dyke, the stiffness of overburden will also have an instant decrease as the bridging beam is transformed into a cantilever (Galvin, 2016).
- (iii) Loading speed. The post-peak failure modulus of loaded materials reacts differently with the loading rate: some show an increase in the increasing strain rate (see Figure 2-10a), while some have opposite results (see Figure 2-10b). It can be extrapolated that how the mining rate affects the burst hazard potential depends on the changes in values of post-peak failure modulus with the strain rate (Bukowska, 2013).

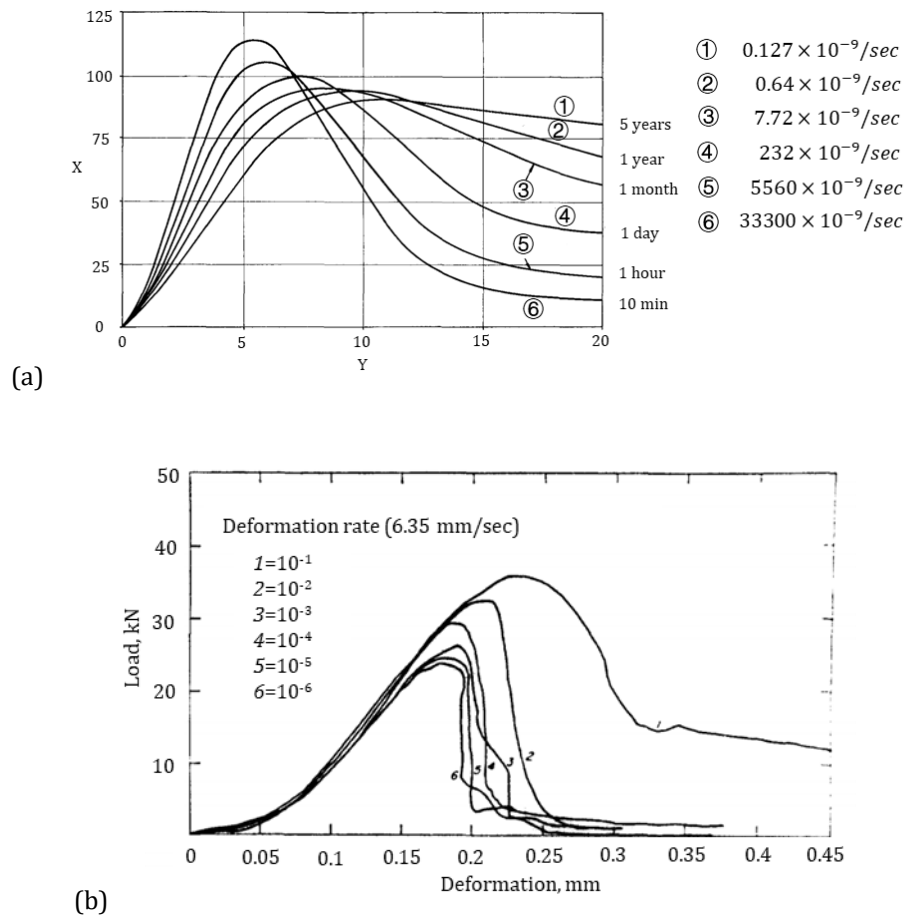
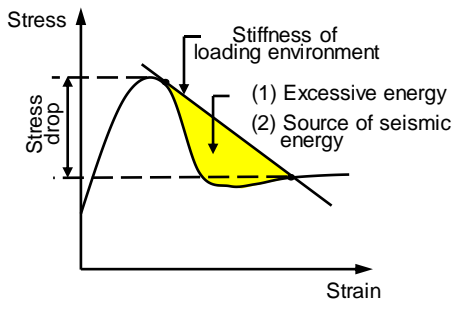
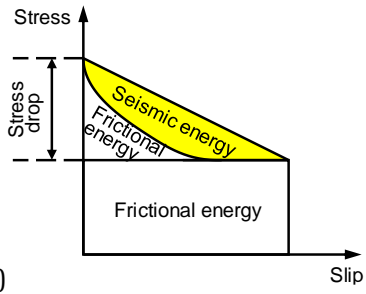
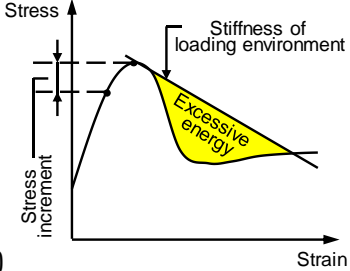


Figure 2-10 Complete load–deformation curves with different strain rates for
(a) sandstone (Bieniawski, 1970) and (b) Tennessee marble (Peng, 1973)

Based on the classifications mentioned above, two basic damage mechanisms of coal bursts and rockbursts can be concluded: direct burst and indirect burst, as shown in Table 2-3. For the direct burst type, the seismic source is co-located with the damage location, which includes strainburst and pillar burst. The amount of total energy released during the bursting process depends on the stored strain energy in the bursting rock and the stiffness of the loading environment, which is shown in Table 2-3a (Kaiser, 1996; Vardar et al., 2017). Seismic loads in direct bursts behave as triggers of burst damage with no stress or energy input. For the indirect burst type, the seismic source and the damaged area have different locations. In the seismic source, a large amount of seismic energy is released due to the slipping of

the geological discontinuities (Table 2-3b). As shown in Table 2-3c, the burst damage in the mine opening is not only caused by the excessive energy in the post-peak period of the coal and rock mass, but also partly from the seismic energy from seismic waves that causes considerable stress increment (Ryder and Jager, 2002; Kaiser and Cai, 2013c).

Table 2-3 Classifications of coal bursts and rockbursts in underground mines

Types	Source mechanism	
Direct burst	 <p>(a)</p>	
	Source mechanism is possibly complex, implosive and shear (Ortlepp, 1997)	
Indirect burst	 <p>(b)</p>	 <p>(c)</p>
	Double couple shear (Shearer, 2009)	

2.3 Dynamic impacts of seismicity

2.3.1 Near-field and far-field zones of a seismic source

The onset of a seismic event is associated with a stress drop and energy release on the ruptured plane, which is commonly assumed to be a circular area with a source radius r_0 . There are significant differences in the rock deformation behaviour between the zones within and outside the source radius of a seismic event (see Figure 2-11). Within r_0 of the source, the rock mass has permanent

displacement and stress change. The intensive ground motions may even cause visible damage to the excavation. For the zone at a distance between r_0 and $2r_0$ to the source, strong ground motions can cause stress change that may affect adjacent fractures (Kaiser, 1996). Therefore, a near-field zone of a seismic event is defined as the zone within twice of its source radius. On the other hand, the far-field zone is defined as outside twice of its source radius. In the far-field zone, the radiated seismic waves from the source can only cause non-permanent displacement and stress change, and the ground motions are usually inversely proportional to the distance from the source. As a result, the types of ground motion that excavations incur depend on the distance between the excavation and the seismic event.

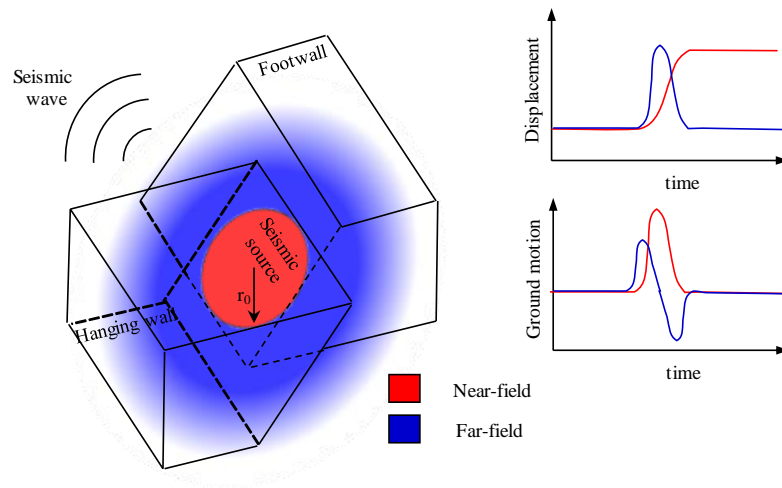


Figure 2-11 Characteristics of displacement and ground motion in rock mass at the near-field and far-field zones, modified from Shearer (2009)

Source radius r_0 can be calculated by several source models such as the Brune model (Brune, 1970), Madariaga model (Madariaga, 1976) and apparent volume model (Mendecki, 1993). The Brune model (Brune, 1970) and Madariaga model

(Madariaga, 1976) assumed that r_0 is proportional to the S-wave velocity v_s but inversely proportional to the corner frequency of the seismic wave (f_c):

$$r_0 = \frac{k_c v_s}{2\pi f_c} \quad (2-4)$$

where k_c is a source model-dependent constant. In the Brune model, $k_c = 2.34$ is adopted as the method uses the simplest source model, which only considers S-waves and ignores the observation angle. Although the Brune model has been widely used in the seismology community, it tends to provide a much larger estimation on r_0 of rockbursts in underground mines (Coulson, 2009). In contrast, a quasi-dynamic model of the circular fault is adopted in the Madariaga model, which determined k_c as 2.01 for P-waves and 1.32 for S-waves. Compared with the Brune model, the Madariaga model presents a better agreement of source radius with the field observations in underground mines (Gibowicz et al., 1990).

The apparent radius originated from the concept of apparent volume proposed by Mendecki (1993). The apparent volume V_A is the parameter to estimate the volume of inelastic deformation in the seismic source that radiates seismic waves, which is determined as:

$$V_A = \frac{M_0^2}{2\mu E_s} \quad (2-5)$$

where M_0 is the seismic moment, μ is the rock rigidity, E_s is the seismic energy. The radius of the V_A , i.e. the apparent radius, is thus calculated as (Kaiser and Maloney, 1997):

$$r_0^3 = \frac{3V_A}{4\pi} \quad (2-6)$$

As the aforementioned models were initially developed from earthquake engineering principles, they should be used cautiously in mines due to the differences in study scale and accuracy requirements. In underground mines, the mining scale is commonly only hundreds of metres, which requires a higher accuracy for both seismic locating and source parameters than earthquake study. However, due to the complex mining environment and restrictions on geophone layout, it can be challenging to calculate accurate source radius by using these models in regular analysis. Therefore, in this study, the source radius is estimated by an empirical equation proposed by Jager and Ryder (1999) based on the experience in South African underground mines:

$$r_0 = 10^{(1+M_L/2)}/2 \quad (2-7)$$

where M_L is the local magnitude of the event. Based on Eq. (2-7), the source radii of seismic events range from 1 m to 25 m when seismic energies range from 1 kJ to 10,000 kJ.

2.3.2 Ground motions

When a stress wave travels in a medium (solid or fluid), stress is applied to particles of the medium. The particles are accelerated to oscillate around their original positions. The speed of particle movement is termed particle velocity, which describes the physical speed of particles moving back and forth in the direction when stresses are passing through (Zhou and Zhao, 2011). Unlike the particle velocity, the seismic wave velocity describes the speed of the wave passing through the medium, and it is roughly three orders of magnitude larger than the particle velocity (Roberts and Brummer, 1988). The intensity of ground motion in underground mines can be represented by the peak particle velocity (*ppv*) at a potential target caused by a stress wave from a seismic event. As the wavelength of a typical seismic compressive wave is considerably larger than the size of the tunnel,

all the particles in the immediate vicinity of the tunnel are moving at essentially the same velocity (see Figure 2-12). *ppv* characteristics becomes more complex to define in a longwall because the size of the longwall is comparable with the wavelength of the seismic wave (Roberts and Brummer, 1988).

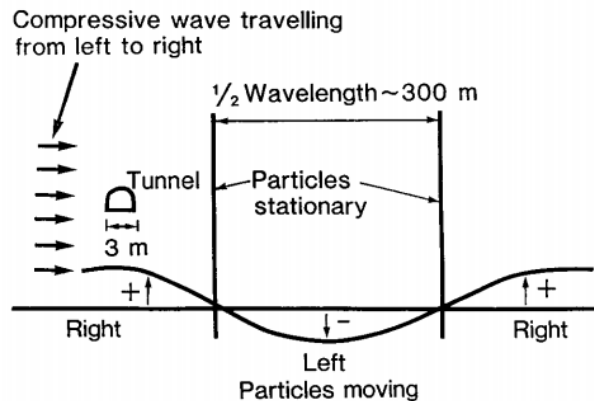


Figure 2-12 Schematic diagram of a compressive seismic wave superimposed on a tunnel (Roberts and Brummer, 1988)

In general, there are two ways to investigate *ppv* characteristics: conducting simulated rockburst tests, and analysing the historical seismic database. In the simulated rockburst test, blasting is used as a seismic source to calibrate the attenuation curve of *ppv* along with the distance between the seismic sensor and blasting source with a certain intensity. Equations listed in Table 2-4 show the relation of the *ppv* value with the charge mass and distance.

Table 2-4 Relationship of *ppv* with distance and charge mass in blasting. *R* is the hypocentral distance in metres, *Q* is the charge mass in kilograms.

Equation	Reference	Notes
$ppv = 1143(R/Q^{0.5})^{-1.6}$	(Rorke, 1992)	Far-field
$ppv = 650(R/Q^{0.5})^{-1.42}$	(Ouchterlony et al., 1997)	Far-field

In contrast to simulated rockburst tests, *ppv* estimation using the historical seismic database is based on observations from regional seismic monitoring during mining. It means that all seismic sources are mining-induced and both the source

intensity and distance are uncontrolled. Table 2-5 shows some of the empirical equations for *ppv* estimation in underground mines. As can be seen that for a given seismic moment, the estimated value of *ppv* is inversely proportional to the distance between the particle and the seismic source. Based on conservative *ppv* ranges by Kaiser and Maloney (1997) and the relation between *ppv* and damage by Hedley (1992), Owen (2005) proposed the *ppv* ranges of interest, typical damage severity and the target distance associations in hard rock mines (see Table 2-6). It shows that even a relatively small seismic event can induce considerable *ppv* and cause severe damage to the excavation if the hypocentral distance is small enough (< 3 m). The *ppv* intensities induced by larger seismic events with different hypocentral distance in a gold mine are summarised by Glazer (2018) in Table 2-7. It shows that a *ppv* of 2.3 m/s can be reached if a seismic event with a magnitude between 3.8 and 4.1 occurs 100 m away.

Table 2-5 Typical *ppv* estimations in underground mines using seismic monitoring

Country	Equation	Notes	Reference
Gold mines in South Africa	$\log(ppv \cdot R) = 0.49 \log(M_0) - 4.68 \text{ (cm}^2/\text{s)}$	Near-field	(McGarr et al., 1981)
Coal mines in Poland	$\log(ppv \cdot R) = 0.66 \log(M_0) - 7.4 \text{ (m}^2/\text{s)}$	Near-field	(Mutke et al., 2016)
Gold mines in South Africa	$\log(ppv \cdot R) = 0.98 \log(M_0) - 1.97 \text{ (m}^2/\text{s)}$	Far-field	(Glazer, 2018)

Table 2-6 *ppv* intensity range of seismic sources with different distance and magnitude (Owen, 2005)

<i>ppv</i> range (mm/s)	Damage Category	Approx. design distance R (m) from seismic source		
		M _L =2.5	M _L =1.5	M _L =0.5
< 50	No damage	> 700	> 150	R > 75
50 to 300	Falls of loose rock	75 to 700	30 to 150	3 to 75
300 to 600	Falls of ground	45 to 75	15 to 30	Near-field
> 600	Severe damage	< 45	< 15	Source zone

Table 2-7 *ppv* of significant seismic events with different local magnitudes and hypocentral distance in a gold mine in South Africa (Glazer, 2018)

Distance (m) \ ML	1.7–2.3	2.8–3.2	3.8–4.1
100	2.6 cm/s	24.4 cm/s	2.3 m/s
200	1.0 cm/s	9.5 cm/s	0.9 m/s
500	0.3 cm/s	2.7 cm/s	0.3 m/s

Although it is convenient to investigate *ppv* characteristics using seismic data if a seismic monitoring system has already been installed in the mine, there are physical constraints that can affect the reliability of the results. Since a seismic monitoring system is designed for event location and source parameters estimation, the seismometers are usually installed far away from the mining activity zone to avoid signal noise and influence from the fractures surrounding the excavations (Mendecki, 2016). Also, the limited amplitude range means the seismic sensor is unable to record ground motions from the nearby seismic source, i.e., the *ppv* in the near-field zone, referred to as near-field *ppv*.

The near-field *ppv* has been evaluated in several hard rock mines in South Africa using synthetic seismograms or semi-empirical models from seismic monitoring results. In Mponeng and East Driefontein Mines in South Africa, the near-field *ppv* was evaluated as 0.34–0.46 m/s, caused by seismic events in the local magnitude of 1.2–2.4 (Cichowicz, 2001). Intensive near-field *ppv* of up to 5.88 m/s was recorded in an American mine at about 3 km depth (McGarr, 1991). In the East Rand Proprietary Mines in South Africa, a lower near-field *ppv* was found from events of -0.76 to 1.40 in local magnitude, ranging from 5.4×10^{-4} m/s to 6.25×10^{-2} m/s (McGarr et al., 1981). Ground motions in the near-field zone have also been surveyed using specially designed sensors attached to the excavation surface, which can record high amplitude vibration induced by nearby events. Dubiński and Mutke (1996) summarised that the near-field *ppv* in Upper Silesian Coal Basin coal mines is between 0.01 m/s and 10 m/s, and the corresponding stress increase is from

0.1 MPa to 50 MPa. It has been reported that in several hard rock mines in South Africa, near-field *ppv* driven by the failure of intact rock can be up to 3.0 m/s, and a dynamic stress drop on previously failed shear planes can cause a near-field *ppv* of 0.1 m/s (Milev et al., 2002).

However, due to the complicated calculation procedure and limitations in monitoring sensors, ground motions in near-field zones are still excluded from regular ground motion analysis, which is one of the major deficiencies for ground motion studies that needs to be addressed (Kaiser and Cai, 2013a). Given the immense vibrations and potential damage to underground openings, the intensity of ground motions in near-field zones needs to be estimated and considered for coal burst forecasting and control.

2.3.3 Ejection velocity

The dynamic failure in underground mines commonly causes a high ejection velocity of the materials to the excavation, which represents the level of kinetic energy released from the rock failure process. The ejection velocity of the material is commonly much higher than *ppv*, which is also the immediate cause of casualties during a dynamic failure. In hard rock mines, the ejection velocities could be well in excess of 50 m/s (Ortlepp, 1993). However, in contrast to measuring ground motions in mines, it is challenging to directly measure the velocity of the fragment detached from the excavation wall by using seismic sensors.

In early research, there was a common assumption that the ejection velocity is equal to the *ppv* (Wagner, 1984; Roberts and Brummer, 1988). Yi and Kaiser (1993) stated that the rock ejection velocities were less but close to the *ppv* in typical mining conditions. However, as illustrated in Section 2.2.2, seismic energy represented by *ppv* is only an insignificant fraction of the kinetic energy to the failure mass. The main energy sources of kinetic energy during coal bursts are the energy stored in the coal

and rock mass, excessive energy from the soft loading system. Therefore, there may be no direct relationship between ppv and the ejection velocity.

Observations and research show that the ejection velocity varies for ejected materials of different sizes. Mendecki (2016) indicated that for face bursts, driven by sudden loading where rock is shattered into small pieces, the ejection velocity is expected to be a decreasing function of the mass of coal and rock. Kaiser and Cai (2013a) concluded that moment transfer between blocks of rock of different sizes is one of the reasons for velocity difference.

An analytical estimation of ejection velocity was conducted by McGarr (1997), who assumed that slab flexure could be a possible mechanism of rock ejections in mines (see Figure 2-13). When the stress caused by the flexure reaches the uniaxial compression strength S , the slab fractures and unflexes violently. The estimated velocity is:

$$v_{ejection} = \sigma_c \sqrt{\frac{7 - \nu^2}{2\rho Y}} \quad (2-8)$$

where σ_c is the uniaxial compressive stress at failure in Pa, ν is Poisson's ratio, Y is Young's modulus in Pa and ρ is the rock density in kg/m³. Based on this analytical model, a peak velocity of 26 m/s can be expected in a typical rock burst event.

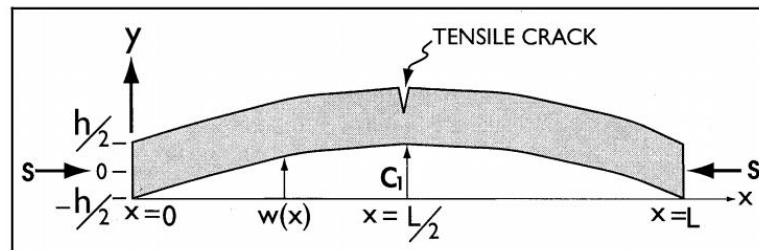


Figure 2-13 A schematic diagram of slab flexure (McGarr, 1997). Slab thickness is h , slab length is L , and the loaded stress is S .

Tannant et al. (1993) determined the ejection velocity of material by back analysing the ejection path taken by the video camera (see Figure 2-14). The ejection velocity can be calculated as:

$$v_{ejection} = \sqrt{\frac{g}{2H\cos^2\theta + D\sin 2\theta}} \quad (2-9)$$

where D and H are the horizontal and vertical distances of the ejected material, respectively, θ is the initial angle of motion measured upwards from the horizontal plane, and g is the gravitational acceleration. The ejection velocity of the failure mass in the test mine site ranged from 1 to 17 m/s (Tannant et al., 1993).

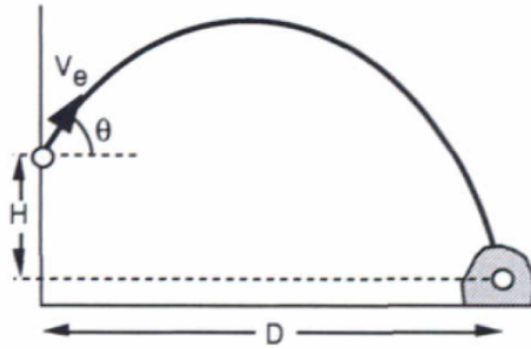


Figure 2-14 A schematic diagram of the ejection path of a rock fragment on the side wall (Tannant et al., 1993). D and H are the horizontal and vertical distances of the ejected material, respectively, θ is the initial angle of motion measured upwards from the horizontal plane, and g is the gravitational acceleration.

Kaiser et al. (1996b) classified the burst damage by combining the mass and ejection velocity, which can guide the support design in burst-prone mines (see Table 2-8). The calculation of kinetic energy in Table 2-8 is based on the assumption that the excavation is unsupported. The result shows that for a given failure mass, higher ejection velocity means higher damage potential and stronger support requirement.

Table 2-8 Kinetic energy and damage intensity as a function of mass and velocity in hard rock mines (Kaiser et al., 1996a)

Mass	Ejection velocity			
	<1.5 m/s	<3 m/s	<5 m/s	<8 m/s
<700 kg/m ²	<1 kJ/m ² (low)	<3 kJ/m ² (low)	<9 kJ/m ² (moderate)	<22 kJ/m ² (high)
<2000 kg/m ²	<2 kJ/m ² (low)	<9 kJ/m ² (moderate)	<25 kJ/m ² (high)	>50 kJ/m ² (extreme)
<4000 kg/m ²	<5 kJ/m ² (low)	<18 kJ/m ² (high)	<50 kJ/m ² (very high)	>50 kJ/m ² (extreme)

Notes: damage intensity classification is based on the kinetic energy (kJ/m²), where smaller than 5 is low, 5 to 10 is moderate, 10 to 25 is high, 25 to 50 is very high, and larger than 50 is extreme.

2.4 Variations of mining-induced seismicity and applications in assessing dynamic failure risks

2.4.1 Event counts and seismic energy variations

As a simple seismic indicator, the variation of event counts and seismic energy can reflect the stress condition and fracture growth in rock mass (Brady, 1977; Srinivasan et al., 1999; Gibowicz and Lasocki, 2001). Analysing the event counts and seismic energy, referred to as variations of seismicity, is the most popular method for assessing coal burst risks in underground mines. Compared to other seismic methods, analysing the variations of seismicity only uses basic parameters of seismic data, i.e. onset time, location and energy of seismic sources, which is easier to use and more tolerant of data quality. A deep understanding of the characteristics of seismic event counts and seismic energy before the impending dynamic failure is essential for burst control and hazard management in underground mines.

Intensive research has been conducted to use temporal and spatial variations of seismicity as precursors to forecast coal bursts and rockbursts. In the space domain, the variation of seismicity has been widely used to locate potential burst damage zones in roadways. In time sequence, it is believed that there is an anomaly of variation of seismicity prior to the burst event, i.e. the seismic event counts first increase and are then followed by a dramatic decrease to a low level before rock failure (Brady, 1978). The low level of event counts during this period is commonly called a “quiet period”. This phenomenon is illustrated as the formation of the damage zone in rocks and the acquisition of the maximum strain energy density (Brady, 1977), which has been observed in both underground mines and earthquake studies (Potvin and Hudyma, 2001; Singh et al., 2010; Li et al., 2016; Liu et al., 2018). Brady and Leighton (1977) examined the seismic data in a burst-prone mine, which showed 188 seconds of increasing seismicity and 65 minutes of decreasing seismicity before a rockburst (see Figure 2-15). However, Cao et al. (2016) observed an opposite phenomenon in a burst-prone coal mine, where the event counts firstly decreased and then increased before the occurrence of the coal burst (see Figure 2-16). This observation is also supported by Srinivasan et al. (1999), who stated that a distinct and rapid increase in event counts commonly precedes a rockburst in gold mines. Also, a downward transfer of signal frequency of the seismic events may indicate a time-dependent growth in rock failure volume.

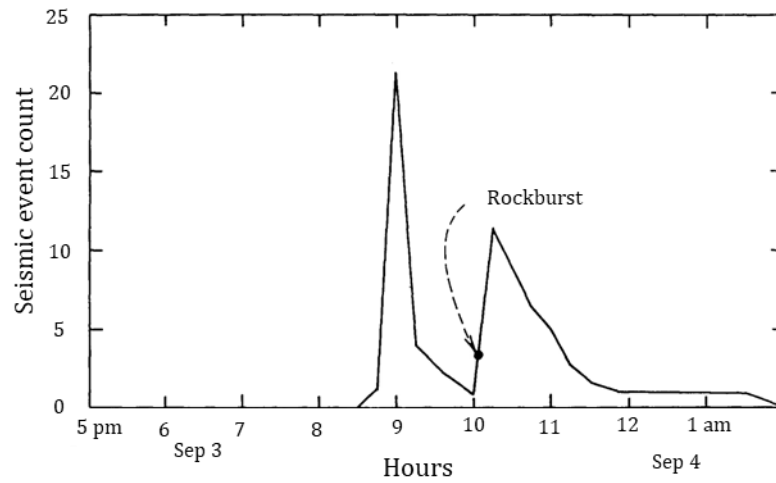


Figure 2-15 Variation of seismic event counts before a rockburst in a hard rock mine (Brady and Leighton, 1977)

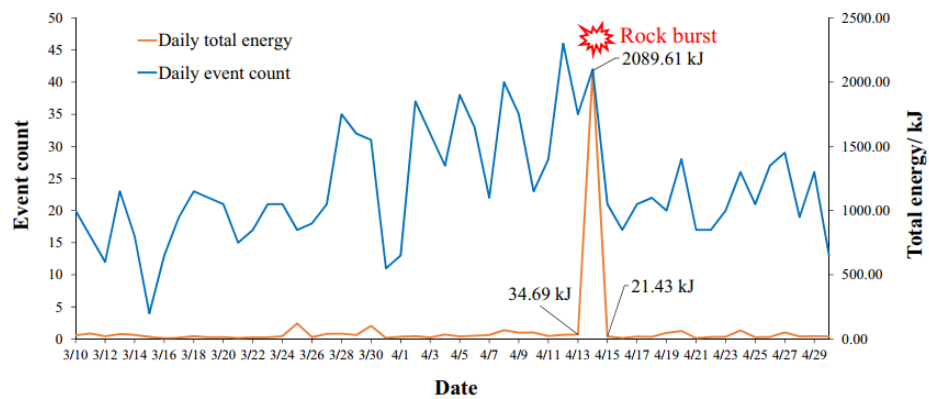


Figure 2-16 Variation of event count and seismic energy before a coal burst in an underground coal mine (Cao et al., 2016)

According to the research findings above, it is still challenging to use temporal variations of seismicity as efficient precursors for burst hazard assessment. The temporal anomaly in seismicity is not a sufficient condition for an impending failure, leading to serious false alarms, and its duration varies from seconds to weeks, depending on different scales, rock types and site conditions (Brady, 1977; Feng et al., 2012). Also, mining operations that control rock failure are a type of intermittent behaviour. The coal bursts triggered by mining operations thus commonly have

strong temporal randomness. As a result, more effort has to be made to accurately forecast burst occurrence using temporal variations of seismicity.

In the space domain, the variation of seismicity has been widely used to locate potential burst damage zones in roadways. It is based on laboratory tests where unstable cracks start to interact and propagate when the rock is loaded to 70%–80% of the peak strength, which is a precursor to the impending rock failure (Martin, 1993). Liu et al. (2018) plotted seismic event density around a developing tunnel to demonstrate the degree of concentration of microcracks and forecast burst risk regions. The result showed that the studied rockburst occurred within the high event-density area, which proves the accuracy of using spatial seismic counts as risk precursors (see Figure 2-17). Wang et al. (2018) investigated the spatial evolution of seismic energy before a coal burst in a longwall. The research indicated that the nucleation of seismic energy in the syncline region was generated, and the energy intensity kept increasing before the coal burst hazard. The zone with the highest seismic energy intensity can well identify the coal burst event (see Figure 2-18). Based on the spatial variation of seismicity, several seismic methods have also been further developed, such as clustering analyses, fractal dimensions (Xie and Pariseau, 1993), spatial bursting energy index (Cai et al., 2019) and spatial b-value distribution (Wesseloo et al., 2014), with encouraging results in underground mines.

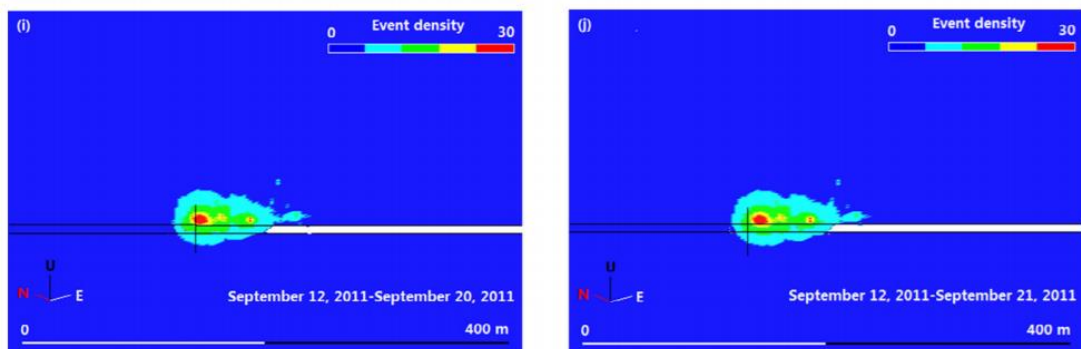


Figure 2-17 Density contours of seismic event counts around a tunnel (Liu et al., 2018)

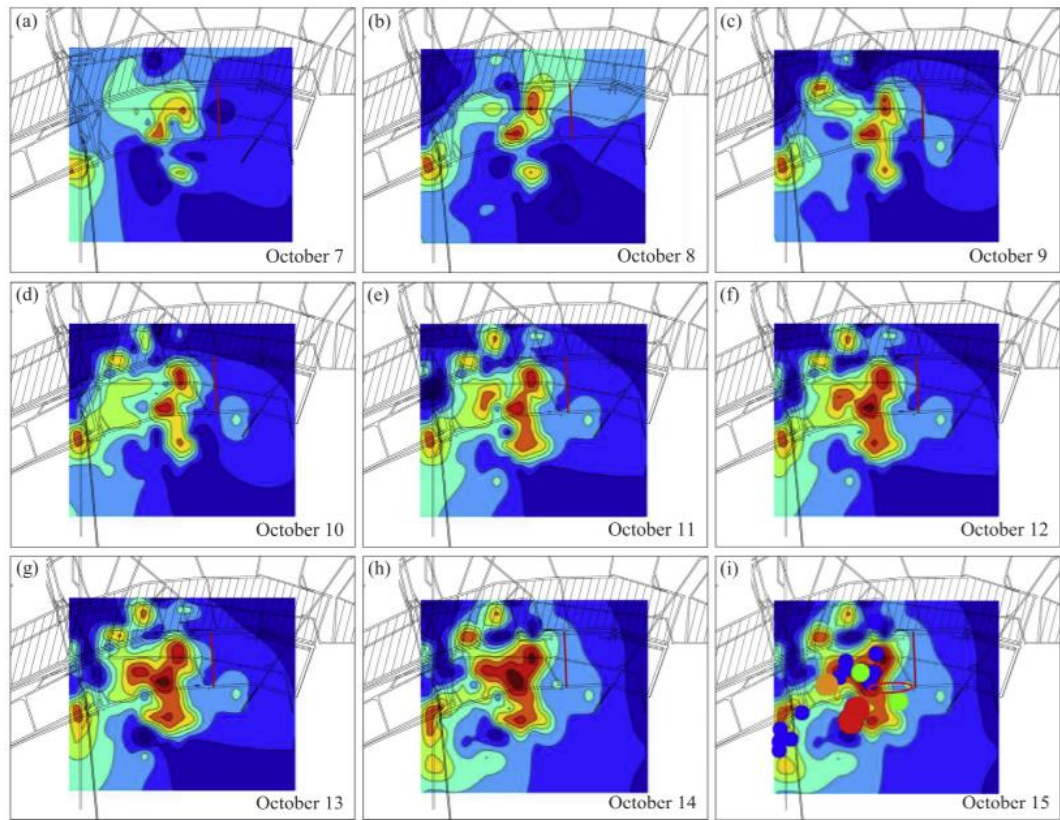


Figure 2-18 Spatial evolution of seismic energy before a coal burst occurred in a longwall (Wang et al., 2018)

However, similar to other seismic methods in coal mines, there may be low accuracy in analysing the spatial variation of seismicity if the seismic monitoring quality is poor. There are two main factors contributing to seismic monitoring quality: location errors and seismic data integrity. In coal mines, the location errors of horizontal coordinates are about 50 m, while errors can be up to 100 m for vertical coordinates (Stec, 2007; Gong et al., 2010b). Also, the adverse layout of geophones in coal mines commonly leads to poor seismic data integrity. The magnitude of completeness (m_c), which is the minimum magnitude of events that can be fully recorded by the system, commonly has high values and varies in space within a coal mine. Thus using incomplete seismic data is highly likely to induce a bias in event counts related analyses. Therefore, location errors and seismic data integrity should be considered in analysing spatial variations in seismicity.

2.4.2 Seismic clusters

In underground mines, the clustered seismic events are the evidence of unstable energy release caused by fracturing in highly stressed rock mass and failure of geological structures (Falmagne, 2002; Vasak et al., 2004; Kaiser et al., 2005; Hudyma, 2008; Woodward et al., 2017). In laboratory tests, the onset of unstable crack growth and fracture interaction, represented by the clustering of acoustic emission signals, is usually at about 70%~80% of the uniaxial compression strength (UCS) of the rock sample (Martin, 1993; Eberhardt et al., 1999). The rock mass strength is commonly far lower than the UCS due to natural jointing, fracturing and other factors. Therefore, the clustering phenomenon of seismic events can be regarded as a precursor of rock failure around the mine opening (Martin and Young, 1993). Besides the high stresses, the clustering of seismic events is also an indicator of undetected geological structures in rock mass, such as joints and minor faults. Based on the failure mechanism, Vasak et al. (2004) identified four typical failures and the associated seismic clusters around excavations during mining (see Figure 2-19). The propagation, connection and excavation intersecting geological structures can be illustrated by the clustering of seismic events. The geological structures near the excavations are locally less restrained and free to slip. Dynamic failure under such a condition is easily triggered due to the increasing displacement potential and associated energy release in geological structures (Diederichs, 2014; Cai and Kaiser, 2018).

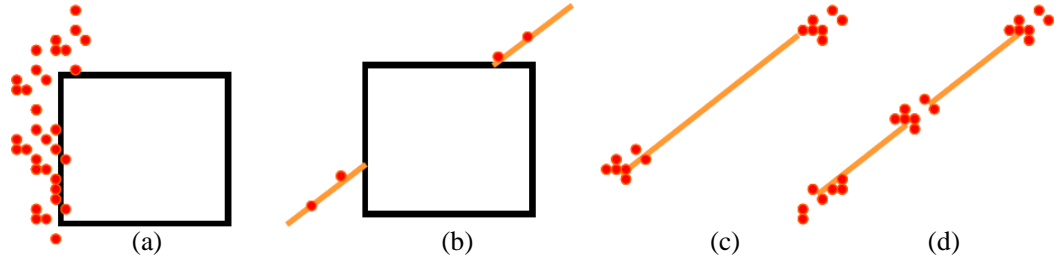


Figure 2-19 Four micro-seismic examples of rock mass failure (Vasak et al., 2004): (a) stress related, (b) excavation intersecting weak planes, (c) weak plane propagation, (d) rock bridge failure. The black rectangle is the excavation boundary, red dots are induced seismic events, and the orange line is the discontinuity in the rock mass.

Falmagne (2002) developed a seismic clustering method based on the source size and the distance between seismic events. Two seismic events are regarded as clustered if their distance is lower than twice of their radii sum. The clustering degree between event i and event j is evaluated using the Cluster Index Function:

$$\text{Cluster Index Function} = \frac{1}{2} \left[1 + \cos \left(\frac{\pi}{2} \times \frac{d_{ij}}{r_i + r_j} \right) \right] \quad (2-10)$$

where r_i and r_j are the source sizes of the two seismic events, i.e., the source radius. Figure 2-20 shows the relationship of the Cluster Index Function with the distance between events and the source sizes. The method was applied to seismic data in the Underground Research Laboratory in Manitoba, Canada, and the results showed a good correlation with rock degradation.

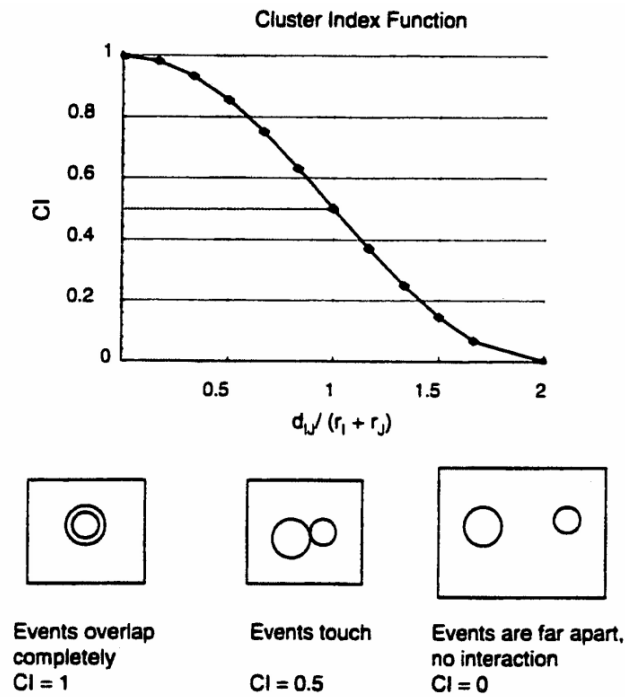


Figure 2-20 Relationship of the cluster index function with the distance between two events and the source size (Falmagne, 2002)

The Density-Based Spatial Clustering of Applications with Noise (DBSCAN) method was first proposed by Ester et al. (1996), and aims to identify various clusters of an arbitrary shape from a large dataset. In DBSCAN, data points are classified as core, border and noise, which considers the number of neighbouring points within a given searching radius (see Figure 2-21). DBSCAN has been widely used in earthquake studies to identify major seismic sources (Georgoulas et al., 2013; Karri et al., 2018). Woodward et al. (2018) proposed a modified DBSCAN method to identify seismic clusters in underground mines, which addressed the limitations in clustering varying-density seismic data and the high sensitivity to parameter selection (see Figure 2-22). The method was shown to be a robust approach to spatially describe mining seismicity characteristics in the short term.

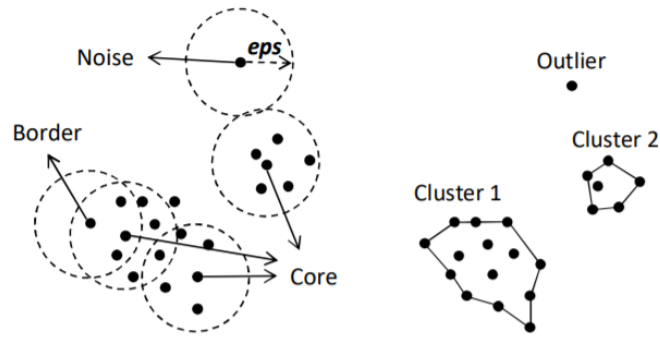


Figure 2-21 An example of data clusters using DBSCAN (Rezaei, 2016)

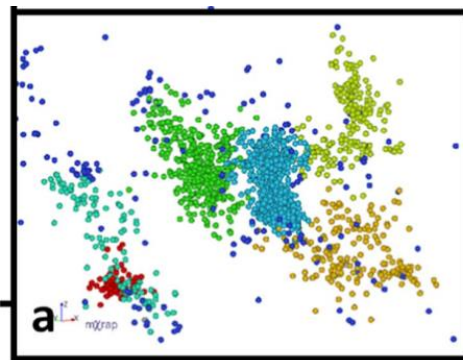


Figure 2-22 Mining-induced seismicity in a tested mine clustered by the modified DBSCAN method (Woodward et al., 2018). Blue dots are the noise events, dots with other colours are events in different clustering groups.

Hudyma (2008) proposed a two-pass seismic clustering method called Comprehensive Seismic Event Clustering (CSEC), which aims to identify the seismic sources with different source mechanisms from vast seismic data. In this method, a compact-linkage (CLINK) clustering routine was first used to classify seismicity into a large number of small clusters with similar source parameter characteristics. Then, the single-link clustering method (SLINK) is applied further to integrate the small clusters into different seismic sources (see Figure 2-23). The method has been used in several underground mines and shown to be a powerful tool in mapping seismic hazards.

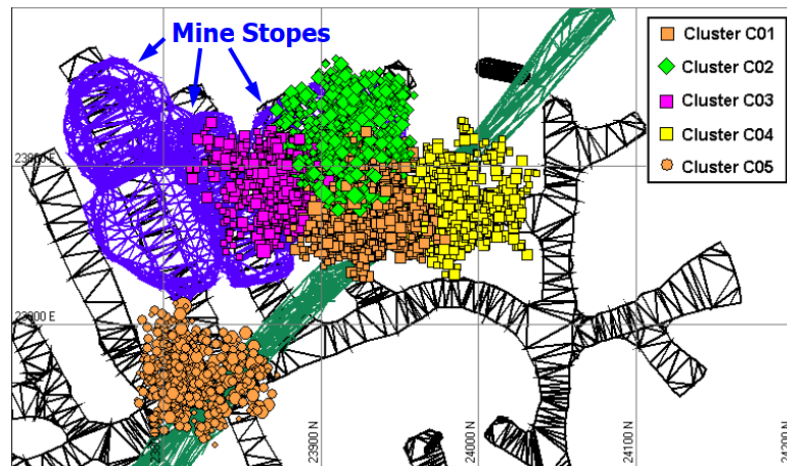


Figure 2-23 Five seismic clusters identified in the stoping area by using the CSEC method (Hudyma, 2008)

A sequential spatial clustering method was developed by Cortolezzis (2018) to show the temporal evolution of seismic clusters during the mining progress. Unlike the other spatial clustering method, the entire development progress of a seismic cluster can be investigated without determining a study time frame (see Figure 2-24). The method was expected to provide insight into investigating rock failure characteristics and assessing seismic hazards during caving mining.

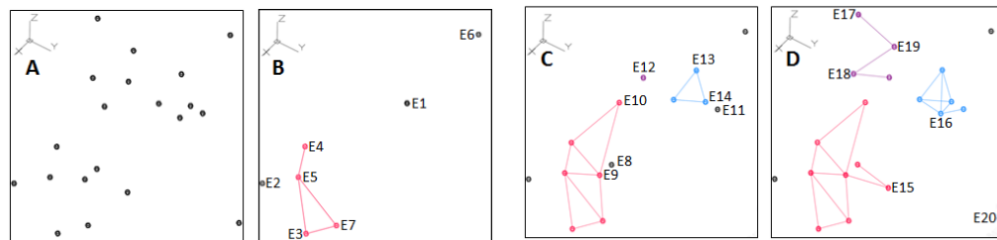


Figure 2-24 An example of the temporal evolution of seismic clusters by using the sequential spatial clustering method (Cortolezzis and Hudyma, 2018)

2.5 Seismic monitoring capability

2.5.1 Location errors

As event locations are the basic input parameters for most of the seismic methods, the accuracy of locating seismic events is the prerequisite to ensure high performance in forecasting seismic hazards. Therefore, how to evaluate the location errors during underground mining and eliminate their impacts on seismic analyses has become an urgent problem that needs to be addressed. Gibowicz and Kijko (1994) stated that the location errors of seismic events are at the order of 20–50 m or 50–100 m, depending on the number of seismic sensors and the network size and geometry. In the Upper Silesian Coal Basin in Poland, the location error of horizontal coordinates is 50 m, while it can be up to 100 m for vertical coordinates (Stec, 2007). The epicentre errors of monitoring systems in one Canadian mine and one South African mine range from 4 m to 61 m, with an average of 15 m to 23 m (Kijko and Sciocatti, 1995), respectively. Gong et al. (2010b) optimised the number of geophones for seismic monitoring in underground mines and analysed the spatial location errors of a Chinese coal mine, which appeared to be approximately 50 m. Since the errors are non-negligible compared to the size of mining excavations, not considering significant location errors is highly likely to cause false results for seismic clustering analysis.

Errors in picking the arrival time of seismic waves and unfavourable sensor layout are two possible reasons for location errors of seismic events. As the arrival time is manually picked in field monitoring in most cases, the wave-picking error depends on the experience of individual seismologists and cannot be eliminated. Zhu et al. (2018) conducted a numerical study to evaluate the impact of wave-picking errors on the accuracy of locating a seismic event. The results showed that the location errors vary with different sensor locations and wave-picking errors. The

location errors can be nearly 25 m when the wave-picking error reaches ± 5 ms. Zhang et al. (2019) discussed the location errors of seismic events in the excavation where the zone cannot be fully enclosed by sensor arrays and found that the twin-tube sensor array in the excavation provides better performance in locating accuracy, achieving errors less than 10 m in locating events (see Figure 2-25).

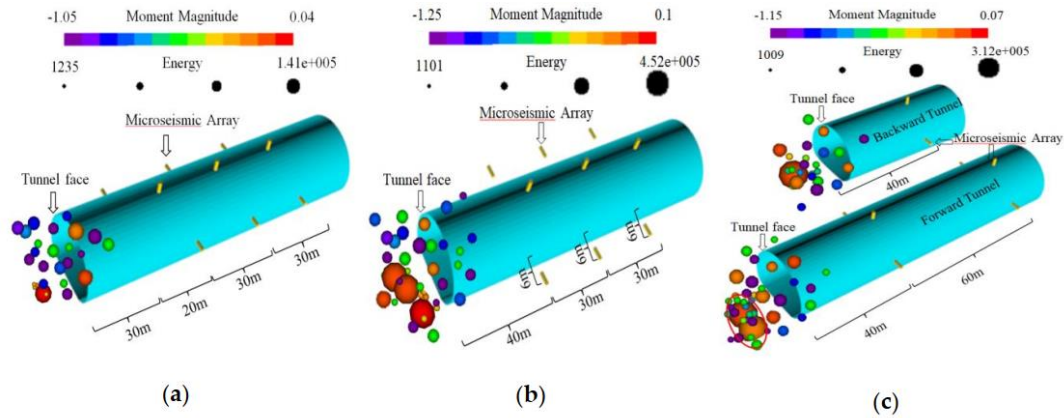


Figure 2-25 Three sensor arrays in a tunnel: (a) axial-extended array, (b) lateral extended array, and (c) twin-tube array (Zhang et al. (2019))

However, the location results of seismic events can be highly ambiguous because of the flatness of the geophone array, complex geological structures and intense extraction in underground coal mines (Leśniak and Pszczoła, 2008). In order to systematically evaluate the location errors, Dębski and Klejment (2016) proposed a new method called the TRMLOC algorithm, which uses the Bayesian inversion technique to explore the spatial distribution of source locations. Compared with the classical error analysis approaches, the new method provides a much faster calculation by eliminating the onset time of seismic sources in the inversion process. However, it is still challenging to evaluate the location errors due to the lack of knowledge on the observational and modelling uncertainties. Such uncertainties were investigated by Debski (2015), who found that the limitations of a priori on the likelihood function may significantly influence the estimation results. Based on the onset time and wave propagation angle of the seismic sources captured by triaxial

sensors, Leśniak (2015) optimised the configuration of the seismic network to reduce the location errors. The results showed that the best source location for a seismic sensor is the one with minimal average location errors. For a seismic monitoring system with uniaxial sensors only, multiple solutions may occur due to the lack of 3D seismic waves when using the arrival-time-difference method to locate events. Li et al. (2014) classified those multiple solutions into two types: same onset time and different onset time. It was found that there is a relation between sensor layout in underground mines and the multiple locating solutions. Li et al. (2014) also emphasised that an optimised network will not only reduce the possibility of multiple locating solutions but also increase the locating accuracy.

2.5.2 Completeness of seismicity catalogue

One of the main aspects in appraising seismic data reliability is data integrity. Due to complex geological conditions and intensive mining activities, seismic signals are recorded in a spatially and temporally heterogeneous underground environment. The seismic monitoring network is usually constrained by the layout of underground excavations. Thus, it is a challenge to ensure an identical detection probability that covers the entire area of interest. On the other hand, seismic signals always contain uncertainties or errors since they are manually processed based on personal experience with varying assumptions. Such uncertainties may induce bias on seismic observations with a large variety in space and time (Woessner and Wiemer, 2005). Most of the seismic analyses applied in mines are statistical analyses, but few consider the impact of an incomplete seismic dataset on result interpretation. The negligence of seismic data integrity could significantly reduce the accuracy of the data interpretation. Therefore, an approach to assess seismic data integrity of seismic monitoring systems applied in underground mines needs to be developed.

In the earthquake engineering community, the magnitude of completeness, m_c , is commonly used to evaluate seismic data integrity. It is based on the assumption

that for the seismicity in a given volume, a simple power-law function can describe the frequency and magnitude distribution (*FMD*) relationship of seismic events (Ishimoto, 1936). The relationship is called the Gutenberg–Richter law, which is defined as:

$$\log_{10}N(M) = a - bM \quad (2-11)$$

where $N(M)$ is the frequency of earthquakes with magnitudes larger than or equal to M . a and b are constants, which are usually estimated by using the maximum-likelihood estimation (Gutenberg and Richter, 1944; Aki, 1965; Utsu, 1965). b -value is calculated as (Aki, 1965; Bender, 1983):

$$b = \frac{\log_{10}(e)}{[\langle M \rangle - (m_c - \Delta M_{bin}/2)]} \quad (2-12)$$

where $\langle M \rangle$ is the mean magnitude of the earthquake catalogue, and ΔM_{bin} is the binning width of the earthquake catalogue. m_c is defined as the minimum magnitude at which the cumulative *FMD* departs from the exponential decay, which is a key indicator for assessing the seismic data integrity (Zúñiga and Wyss, 1995). An example of the *FMD* curve and m_c for an earthquake catalogue is presented in Figure 2-26.

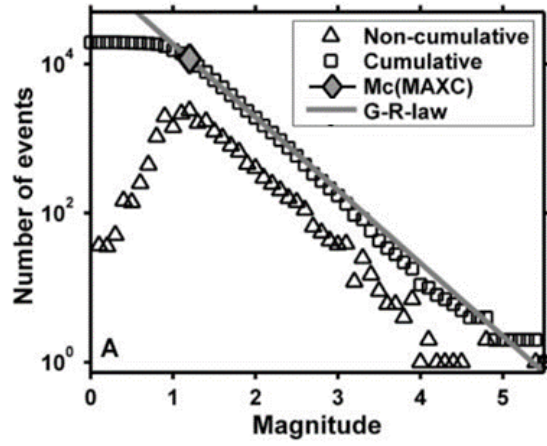


Figure 2-26 *FMD* and cumulative *FMD* of an earthquake catalogue recorded by the Northern California Seismic Network (Woessner and Wiemer, 2005)

As m_c is essential for statistical studies in seismology, research has been conducted to determine a reliable m_c value. Ogata and Katsura (1993) established a statistical model using the Objective Bayesian Method to investigate the variations of b-value and detection rate of the earthquake catalogue. The model results provided insights into studying the relationship between the configuration and sensitivity of seismic sensors in a seismic network. Based on this model, Woessner and Wiemer (2005) developed the Entire Magnitude Range method (EMR) to model the incomplete part (with magnitude $< m_c$) and the complete part (with magnitude $> m_c$) of the frequency-magnitude distribution. The normal cumulative frequency-magnitude distribution of the earthquake catalogue $q(M|\mu, \sigma)$ is calculated as:

$$q(M|\mu, \sigma) = \begin{cases} \frac{1}{\sigma\sqrt{2\pi}} \int_{-\infty}^{m_c} \exp\left(-\frac{(M-\mu)^2}{2\sigma^2}\right) dM, & M < m_c \\ 1 & M \geq m_c \end{cases} \quad (2-13)$$

where μ is the magnitude where half the earthquakes are detected, σ is the standard deviation representing the width of the incomplete earthquake magnitude detection range. Based on the self-similarity assumption in the earthquake catalogue,

Wiemer and Wyss (2000) proposed the maximum curvature method (MAXC) to achieve fast estimation of m_c . In this method, the m_c is the maximum value of the first derivative of the frequency–magnitude distribution curve. However, such a calculation may underestimate m_c as the real m_c may be higher than the lower limit of the magnitude bin with the maximum first derivative (Schorlemmer and Woessner, 2008). Cao and Gao (2002) estimated m_c using b-value stability as a function of the cut-off magnitude, and the signal-to-noise ratios of seismic waves were used to investigate the detection capability of individual stations. To assess the seismic data integrity, Schorlemmer and Woessner (2008) proposed a method for calculating the earthquake detection probabilities rather than estimating m_c , which is related to the wave picking and the seismic network configuration. It was found that seismic data integrity is a function of network properties instead of seismic data samples.

Although the above methods, referred to as conventional m_c methods, have been widely used to assess data integrity in earthquake studies, their applications in underground mining are still rare. Due to the complex geological and mining conditions, the frequency–magnitude distribution in underground mines may not follow the self-similarity assumption. A case study of the seismic data catalogue characteristics in a hard rock mine was conducted by Woodward and Tierney (2017). The cumulative frequency–magnitude distribution shown in Figure 2-27a presents a bimodal curve with two possible m_c , which may indicate that the seismic data originated from two different sources. Therefore, Woodward and Tierney (2017) categorised the mining-induced seismicity into two different sources using an artificial neural network, and a power-law data curve is present in each source (see Figure 2-27b).

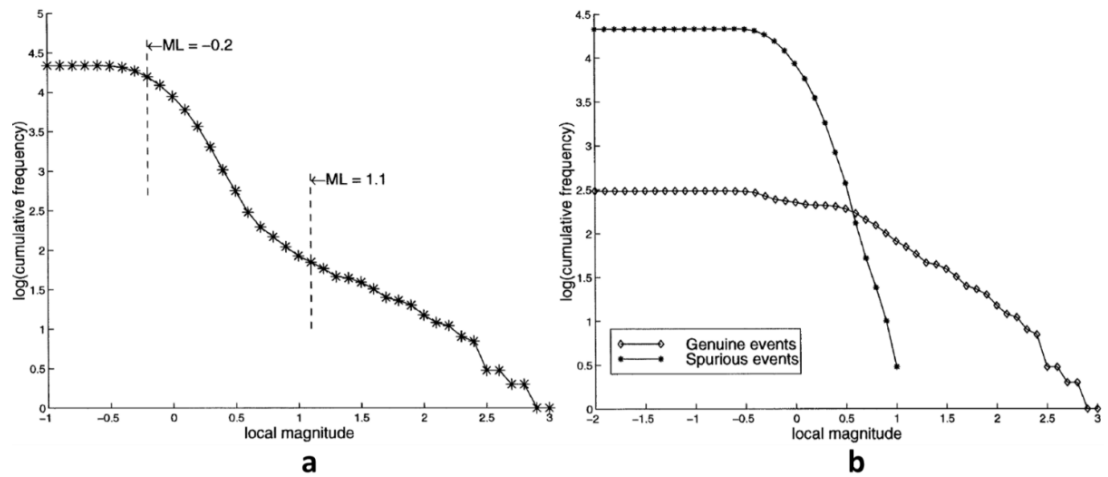


Figure 2-27 Cumulative *FMD* in an Australian underground mine using (a) all seismic events and (b) the seismic events from two different sources (Woodward and Tierney, 2017)

To ensure the detection consistency of seismic events in a given area of interest, a conservative strategy is commonly adopted, which only uses seismic events with magnitudes larger than m_c (Woessner and Wiemer, 2005). However, if a relatively high magnitude of m_c is observed, seismic events with energy below m_c would be discarded for further seismic analyses, which causes significant data to be wasted. Also, to ensure reliability and accuracy, m_c can only be calculated in the region where adequate seismic events have been monitored. Thus, in underground mining, the m_c results can be highly sensitive in the area where only sparse seismic data are collected.

2.6 Summary

In this chapter, the literature relevant to the scope of this thesis was reviewed and summarised. To understand dynamic failure in underground mines, the mechanism and classification of coal bursts and rockbursts were first demonstrated. The dynamic impact of seismic waves on the rock mass was also presented. Then, the principles and applications of using mining-induced seismicity to assess coal

burst risks were introduced. Finally, the deficiencies of current seismic monitoring techniques for dynamic hazard forecasting were revealed.

Based on the damage mechanism and energy sources, coal bursts and rockbursts can be classified as direct bursts and indirect bursts. The excessive strain energy released in the loading environment is the primary energy source for both burst types. Seismic energy transmitted via strong ground motions is the additional energy source for indirect bursts. According to the distance from the seismic source, the ground motions induced by seismic waves can be distinguished as far-field and near-field motions. Since near-field ground motions may cause enormous vibrations and potential damage to underground openings, their characteristics need to be investigated in ground motion analysis to prevent burst hazards.

Ground motions are not directly related to the ejection velocity. The seismic energy transmitted via ground motions only constitutes a small fraction of the kinetic energy to the failure mass. The main energy source of kinetic energy during the dynamic failure is the energy stored in the coal and rock mass, excessive energy from the soft loading system.

Since dynamic failure triggered by mining operations has highly temporal randomness, it is more applicable to use the spatial variation of seismicity for a robust dynamic failure assessment. Seismic clustering analysis can spatially locate the energy release of unstable fracturing in highly stressed rock mass and failure of geological structures, which can be a powerful tool for burst hazard prediction.

The inherent location errors and poor seismic data integrity are the two main deficiencies of seismic monitoring in underground mines. Inaccurate seismic event location and an incomplete seismic dataset may significantly reduce the accuracy of data interpretation. Therefore, the characteristics of location errors and seismic data

integrity in underground mines should be investigated and considered in seismic analyses.

In conclusion, the literature review has demonstrated several research gaps that need to be addressed to better understand the dynamic failure mechanism and enhance the performance of seismic analyses in hazard forecasting. More studies have been conducted in hard rock mines than in coal mines. However, due to the differences in the mining methods and mechanical properties of the materials, the burst risk criteria determined in hard rock mines cannot be directly applied to coal mines. Therefore, in the following chapters, a detailed analysis is conducted in a coal mine to investigate the characteristics of ground motions and the induced seismic impacts. The characteristics of location errors and seismic data integrity are also studied and used to improve the data quality for seismic analyses.

Chapter 3. Geological and seismic characteristics of the study site-Huating Coal Mine

3.1 Introduction

As illustrated in Chapter 1 and Chapter 2, due to a lack of understanding of seismic impacts on coal burst damage and unsatisfactory seismic monitoring performance, it is challenging to conduct effective seismic analyses for hazard forecasting and control. To investigate these key issues, field monitoring data in real underground coal mines are vital to link seismic analysis results with the actual burst damage. Although hazardous coal burst damage is undesirable, past seismic recordings and detailed descriptions of coal bursts in mines can provide invaluable resources for back analysis. Therefore, this thesis is based on field observations of seismic data from a burst-prone underground coal mine, Huating Coal Mine, in Gansu Province, China. Due to the complex geological and mining conditions, the coal mine has reported more than 200 coal bursts since 2008. This chapter presents an overview of the case study site, longwall (LW) 250105 in Huating Coal Mine including its geology, mining method, seismic activities and coal burst records.

3.2 Geological and mining conditions

According to the regional *in-situ* stress measurements at the case study site, Huating Coal Mine, the *in-situ* stress is dominated by the horizontal stress in this mine, which is approximately 1.2 times the vertical stress (Ju et al., 2019). The target coal seam to be extracted is the No. 5 Coal Seam, which is 550 to 800 m deep with a dip angle of between 1° and 15°. The coal seam has an average thickness of about 40 m. Thus, it is designed to be mined out in three slices, and the longwall top coal caving method is used for each layer (see Figure 3-1). A mechanical property test

and coal burst liability assessment have been conducted for the No. 5 Coal Seam. The results in Table 3-1 show a high burst liability due to the short dynamic failure time, high elastic energy index and high impact energy index (Cai et al., 2016).

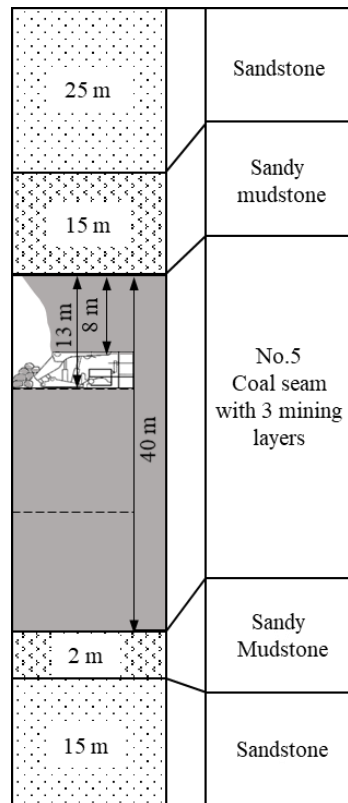


Figure 3-1 Stratigraphic column in LW250105 area (Wang et al., 2021)

Table 3-1 Mechanical properties and coal burst liability of No. 5 Coal Seam in Huating Coal Mine (China University of Mining and Technology, 2016)

Uniaxial compression strength (MPa)	Density kg/m ³ (ρ)	Elastic modulus (E)	Shear modulus (G)	Dynamic failure duration D_{τ} (ms)	Bursting energy index K_E	Elastic strain energy index W_{ET}	Coal burst liability
13.7 MPa	1320	3 GPa	1.15 GPa	2,640	6.67	10.1	High

The study longwall panel LW250105 is an upper layer panel of the No. 5 Coal Seam extraction, with a length of 2,000 m and a width of 200 m (see Figure 3-3). The panel started to retreat from the start-up position in March 2014 and stopped at the

completion position in May 2016. LW250105 is overlaid by 15 m of thick sandy mudstone and 25 m of sandstone. The mining height in each layer is 13 m, including 5 m in cutting and 8 m in caving (see Figure 3-1). Different from conventional mine designs, the LW250105 tailgate was developed using the “gob-side entry driving” method (GED), which is shown in Figure 3-2. The GED method aims to reduce coal losses in wide chain pillars to fulfil the minimum recovery ratio requirement set by the Chinese government (Wu et al., 2018). As a result, only a 6 m-wide rib pillar was left between the LW250105 tailgate and the goaf created by the previous longwall panel, LW250103 (see Figure 3-3). The rib pillar had limited loading capacity and was mainly used to insulate the tailgate and the goaf. The rib pillar width was determined based on the distribution of abutment stresses induced by panel retreating on the goaf-side coal seam. The tailgate was designed to locate in the “destressed zone” to avoid stress-induced damage and ensure its stability (Bai et al., 2015). Although the GED method has been applied in several Chinese coal mines (Jia et al., 2014; Qian et al., 2014), LW250105 tailgate still had a high burst risk under dynamic pressures from breaking strata and strong ground motions.

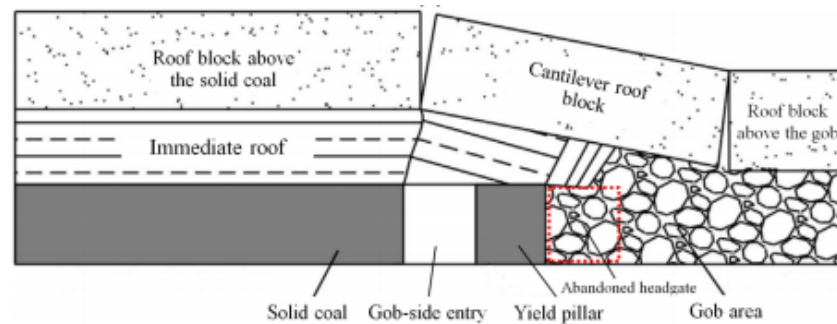


Figure 3-2 An example illustrating the gob-side entry driving (GED) method (Wu et al., 2018)

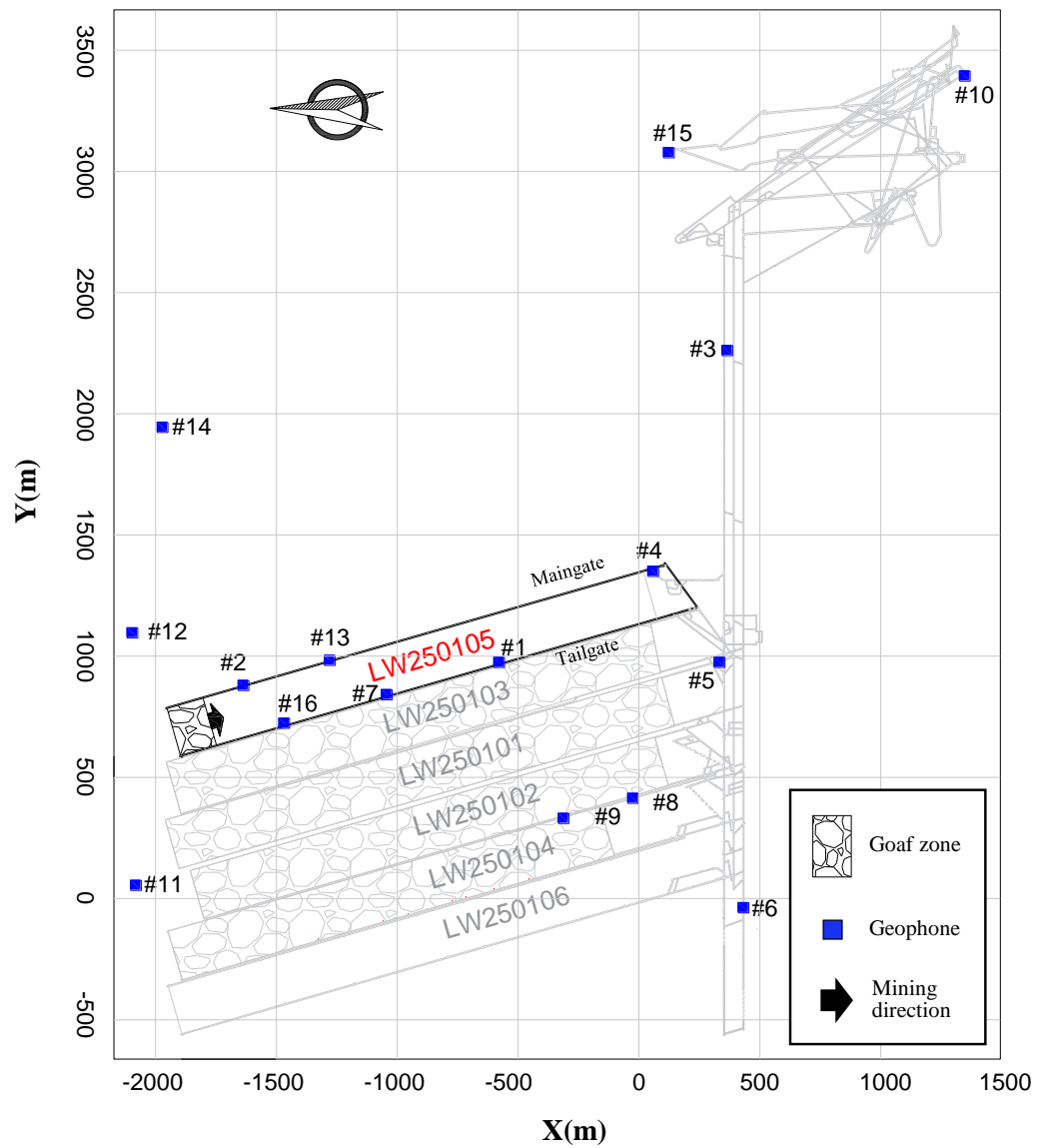


Figure 3-3 LW250105 layout and geophone distribution in Huating Coal Mine (Wang et al., 2021)

3.3 Seismic monitoring system

The microseismic monitoring system 'SOS', developed by the Central Mining Institute of Poland, was installed in Huating Coal Mine in 2008 to continuously monitor the seismicity associated with mining activities. SOS has a real-time monitoring recorder, a digital transmission system, an analyser and 16 geophones. The geophones are uniaxial with a detection frequency range of 1–600 Hz, a

sampling rate of 500 Hz, and a maximum data transmission rate of 1 MB/s and 16-bit A/D conversion. The seismic monitoring system was in the commissioning stage in March 2014 and commenced regular monitoring for LW250105 from April 2014. A P-wave velocity of 3,600 m/s was used to locate seismic events. The seismic monitoring system in the Huating Coal Mine only used uniaxial geophones because of a series of challenges, such as intrinsic safety requirements, weak or noisy seismic signals, and timely installation of portable sensors in fast-moving coal mining conditions. The absence of triaxial seismic recordings may cause challenges in computing accurate source parameters.

Two types of geophones were installed underground to monitor the seismicity in LW250105: roadway geophones and distant geophones. Roadway geophones #1, #2, #4, #7, #13 and #16 were placed in both the maingate and tailgate of LW250105. The location of roadway geophones was regularly modified along with the panel retreat during the monitoring period from April to December 2014 (see Figure 3-4). The distance from the longwall face to the nearest roadway geophone is 100~300 m. Being close to the seismically active zone, roadway geophones captured clear waveforms with high signal-to-noise ratios. Hence the roadway geophones are mainly used to locate seismic events by picking up a clear P-wave arrival time (see Figure 3-5a). However, as the high waveform amplitude may be beyond the geophone measurement range of ± 0.64 mm/s, some seismic signals are truncated by the roadway geophones and thus the recorded waveform is incomplete and cannot be used for source parameter calculation.

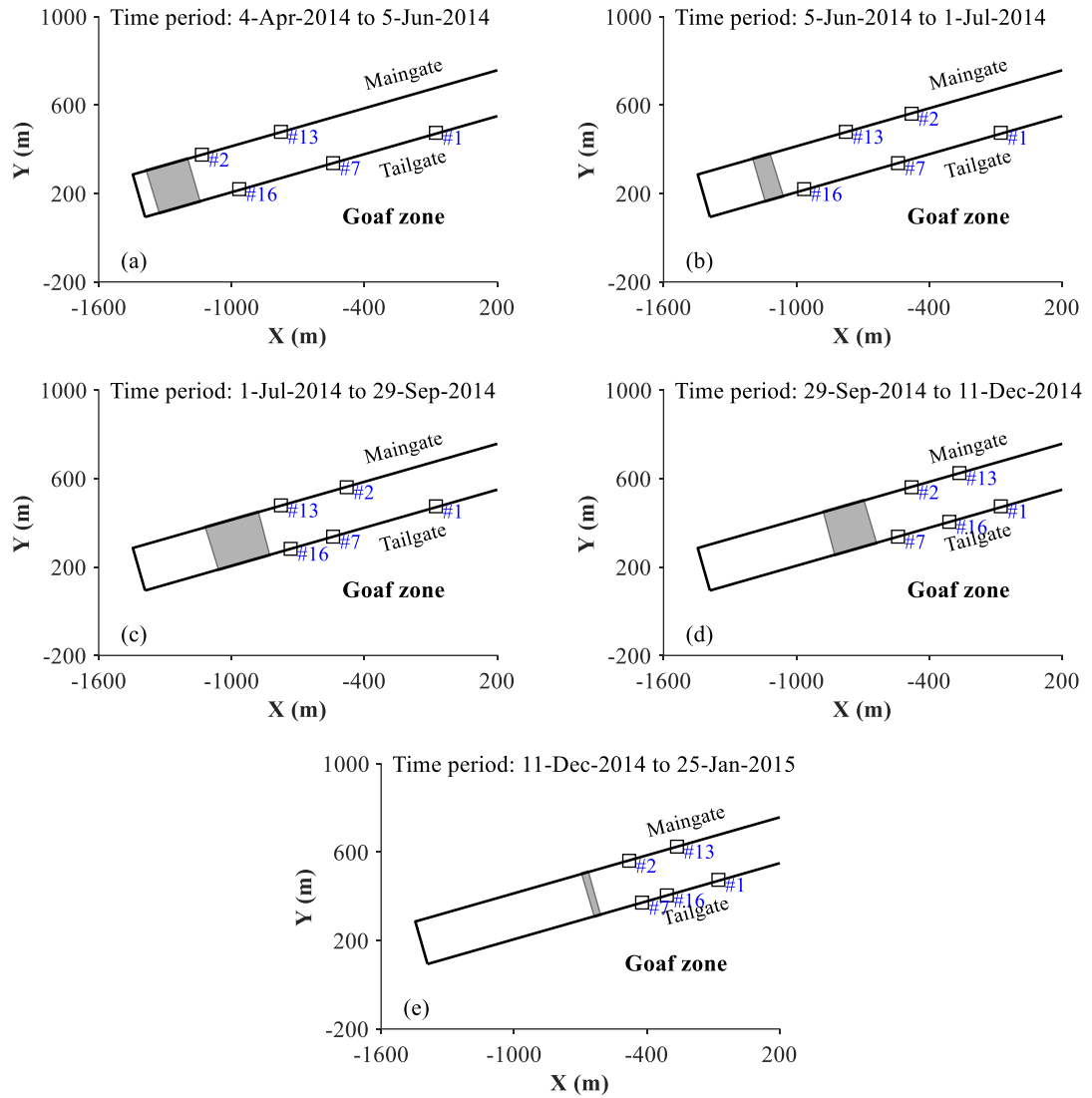


Figure 3-4 Distribution of roadway geophones in LW250105 from April to December 2014. The grey zone is the longwall chainage during the period.

The other ten geophones in the system are distant geophones (geophones #3, #5, #6, #8, #9, #10, #11, #12, #14 and #15), which were installed at different heights in the roof at distances of 2 km to 4 km away to spatially cover the monitored area (see Figure 3-3). Due to the energy attenuation over the long distances, most of the waveforms received by the distant geophones are complete with amplitudes within the geophone measurement range, ± 0.64 mm/s. Thus, distant geophones are mainly used for source parameter calculation. However, the long distance between the panel and goafs also led to blurred waveforms commonly recorded at distant geophones (see Figure 3-5b). Sometimes, these waveforms were unavailable

for event locating because of the low signal-to-noise ratio. During LW250105 retreating in 2014, all roadway geophones were available to locate events. Due to either poor waveform quality or installation problems, only four of the distant geophones (#3, #5, #6 and #11) were working to monitor seismicity in LW250105.

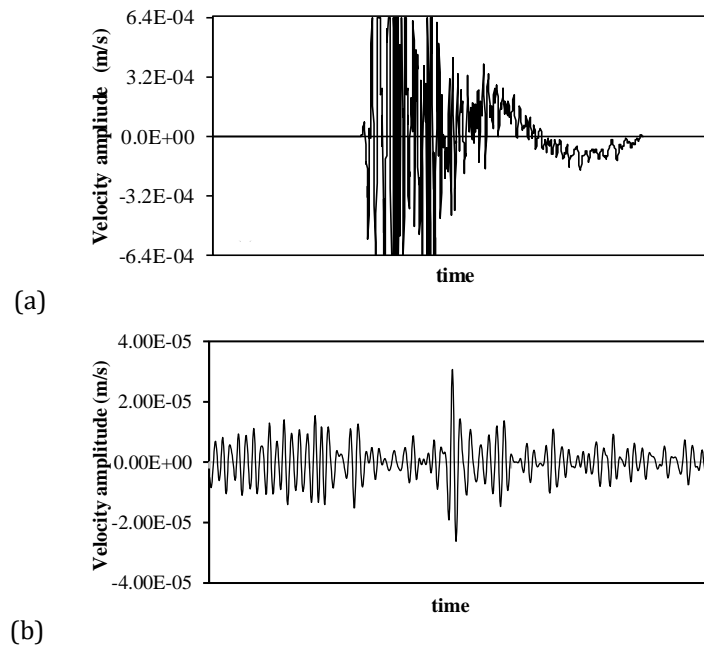


Figure 3-5 Examples of (a) truncated waveforms captured by a roadway geophone and (b) blurred waveforms captured by a distant geophone

3.4 Mining-induced seismicity

In 2014, a total of 11,915 seismic events were detected during LW250105 retreat. Figure 3-6 summarises the energy level proportions of the seismicity, showing that more than 70% of events had energy of 1~100 kJ. The seismic events with energy larger than 100 kJ accounted for less than 5% of the total, but were responsible for most coal burst damage in this longwall.

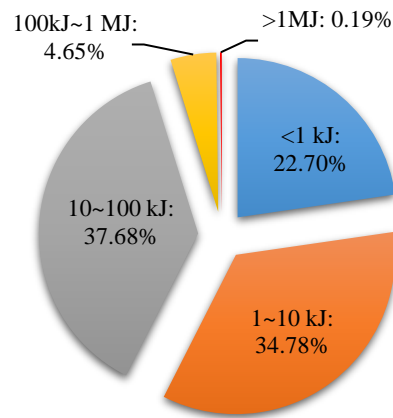


Figure 3-6 Percentage of seismic events at different energy levels in LW250105 recorded during 2014

Figure 3-7 shows the spatial distribution of seismic events during LW250105 retreat in 2014. Since the seismic monitoring system was in the commissioning stage in March 2014, only a few seismic events were detected at about 100 m ahead of the longwall start-up location, and most of them had energy larger than 10 kJ. Regular seismic monitoring in LW250105 commenced from April 2014, and a large number of seismic events were detected with a wide energy range from less than 1kJ to up to more than 10 MJ. Due to the higher abutment stresses induced by the panel retreating on the goaf side, the tailgate has experienced more seismic events with energy over 100 kJ than the maingate has. A clustering phenomenon of high-energy seismic events was also detected in the tailgate with the X coordinate between -1100 m and -900 m, where coal and rock mass were highly unstable and intensive coal burst damage frequently occurred. Figure 3-8 shows the average seismic event counts and seismic energy released per day in front of the longwall face. It can be seen that both frequent seismic events and high-level energy release occurred within about 150 m ahead of the longwall face. The average daily event counts can be up to 17 in the zones of 40–60 m ahead of the longwall face. The highest average energy release occurred in the zone at 60–80 m ahead of the longwall face, where 728 kJ of seismic energy was detected per day. It indicates that

the zones within 80 m of the longwall face were under significant abutment pressure, where critical coal burst risks were also present.

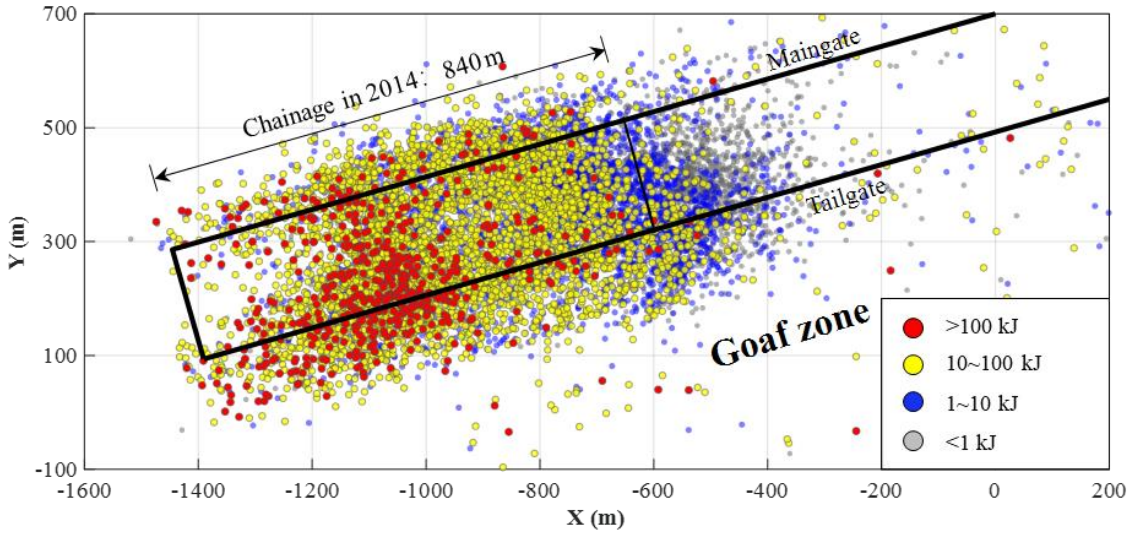


Figure 3-7 Spatial distribution of seismic events with different energy levels in LW250105

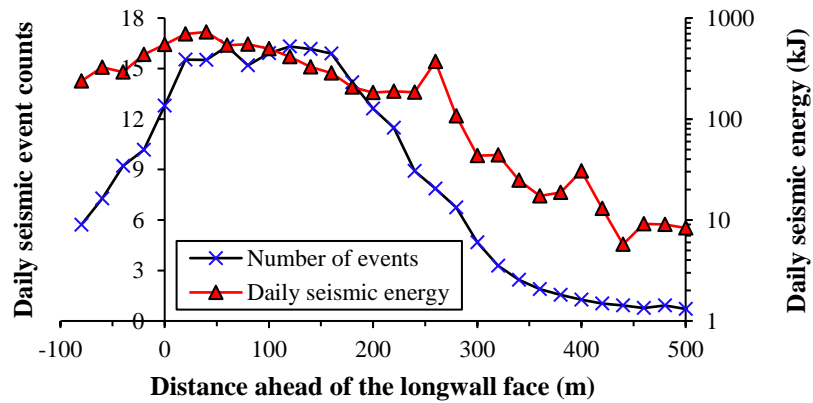


Figure 3-8 Number of daily seismic events and seismic energy ahead of LW250105 face during 2014 (with a distance interval of 20 m)

3.5 Coal bursts

In 2014, a total of 29 coal bursts occurred in the tailgate during LW250105 retreating. Figure 3-9 shows the spatial distribution of these coal bursts and the corresponding zones of damage, and Table 3-2 lists their key characteristics. The coal bursts had seismic energy from 0.053 MJ up to 28.6 MJ, and most of them were

located in the mined panel, LW250103, on the south side of the study panel. The burst-induced roadway damage included instantaneous floor heave, rib convergence and ground support failure. The burst damage length is measured as the length of a roadway that has experienced instant burst-induced damage after a coal burst occurrence, which cannot be further used without an extensive rehabilitation. The burst damage length induced by the 29 coal bursts varied from 20 m to nearly 200 m, and many of the damage zones overlapped with each other. It means that some areas experienced burst damage more than once, where high energy and high-stress concentration around the panel was not yet sufficiently released after one coal burst event.

According to the source radius estimation proposed by Ryder and Jager (2002), the expected source radii of coal bursts are between 4.72 m and 38.41 m, and the radii of potential induced failures can be more than 50 m, which is about twice the source radii (Kaiser et al., 1996b). The epicentral distances between coal burst damage zones and coal bursts ranged from 0 to 200 m. About 60% of the coal bursts (17 of 29) caused burst damage within 50 m of epicentres. These coal bursts commonly generated intensive ground motions and instant fractures to the adjacent roadway, which could be the source of the burst damage (Kaiser and Cai, 2013b). Over a third (37%) of the coal bursts (11 of 29) caused damage located more than 50 m away from the epicentres of coal bursts. It can be postulated that the dynamic loads induced by these coal bursts play an essential role in triggering burst damage if the coal or rock mass is critically stressed.

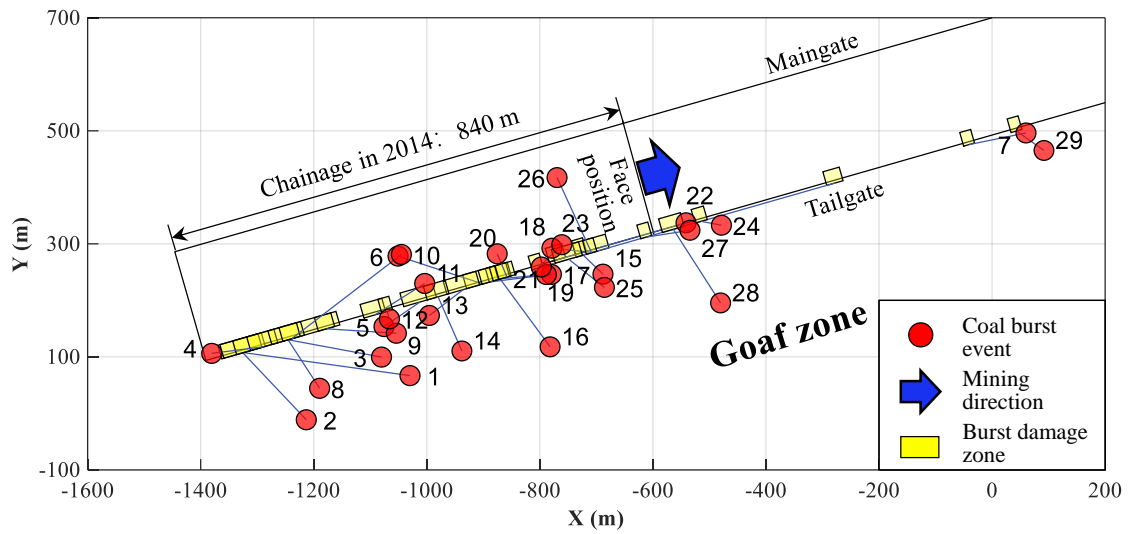


Figure 3-9 Spatial distribution of coal bursts and burst damage zones during the retreat of LW250105 in 2014. The blue line links the epicentres of the coal bursts and the corresponding burst damage zones.

According to Table 3-2, 45% of the coal burst damage (13 of 29 bursts) occurred within 50 m ahead of the longwall face, and 6 of them were ahead of the tailgate. It corresponds with the results shown in Figure 3-8, indicating that frequent seismic activities and intensive energy release were found near the longwall face. It also demonstrates that significant abutment stress caused by the longwall face retreat would be one of the main factors resulting in frequent coal burst hazards. Also, 24% of the coal burst damage zones were located 50~100 m ahead of the longwall face (7 of 29), and 31% were located over 100 m (9 of 29) in front of the face. Besides the side abutment stress induced by the goaf zone, the burst damage was possibly attributed to the undetected geological structures, which can cause further stress distribution in the coal and rock mass. Considering that high-level event counts still occurred more than 200 m away from the longwall face (see Figure 3-8), the local clustering of seismic activities is an essential clue to locate undetected geological structures and evaluate coal burst hazard potential.

As regular monitoring for LW250105 commenced from April 2014, coal bursts from April to December 2014 were used for analysis in the following chapters in this thesis.

Table 3-2 Characteristics of coal bursts in LW250105 during 2014

No.	Date	Seismic energy (MJ)	Local magnitude	Damage length in tailgate (m)	Distance from the coal burst to longwall face (m)
1	17 Mar	0.38	0.52	200	0
2	19 Mar	0.72	0.71	40	0
3	26 Mar	0.45	0.57	15	10
4	29 Mar	0.19	0.98	\	\
5	30 Mar	2.77	0.43	50	310
Below are the coal bursts used for analysis in this research					
6	8 Apr	28.6	1.78	60	400
7	13 Apr	0.18	0.30	20	1300
8	17 Apr	0.77	0.72	60	15
9	24 Apr	1.86	0.98	30	80
10	29 Apr	2.96	1.11	32	0
11	27 May	1.22	0.86	40	60
12	3 Jun	2.35	1.05	20	70
13	27 Jun	1.78	0.97	60	110
14	10 Jul	1.78	0.97	40	35
15	29 Jul	0.094	0.12	20	255
16	2 Aug	0.18	0.31	40	85
17	6 Sep	0.34	0.49	30	0
18	7 Sep	0.55	0.63	60	170
19	12 Sep	0.13	0.21	30	0
20	15 Sep	0.47	0.58	30	0
21	16 Sep	1.11	0.83	30	600
22	22 Sep	0.088	0.10	30	70
23	27 Sep	0.62	0.66	20	20
24	6 Oct	0.053	-0.05	22	292
25	11 Oct	1.86	0.98	50	20
26	25 Oct	0.057	-0.03	19	36
27	16 Nov	0.14	0.22	20	76
28	3 Dec	0.17	0.28	40	73
29	13 Dec	1.32	0.88	20	693

3.6 Summary

This chapter provides an overview of the case study site, LW250105 in Huating Coal Mine, Gansu Province, China. Complex geological and mining conditions contribute to high burst proneness in this site. Due to the high thickness of the coal seam, LW250105 adopted the longwall top coal caving method for coal extraction. The great mining height and caving height might cause elevated abutment stress from the longwall face and dynamic impacts from seismicity. Also, as only a 6 m-wide rib pillar was set between the tailgate and goaf, it is postulated that the coal to be extracted in LW250105 was under significant side abutment stress on the goaf side.

Two types of geophones were used for regular seismic monitoring in LW250105. Roadway geophones were placed in LW250105 roadways and moved along with the panel retreating, which aims to record the clear wave arrivals for locating purposes. Distant geophones were placed far away from the panel, mainly to record full waveforms for energy calculation. During LW250105 retreat in 2014, high-energy seismic events with seismic energy larger than 100 kJ were only a small fraction of the total seismicity (less than 5%), but they were responsible for the majority of coal bursts. The panel within 80 m ahead of the longwall face presented both peak event counts and seismic energy release, which indicates significant abutment stress in coal and rock mass and the high instability of roadway surroundings.

In LW250105, the majority of coal bursts resulted in roadway damage near the seismic source (<50 m). Such damage could be induced by the intensive ground motions and instant fractures to the adjacent roadway from the seismic source. The rest of the roadway damage was far away from the seismic source (>50 m). In this case, the burst damage zone was highly likely under critical stress already, and coal and rock failure was triggered by the dynamic loads from remote seismic sources. Nearly half of the burst damage occurred within 50 m ahead of the longwall face.

However, several burst damage zones were located hundreds of metres away from the longwall face, which may be attributed to the local high-stress concentration due to undetected geological structures. In Chapter 4, the relationship between coal burst and the ground motions characteristics in LW250105 will be investigated, and the triggering mechanism of burst damage will be discussed.

Chapter 4. Ground motion characteristics and their cumulative impacts on coal burst risks in underground mines

The content of this chapter has been submitted as a paper to the journal *Geomechanics and Geophysics for Geo-energy and Geo-resources*.

For the brevity and consistency of the thesis, repeated content has been removed and a concise introduction is presented.

4.1 Introduction

As illustrated in Section 2.3, ground motions and the induced dynamic impacts from seismic events are one of the main factors triggering rockburst hazards. The successive triggering from ground motions can cause cumulative damage and deformation in the stressed rock mass, where support elements present a lower safety factor and an elevated vulnerability to rockbursts (Kaiser and Cai, 2013a). It has been proven in hard rock mines that the historical ground motions are strongly related to coal and rock failures and excavation instability, but studies are rarely conducted in coal mines. Therefore, it is necessary to understand the ground motion characteristics of seismic events during mining to assess coal burst risks. Also, the stressed rock mass around the excavations may encounter unexpected high ground motions in the near-field zone of the seismic source, which can easily trigger dynamic failure in the excavation. However, due to the complicated calculation procedure and limitations in monitoring sensors, ground motions in near-field zones are still excluded from regular ground motion analysis (Kaiser and Cai, 2013a). Therefore, it is necessary to estimate the intensity of ground motions in near-field zones and investigate their relationship with dynamic failure.

In this chapter, ground motion characteristics of seismic events in both far-field and near-field zones were investigated, and their relationships with the impending coal burst hazards were further explored. Based on the seismic data in LW250105 for April to December 2014, the ground motion intensities of seismic events and coal bursts were compared with the published data in other mines. By estimating dynamic stresses induced by the ground motions, the triggering mechanism of coal burst damage is discussed. According to the cumulative damage that ground motions cause to the surroundings of a mine opening, a link was built between historical ground motions and coal burst damage. A new index called Number of High Ground Motions (NHGM) was also proposed to correlate with the actual coal burst damage.

4.2 Background

4.2.1 Ground motions in far-field zones

Theoretically, ground motions induced by seismic events in far-field zones are positively related to the seismic energy and decay as the distance increases from the seismic source (Mendecki, 1996; Shearer, 2009). To approximate ground motion intensity of a seismic event in the far-field zone, $ppvR$ (unit: m^2/s) is usually used. $ppvR$ is the peak particle velocity (ppv) of the recorded seismic wave from geophones multiplied by the hypocentral distance R , the distance between the event and individual geophones in an array (Kaiser and Maloney, 1997). Due to different source mechanisms, the wave radiation pattern of a seismic event in the far-field zone is complicated and directional, rather than in a simple spherical pattern, which causes different $ppvR$ readings among geophones (see Figure 4-1a). For seismic risk assessment and ground support design, it is necessary to consider the most critical seismic loadings. Hence, only the geophones that fully convey seismic energy in the maximum radiation direction are selected in this study (Kaiser and Cai, 2013a). Figure 4-1b shows an example of $ppvR$ results of different geophones from a seismic event. Geophone #3 has a higher $ppvR$ compared to others although its location is not the closest. This means, compared with other geophones, the seismic wave received by geophone #3 is most likely to be the peak or approximate to the peak of the radiation pattern. Thus the $ppvR$ recorded by geophone #3 is used to describe the ground motion intensity of this seismic event in the far-field zone. If an excavation is located in the far-field zone of a seismic event, the induced ground motion that the excavation undergoes, named $ppv_{far-field}$, can be estimated using the following equation:

$$ppv_{far-field} = \frac{ppv}{D} \quad (4-1)$$

where D is the distance from a seismic event to the nearest roadway, or 'event-roadway distance' for short (see Figure 4-1a).

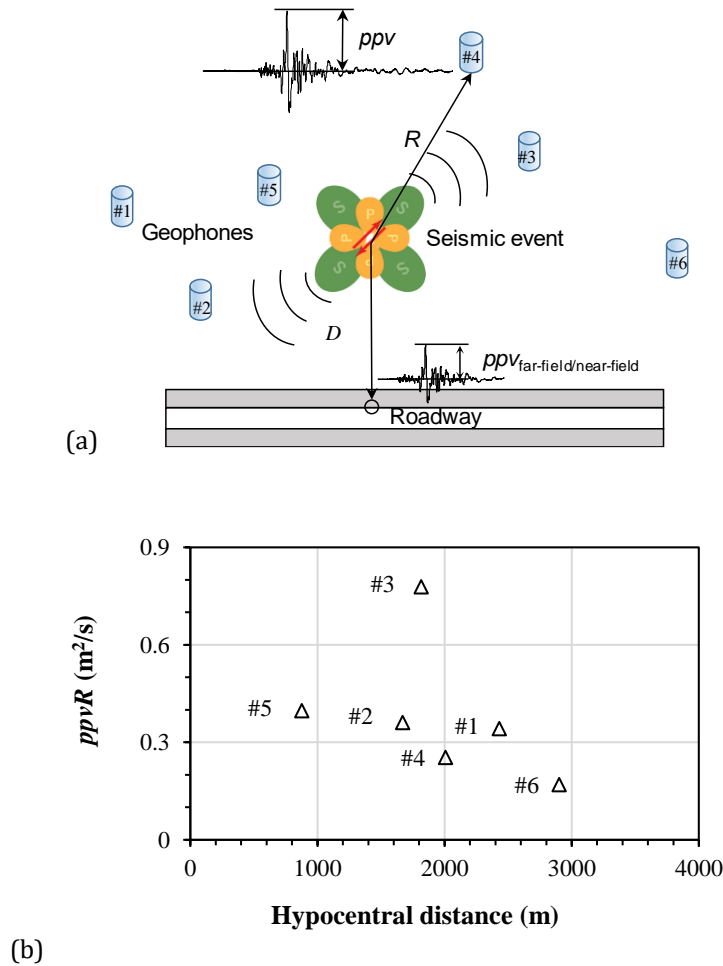


Figure 4-1 (a) Schematic diagram of source mechanism of a seismic event, ppv readings in different geophones and ground motion response in the roadway, (b) Example of $ppvR$ results of a seismic event from different geophones

4.2.2 Ground motions in near-field zones

As event-roadway distance is smaller than twice of the source radius, the excavation may experience intensive near-field ground motions. Due to the different radiation and attenuation characteristics, the intensity of a seismic event in the near-field zone cannot be simply described as $ppvR$. Although it is difficult to directly measure near-field ground motions, it is possible to have an estimation by using

analytical equations derived from synthetic seismograms and/or semi-empirical models. In this study, the method proposed by McGarr (1991) is adopted, which relates near-field ground motion to geophone recordings. Within the near-field zone of a seismic event, there are many asperities on the rupture plane (Van Aswegen and Butler, 1993). Each asperity failure can be regarded as a sub-event producing one single sine seismic wave (Boatwright, 1988). The patterns of seismic waves from geophone readings are thus the combination of sine waves from multiple asperity failures. The ground motion in each asperity failure, i.e. near-field ground motion, equals half of its slip velocity, which is the velocity of one side of the asperity with respect to the other side (Mendecki, 2016). The maximum slip velocity of the asperities can be calculated using hypocentral distance R and peak particle acceleration (ppa), which is the derivative of velocity waveforms from geophone readings. After considering the above factors, for an excavation located in the near-field zone of an event, the ground motion (referred to as $ppv_{near-field}$) can be calculated by Eq. (4-2) (McGarr, 1991):

$$ppv_{near-field} = 1.28(v_s/G)\rho R ppa \quad (4-2)$$

where v_s is shear wave velocity, ρ is rock density, and G is rock shear modulus. As the near-field ground motion is directly induced by the local rock failure, it can be used as an indicator to describe failure intensity.

4.3 Ground motion characteristics in LW250105

4.3.1 Ground motions in far-field zones

During the study period, nearly 10,000 seismic events in LW250105 were recognised as causing ground motions in far-field zones to the roadway. Figure 4-2 shows the relationship between $ppvR$ and seismic energies. The $ppvR$ of seismic events ranges from $3.1 \times 10^{-5} \text{ m}^2/\text{s}$ to $1.6 \text{ m}^2/\text{s}$. The highest $ppvR$ is from a seismic

event with energy magnitude of 87 kJ, located 45 m away from the roadway. According to the least-squares regression line in Figure 4-2, the relationship between average $ppvR$ and seismic energies is described as:

$$\log(ppvR) = 0.24(E_S) - 1.86 \quad (4-3)$$

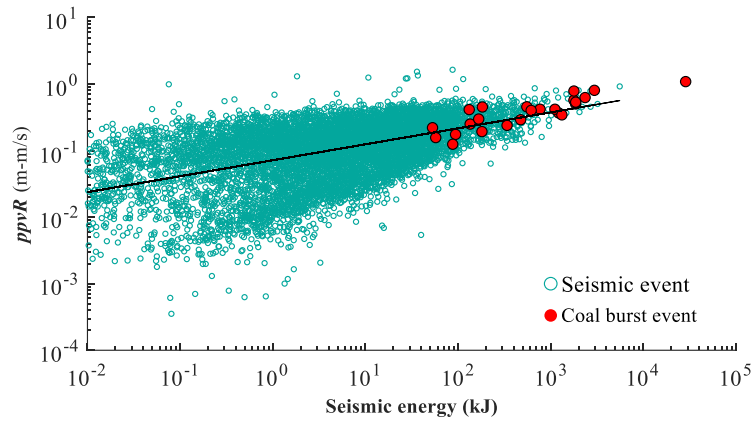


Figure 4-2 Relationship between seismic energy and $ppvR$ of seismic events and coal bursts in LW250105

Based on Eq. (4-3), a scaling law map was plotted in Figure 4-3a showing the average ground motion intensities in the far-field zone with varying seismic energies and hypocentral distances. For example, a seismic event with energies of 1 kJ is expected to induce ppv of 0.001 m/s at about 80 m away from the source. To compare the differences of ground motion intensities between coal mines and hard rock mines, the ground motion intensity recorded at hard rock mines, the gold mines in Klerksdorp Goldfield, South Africa (Glazer, 2018), is also presented in Figure 4-3b. Due to the higher magnitude of seismic energies, ground motions of more than 1 m/s can be experienced in hard rock mines. However, with the same energy level and hypocentral distance (shown as the zone with the red dashed line in Figure 4-3b), seismic events in coal mines can produce higher ground motions than those in hard rock mines. For example, to induce ground motions of 0.01 m/s from 10 metres away

from the source, a seismic event should have energies of 1 MJ in hard rock mines but only about 10 kJ in LW250105. It means that for the same ground motion level, the seismic energy required for events can be nearly 100 times smaller than that in hard rock mines.

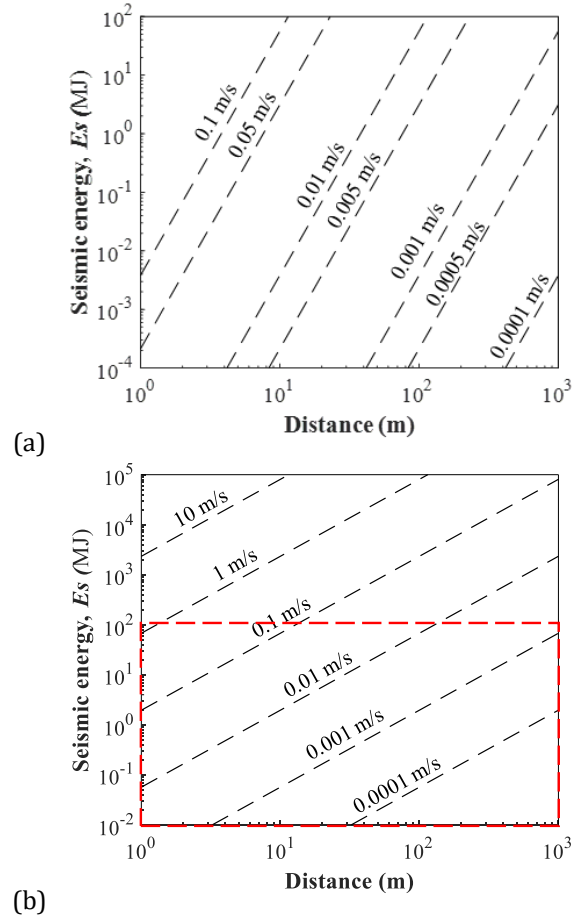


Figure 4-3 Average ground motion intensities in far-field zones of seismic events in (a) LW250105 and (b) gold mines in Klerksdorp Goldfield (Glazer, 2018). Red dashed line indicates the overlapping area of (a) and (b)

The $ppvR$ of studied coal bursts in LW250105 ranges from 0.12 m^2/s to 1.09 m^2/s , which only shows an average intensity compared to that of seismic events with similar energy level. Figure 4-4 displays $ppvR$ intensities between LW250105 coal bursts (marked with red), Upper Silesian Coal Basin coal bursts concluded by Dubinski and Mutke (1997) (marked with green) and rockbursts summarised by McGarr (1991) (marked with blue). Upper Silesian Coal Basin coal bursts cover a broad range of energy levels from 0.6 kJ to more than 34000 MJ, and the maximum

$ppvR$ is $14.13 \text{ m}^2/\text{s}$ (The 0.6 kJ coal burst is not displayed in Figure 4-4). Rockbursts have an overall higher energy level than coal bursts, and the maximum $ppvR$ can be up to $25.9 \text{ m}^2/\text{s}$. Compared to Upper Silesian Coal Basin coal bursts, the studied coal bursts in LW250105 have lower energy levels and $ppvR$ intensities. It demonstrates that the coal bursts in LW250105 were more easily triggered by seismic events than those in other mines in the literature.

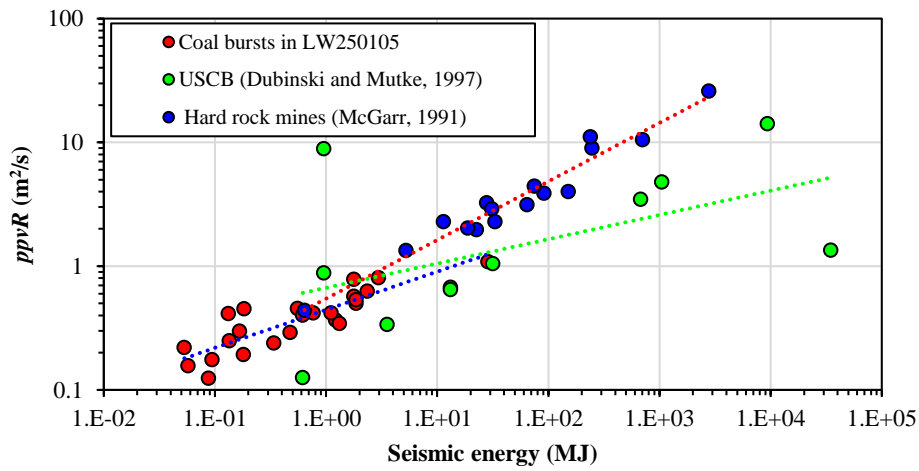


Figure 4-4 Relationship between $ppvR$ and seismic energy of LW250105 coal bursts (marked with red), coal bursts in Upper Silesian Coal Basin, referred as USCB (marked with green) and strong seismic events in hard rock mines (marked with blue)

Figure 4-5 shows the $ppv_{far-field}$ induced by seismic events and coal bursts in different ranges of event–roadway distances. The $ppv_{far-field}$ of the seismic events ranged from $2.16 \times 10^{-6} \text{ m/s}$ to 0.10 m/s , and the maximum $ppv_{far-field}$ was induced by a 28 kJ event which occurred 12.61 m away from the roadway. The $ppv_{far-field}$ of coal bursts ranged from $1.93 \times 10^{-3} \text{ m/s}$ to 0.017 m/s , with event–roadway distances from 24 m to 157 m . Although the average $ppv_{far-field}$ of coal bursts is higher than 80% of seismic events, the peak $ppv_{far-field}$ is still lower than that of nearly 600 seismic events, constituting more than 5% of the total. Most of the intensive $ppv_{far-field}$ of higher than 0.01 m/s were induced by the events located within 20 m of the roadway (see Figure 4-5a). Few intensive $ppv_{far-field}$

were observed from events located more than 40 m from the roadway (see Figure 4-5c, d, e, f).

The trend of ground motions in each event-roadway distance range can be presented by a power-law relationship:

$$\log(ppv) = a \log E_s + b \quad (4-4)$$

where a is the slope of the fitted trendline, indicating the difference of ground motions between events at different energy levels. b is the intercept/cut-off of the trendline showing an overall ground motion level. The black lines in Figure 4-5 are the best-fit power-law trendlines between $ppv_{far-field}$ and seismic energy. The result shows a lower a and a higher b in Figure 4-5a than in Figure 4-5b~f. It indicates that seismic events located less than 20 m from the roadway have generally higher $ppv_{far-field}$, which also covers a high energy magnitude range. For example, $ppv_{far-field}$ larger than 0.01 m/s can be induced by these seismic events with an energy level from only 0.02 kJ to 400 kJ. It implies that ground motions in the far-field zone induced by a seismic event closer to the roadway can be more intensive and less influenced by seismic energy. Figure 4-5b~f also shows that the $ppv_{far-field}$ induced by some coal bursts are even lower than many of the seismic events with the same energy levels. The results imply that most of the $ppv_{far-field}$ of seismic events and coal bursts are far below the risky ground motion criterion in the Upper Silesian Coal Basin, 0.2 m/s (Dou et al., 2016). Therefore, it can be postulated that the coal bursts in LW250105 were less likely initiated by $ppv_{far-field}$.

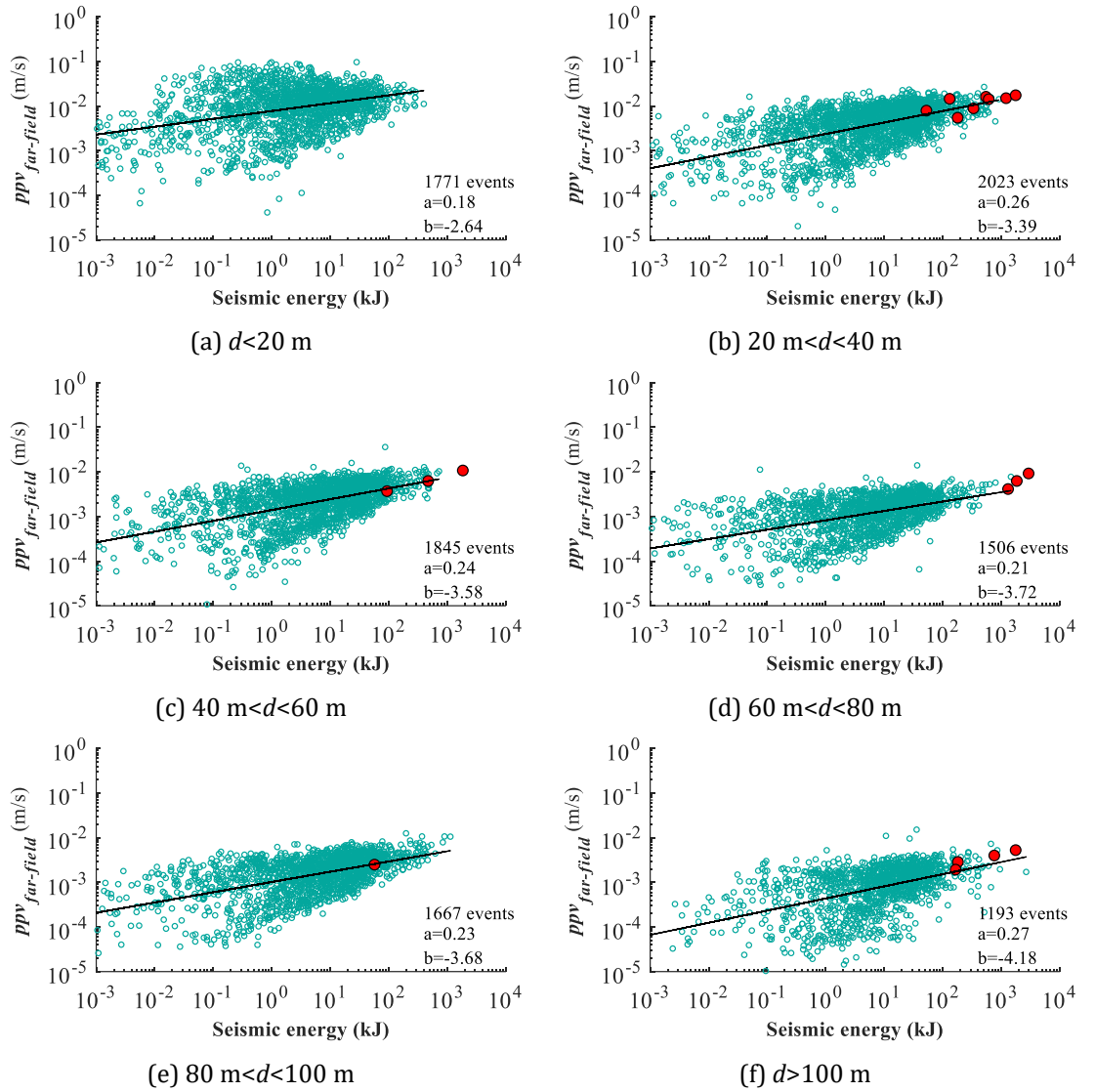


Figure 4-5 Far-field ground motions from seismic events (marked as blue dots) and coal bursts (marked as red dots) at different event-roadway distances (d)

4.3.2 Ground motions in near-field zones

From April to December 2014, 410 seismic events are determined to produce ground motions to roadways in the near-field zone, including 83 events to the maingate and 327 to the tailgate. Figure 4-6 is the $ppv_{near-field}$ results of these seismic events and the studied coal bursts. The seismic events produced $ppv_{near-field}$ from 7.64×10^{-4} m/s to 0.35 m/s, with a large seismic energy range from 0.25 kJ to 2350 kJ. The average $ppv_{near-field}$ is 0.076 m/s, which is nearly 20

times higher than average $ppv_{far-field}$, 5.0×10^{-3} m/s. For the purpose of hazard control and prevention, the study focuses more on the highest ground motion in extreme conditions at each energy level. Therefore, the upper bound limit of $ppv_{near-field}$ at 90% confidence was also plotted as a blue line in Figure 4-6, and this boundary was in the following equation:

$$\log(ppv_{near-field}) = -2.0 + 0.26 \log(E_S) \quad (90\% \text{ confidence}) \quad (4-5)$$

According to Eq. (4-5), a seismic event with energy of 1 kJ can potentially produce $ppv_{near-field}$ of 0.06 m/s, and a seismic event with energy of 1000 kJ is expected to have $ppv_{near-field}$ of up to 0.36 m/s.

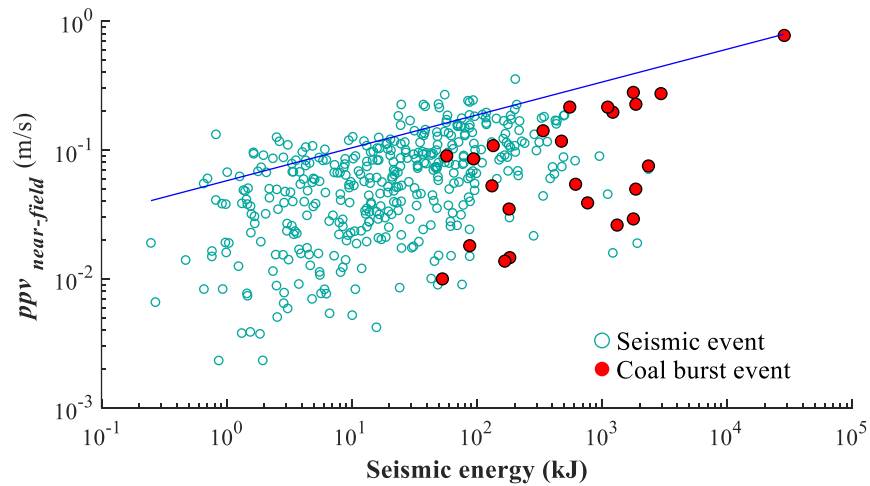


Figure 4-6 Relationship between seismic energy and near-field ground motions. The blue line denotes the upper bound limit of $ppv_{near-field}$ at 90% confidence.

Due to the higher energy magnitude and peak particle acceleration in the seismogram, coal bursts produced more intensive near-field ground motions than seismic events. $ppv_{near-field}$ of coal bursts ranged from 0.01 m/s to up to 0.77 m/s, with an average of 0.13 m/s. Similar results were presented by Cichowicz (2001) and McGarr et al. (1981), which suggest that the ground motions in the near-field zone can vary from 5.4×10^{-4} m/s to 0.46 m/s. The most intensive ground motion in

the near-field zone was induced by the coal burst on 8 April 2014, which released seismic energy of 28,600 kJ and caused damage 60 m long in the LW250105 tailgate. Compared with the hazardous seismic events at East Rand Proprietary Mines in South Africa (ERPM) (McGarr, 1991), the overall $ppv_{near-field}$ of the coal bursts is still lower than that of hazardous events in hard rock mines (see Figure 4-7).

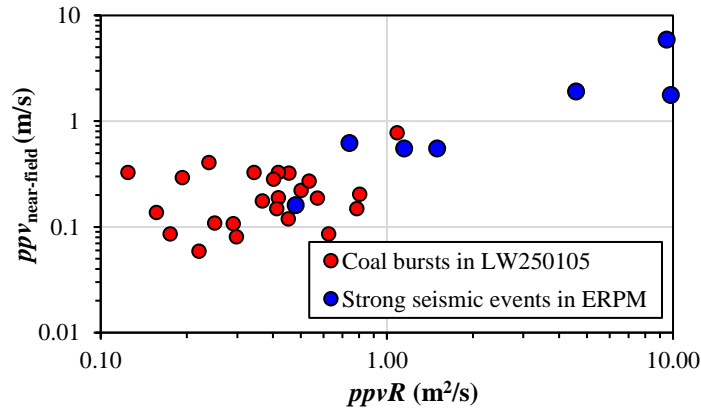


Figure 4-7 Ground motions in near-field zones of LW250105 coal bursts (red dots) and East Rand Proprietary Mines in South Africa, referred as ERPM (blue dots)

Figure 4-8 is the result of average intensities of ground motions in both far-field and near-field zones and the number of events in different ranges of event-roadway distances. From this figure, there is no general trend of the average ground motions in the near-field zone along with the increase of event-roadway distance. The peak average $ppv_{near-field}$ of 0.13 m/s was induced by the seismic events with event-roadway distances of 10 to 20 m, rather than the ones with event-roadway distances less than 10 m. It indicates that the zone with event-roadway distances of 10–20 m was under intensive static loads, since the failure of the highly loaded rock mass is more likely to accelerate vibrations and cause higher ground motions in the near-field zone (Mendecki, 2016). For all the ranges of event-roadway distances, the average $ppv_{far-field}$ is much lower than $ppv_{near-field}$, with values from 0.033 m/s when the event-roadway distance is less than 10 m to 0.002 m/s when the event-roadway distance is larger than 40 m.

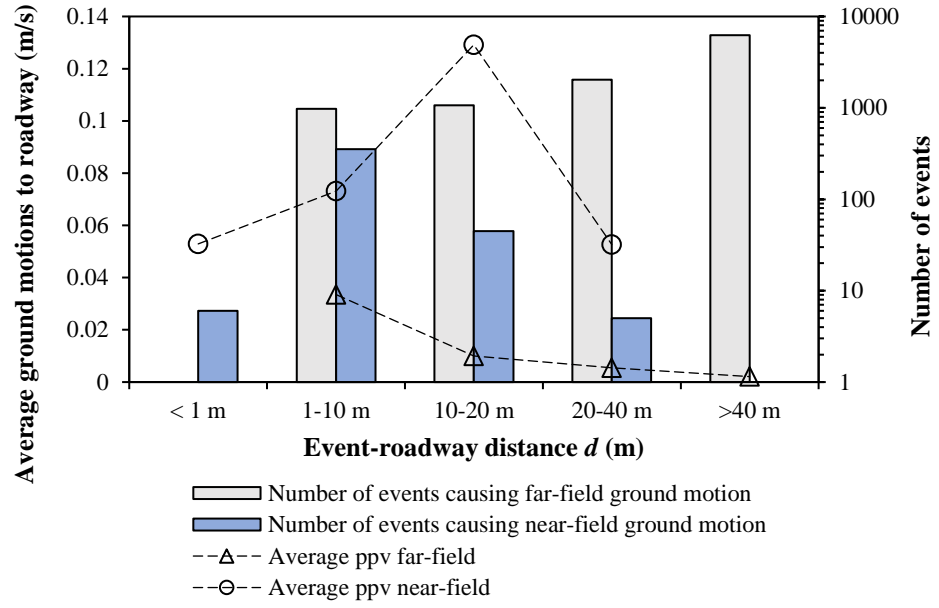


Figure 4-8 Average far-field and near-field ground motions and number of events at different event-roadway distances

4.3.3 Dynamic stresses

The equivalent dynamic stress induced by ground motions to the roadway can be estimated by Eq. (4-6) (Kaiser et al., 1996b):

$$\Delta\sigma^d = nv_s\rho \cdot ppv \quad (4-6)$$

In Eq. (4-6), ρ is the material density, v_s is the shear wave velocity, n is a constant ranging from -4 to 4, which is related to wave incidence angle. Since the most unfavourable conditions should be firstly considered for burst risk management in mines, n equal to 4 is adopted, which represents 45° incidence of the seismic wave relative to the maximum principal stress (Kaiser et al., 1996b).

Figure 4-9 shows the results of dynamic stresses induced by ground motions from seismic events and coal bursts, and the coal UCS (uniaxial compression strength) here is used as a reference. It shows that most of the low intensity dynamic

stresses are induced by ground motions in the far-field zone, and medium-high intensity dynamic stresses are dominated by ground motions in the near-field zone. Nearly 80% of the seismic events, with ground motions to roadways less than 0.009 m/s, induced dynamic stresses less than 0.1 MPa. Such a low transient stress increment in coal can be ignored if compared to the coal UCS of 13.7 MPa. Only the top 1% of ground motions produced dynamic stresses more than 10% of coal UCS, 1.37 MPa. Considering that the strength of the coal mass is commonly lower than UCS due to the natural jointing and fracturing, such intensity of dynamic stresses is likely to initiate the instability and failure of the highly loaded coal. The maximum dynamic stresses of ground motions that seismic events and coal bursts produced are 2.95 MPa and 8.48 MPa, respectively, which are 0.2 to 0.6 times the coal UCS. The results demonstrate that most ground motions cause negligible dynamic impacts on roadways, and coal bursts in this condition may only occur when the coal and rock mass is already in an unstable equilibrium. But for some significant ground motions, it is still possible to initiate dynamic failure in mine openings by a considerable dynamic stress transmission.

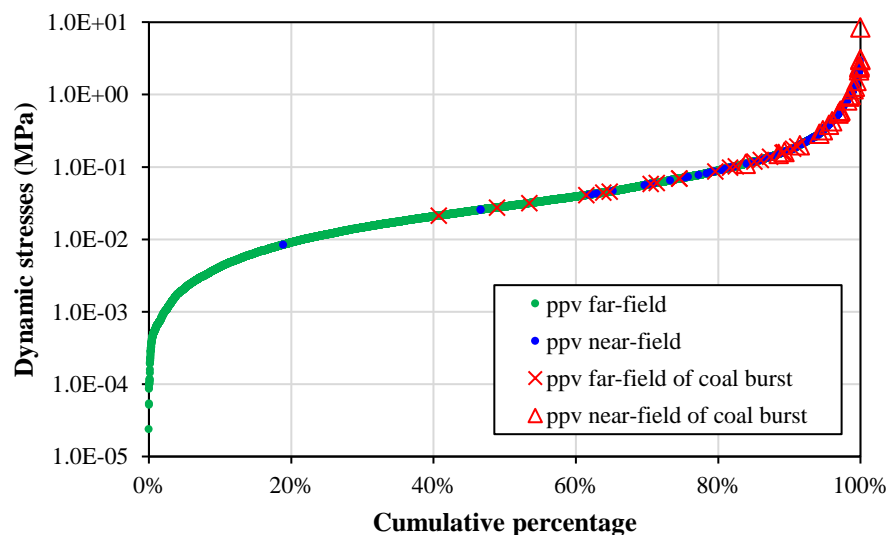


Figure 4-9 Ground motions and equivalent dynamic stresses that seismic events impart to LW250105 roadway

4.4 Correlation between historical ground motions and burst damage

4.4.1 Number of high ground motions

Ground motions can have a cumulative impact on increasing support vulnerability and burst damage risks in excavations. As indicated in Section 4.3.2, $ppv_{near-field}$ presented a much higher $ppv_{far-field}$ in the studied case. However, the current ground motion analysis for support design commonly excludes near-field sources (Cai and Kaiser, 2018). Ignoring near-field ground motions can underestimate the cumulative damage induced by seismic events, which may cause unexpected roadway instability to produce coal burst. Therefore, to comprehensively assess coal burst risks by using both far-field and near-field ground motions, an index called number of high ground motions ($NHGM$) was proposed to investigate the relationship between frequencies of intensive ground motions in history and actual burst damage in roadways.

$NHGM$ records the cumulative quantity of historical ground motions on roadways larger than a given threshold. The roadway length is discretised into several small sections (in 10 m intervals), and within each section i , $NHGM$ is calculated as:

$$NHGM_{(i)} = \sum_{j=1}^q y(j) \quad y(j) = \begin{cases} 1 & (ppv_j \geq ppv_k) \\ 0 & (ppv_j < ppv_k) \end{cases} \quad (4-7)$$

In Eq. (4-7), ppv_j is the ground motion resulting from the j^{th} seismic event, q is the last seismic event recorded. ppv_k is the threshold for $NHGM$ to filter out low intensity near-field and far-field ground motions. As seismicity and ground motions are highly site-dependent, ppv_k can vary among different underground mines. For

the study site, the ppv_k is set as 0.01 m/s, which is about the 85th percentile of all ground motions. With the face retreating, more sections in the roadway ahead of the working face will be located within the seismically active zone and their $NHGM$ start to increase. This study only considers the sections ahead of the working face that has undergone ground motions. Thus, the number of sections is updated daily and is different between studied coal burst cases.

4.4.2 Back analysis

Ground motions from all seismic events occurred for April to December 2014 at the LW250105 panel are used to calculate $NHGM$ at the tailgate. The $NHGM$ results for each coal burst case during the period are calculated using the seismic data from April 2014 to the day before the onset of the coal burst. Figure 4-10 is an example of $NHGM$ distribution on the tailgate ahead of the longwall face before the coal burst occurrence on 6 September 2014. In this figure, $NHGM$ distribution shows high values within 50 m away from the longwall face, and there is a downward trend with increasing distance to the longwall face. It means that the tailgate within 50 m away from the longwall face has a relatively higher instability than other zones due to the intensive ground motions experienced.

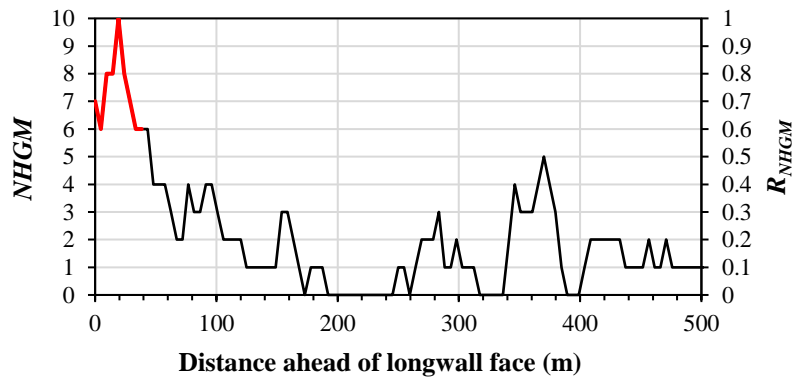


Figure 4-10 $NHGM$ distribution on the tailgate before coal burst occurred on 6 September 2014. Red line marks the burst damage position.

As $NHGM$ is a seismic related parameter, its value is related to the active degree of seismic events. The factors controlling the active degree of seismic events are not only stress conditions and geological structures in the coal and rock mass, but also mining rate, seismic monitoring quality at the time, and pre-destressing operations. As these factors vary along with the mining, a significant difference in the active degree of seismic events between different periods may occur, which usually results in a bias on seismic parameters. A typical scenario is that identical $NHGM$ values at different periods may not indicate the same coal burst risks. Therefore, a normalised $NHGM$, R_{NHGM} , is adopted to reduce the impacts of active degree of seismic events on the analysis results, which is the $NHGM$ within each section i divided by the maximum $NHGM$ in each result:

$$R_{NHGM(i)} = NHGM(i)/NHGM_{max} \quad (4-8)$$

where R_{NHGM} is the normalised $NHGM$, $NHGM_{max}$ is the maximum $NHGM$ of all sections in each result. In Figure 4-10, the burst damage zone was located in the highest $NHGM$ zone where R_{NHGM} is 1. It indicates that coal burst damage in this case had a strong correlation with high R_{NHGM} .

Figure 4-11 shows the R_{NHGM} results and the actual damage zones in LW250105 tailgate induced by 24 coal bursts. For better visualisation, the R_{NHGM} distributions are presented as colour bars. The bottom of the colour bar represents the latest longwall face position before a coal burst occurrence. Only 20 coal bursts have R_{NHGM} results for the analysis. The coal bursts on 8 April, 13 April, 16 September and 13 December caused the damage located outside the seismically active zone where no R_{NHGM} can be calculated. The R_{NHGM} results of damage zones in Figure 4-12 show that 65% (13 of 20) of the burst damage zones occurred in the zone with maximum R_{NHGM} larger than 0.6. Also, about 45% (9 of 20) of the

burst damage zones have maximum R_{NHGM} larger than 0.8. It indicates that the roadway zones with high R_{NHGM} values have higher burst damage risk.

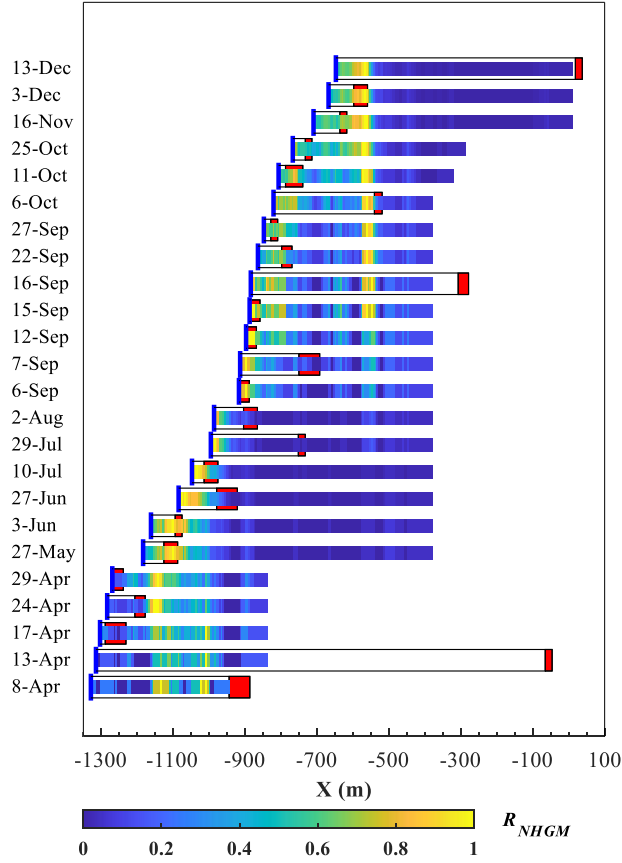


Figure 4-11 R_{NHGM} distributions in LW250105 tailgate before coal bursts occurred. The red zone is the coal burst damage zone. The blue line is the longwall face position.

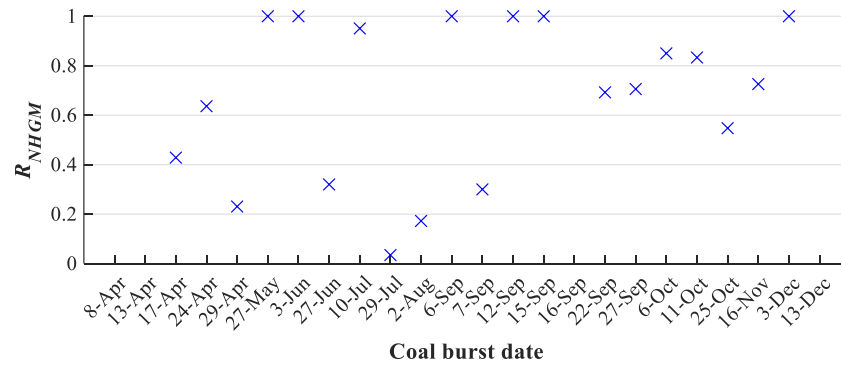


Figure 4-12 R_{NHGM} in burst damage zones in LW250105

The results in Figure 4-12 indicate that roadways with R_{NHGM} larger than 0.6 can have high burst risk due to a deep failure of surroundings and high vulnerability of the support system. However, there was still some burst damage before May with no R_{NHGM} result or with values lower than 0.6. One of the main reasons could be the poor seismic data integrity during the period. To evaluate the integrity of the seismic events before each studied coal burst, the maximum curvature method, which has been illustrated in Section 2.5.2, is used to calculate magnitude of completeness (m_c), and the results are shown in Figure 4-13. It implies that a relatively high m_c with values up to 0.15 was present in April 2014. It indicates that the seismic events with magnitude lower than 0.15, equivalent to about 105 kJ, were only partially detected during the period. According to the ground motion results in Section 4.3, seismic events with such intensities can generate $ppv_{far-field}$ of up to 0.014 m/s and $ppv_{near-field}$ of 0.085 m/s. Therefore, the low detection probability of these events can lead to a bias in R_{NHGM} results. From June, m_c decreased and fluctuated around -0.15, showing better integrity of seismic data, which contributes to R_{NHGM} results with less bias.

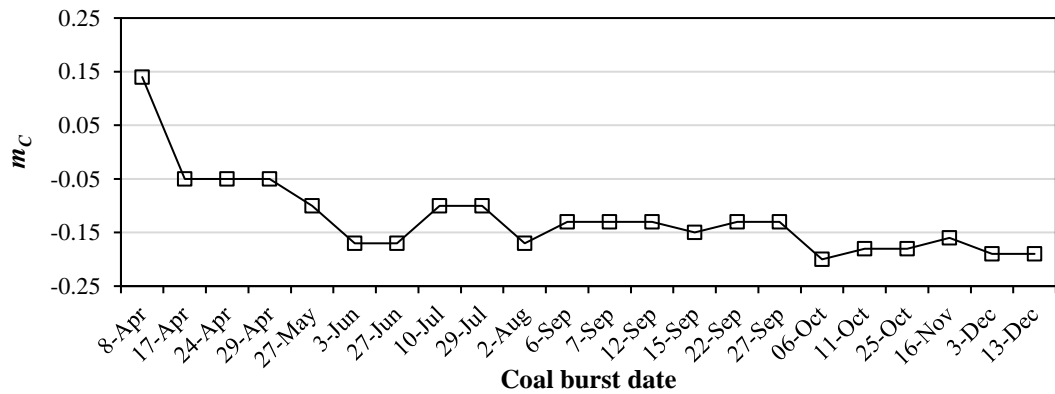


Figure 4-13 Magnitude of completeness before the occurrence of coal bursts in LW250105

4.5 Summary

In this chapter, a comprehensive ground motion analysis was implemented to explore dynamic impacts from seismic events on roadways and their relations with coal burst damage. The ground motions that roadways have undergone in both near-field and far-field zones were quantified. The ground motion-induced cumulative damage in roadway surroundings was also illustrated by the proposed index (*NHGM*).

The results indicated that $ppv_{near-field}$ has an overall much higher intensity than $ppv_{far-field}$. Compared with the rockbursts recorded in the literature, both the $ppv_{far-field}$ and $ppv_{near-field}$ of the coal bursts had much lower intensities. However, for seismic events at the same energy level, ground motion intensities in coal mines can be much higher than those in hard rock mines. In most cases, ground motions only generate negligible dynamic impacts on roadways, and coal bursts may be triggered when the coal and rock mass is already critically stressed. However, some significant ground motions may contribute to producing considerable stress increment and initiating dynamic failure.

The *NHGM* results demonstrated that coal bursts had a higher possibility of occurring in higher R_{NHGM} zones, i.e. the zone that has experienced more cumulative damage from past intensive ground motions. A low detection probability of the seismic monitoring system may lead to the failure to apply *NHGM* to assess coal burst risks. This study can contribute to providing a powerful tool for coal burst forecasting and roadway instability assessment in ground motion terms.

Chapter 5. Location error based seismic cluster analysis and its application to coal burst assessment

The content of this chapter has been published as a paper in the journal *International Journal of Rock Mechanics and Mining Sciences*.

<https://doi.org/10.1016/j.ijrmms.2021.104784>

For the brevity and consistency of the thesis, repeated content has been removed and a concise introduction is presented.

5.1 Introduction

In underground coal mines, seismic clustering analysis is a powerful tool to assess coal burst risks. As a seismic cluster represents the characteristics of the spatial distribution of seismic events, accurately locating seismic events is a prerequisite to successfully detect clustering behaviour. However, the location results of seismic events can be error prone because of the flatness of the geophone array, complex geological structures and intense extraction in underground coal mines (Leśniak and Pszczoła, 2008). Based on previous research, the location error of horizontal coordinates ranges from 4 to 50 m, while it can be up to 100 m for vertical coordinates (Gibowicz and Kijko, 1994; Kijko and Sciocatti, 1995; Stec, 2007; Leśniak and Pszczoła, 2008; Gong et al., 2010b). Such location errors are non-negligible compared to the size of mining excavations, which should be considered in seismic clustering analysis. How to assess the location errors during longwall mining and eliminate their impacts on seismic clustering analyses has become an urgent issue that needs to be addressed.

Therefore, this chapter proposes an enhanced seismic clustering method to reduce the influence of location errors and improve the accuracy of seismic cluster analysis in coal burst hazard assessment. To test the method, nine-month seismic data and the coal burst damage records for April to December 2014 in LW250105 are used. The location errors in the area of interest are assessed using the emulation testing method. The location error characteristics of the seismic monitoring system in different time periods are separately discussed. Based on the fracture sizes and the horizontal locations of seismic events, the seismic clustering criterion considering location errors is established. An index, named Number of Possible Clustered Events (*NPCE*), is introduced to investigate the seismic clustering distribution and evolution along with mining. The proposed method and the index

are then back analysed against the monitored coal burst damage zones recorded in the case study mine.

5.2 Location error assessment

5.2.1 Location error emulation test

The classic least-squares method was used to locate the events (Geiger, 1912). In a homogeneous-isotropic velocity model with a constant velocity, the arrival times of a seismic event recorded from n geophones are t_1, \dots, t_n . Find the occurrence time t_0 and the location (x_0, y_0, z_0) at any spatial point in the Cartesian coordinate to make the sum of squared time residuals as the minimum:

$$\Phi(t_0, x_0, y_0, z_0) = \sum_{i=1}^n r_i^2 \quad (5-1)$$

In this equation, r_i equals

$$r_i = t_i - t_0 - T_i(x_0, y_0, z_0) \quad (5-2)$$

$$T_i(x_0, y_0, z_0) = \frac{\sqrt{(x_0 - x_i)^2 + (y_0 - y_i)^2 + (z_0 - z_i)^2}}{v_p} \quad (5-3)$$

where $T_i(x_0, y_0, z_0)$ is the travel time of the seismic wave, (x_i, y_i, z_i) is the location of the i^{th} geophone, and v_p is the average P-wave velocity. The seismic event may be mis-located by this locating process due to errors from two aspects: random location scatters and systematic bias (Gibowicz and Kijko, 1994; Gibowicz and Lasocki, 2001). Random location scatter δ_p is the error produced in picking the arrival times of seismic waves. As the arrival times are manually picked in field monitoring in most cases, δ_p depends on the experience of individual seismologists and cannot be eliminated. Systematic bias is the wave velocity error δ_v , which is site-dependent

due to the limited knowledge of the velocity model of rock mass structure between events and geophones. If these two errors are considered, the time residual r'_i and travel time $T'_i(x_0, y_0, z_0)$ are:

$$r'_i = t_i \pm \delta_{ip} - t_0 - T'_i(x_0, y_0, z_0) \quad (5-4)$$

$$T'_i(x_0, y_0, z_0) = \frac{\sqrt{(x_0 - x_i)^2 + (y_0 - y_i)^2 + (z_0 - z_i)^2}}{v_p + \delta_{iv}} \quad (5-5)$$

where δ_{ip} and δ_{iv} are the arrival-time picking error and the wave velocity error in the i^{th} geophone, respectively. These two errors will cause a locating result to drift away from the original position of the seismic event.

According to the seismic locating method, the location accuracy of a seismic monitoring system mainly depends on the layout of the geophones, average P-wave velocity v_p , errors δ_p and δ_v . To assess the location capability of a seismic monitoring system, Gong et al. (2010a) proposed an “emulation testing” method to forward analyse the location error considering δ_p and δ_v before mining. The principle of this method is to firstly repeat locating a known point with random errors of δ_p and δ_v . Then a location error can be evaluated by statistically analysing the locating results. In this study, only horizontal locations of seismic events are considered. Therefore, the emulation testing process includes the following steps:

(i) assume a seismic event occurs at the test point (x_0, y_0) with an occurrence time t_0 , thus both theoretical arrival time t_i and travel time $T_i(x_0, y_0)$ can be derived by Eq. (5-2) and Eq. (5-3);

(ii) assume the random errors δ_p and δ_v follow the Gaussian distribution, the errored arrival time $t_i \pm \delta_{ip}$ and errored wave velocity $v_p \pm \delta_{iv}$ are used to relocate this event based on Eq. (5-1), Eq. (5-4) and Eq. (5-5); and

(iii) conduct large numbers of emulation tests, by repeating relocating the event in step (ii), to derive a scatter plot showing the potential event locations with errors.

Based on the emulation test results, the location error, δ_L , can be determined by:

$$\delta_L = \frac{\sum_{k=1}^{N_m} \sqrt{(x_{0'k} - x_0)^2 + (y_{0'k} - y_0)^2}}{N_m} \quad (5-6)$$

where $x_{0'k}$, $y_{0'k}$ are the location of the k^{th} emulation test, N_m is the number of emulation tests. The location error on the test point can also be represented by an error ellipse. Error ellipse is the standard deviation ellipse with long axis a and short axis b , which are equal to the standard deviations of the emulation testing results along with two axis directions, respectively. Figure 5-1a is an example of emulation tests for a given point with δ_L of 20.05 m. The error ellipse is shown in orange, with $a=29$ m and $b=15$ m. As the error ellipse represents the area of most of the emulation testing results, its size determines the locating accuracy of the point. A larger error ellipse means a wider range of location results and lower location accuracy. Inversely, a smaller error ellipse indicates a higher location accuracy as indicated by more concentrated emulation testing results. Within the error ellipse, the emulation testing results are not evenly distributed but follow a normal distribution. Figure 5-1b is the probability density of the Gaussian distribution based on the emulation testing results in Figure 5-1a. It indicates that the target point location, represented by the emulation testing results, is more likely to be near the centre of the error ellipse than the boundary. Figure 5-1b can be used to detect the clustering possibilities between events after their relocations, which is discussed in more detail in Section 5.3.

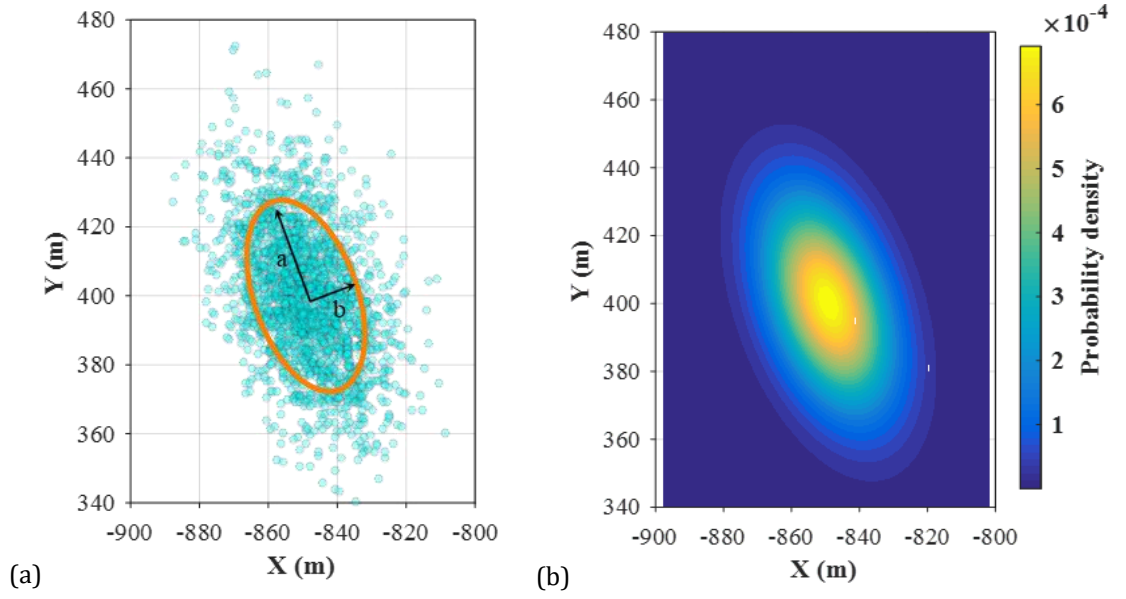


Figure 5-1 (a) Example of 2000 emulation testing results of a point at X=-850 m and Y=400 m. δ_L is 20.05 m, and a and b of the error ellipse are 29 m and 15 m, respectively. (b) Probability density of Gaussian distribution based on emulation test results of (a).

Based on the emulation testing method, the location error assessment in the monitored mining area can be investigated. It is implemented by discretising the mining area into grids and assessing location errors at all grid points. The location error is fully dependent on the monitoring system settings such as wave velocity and geophone locations. Therefore, the assessment should be recalibrated each time after the monitoring system is modified during mining.

5.2.2 Location error analysis

Table 5-1 shows the main input parameters for calculating location error during LW250105 retreat. The average P-wave velocity is determined by the controlled blasting tests at the mine for calibration purposes. It is used as a wave velocity input for locating seismic events. According to the seismic data statistics for this mine, about 80% of the P-wave arrival times have δ_v within ± 0.006 s. Thus, 0.006 s was set as the standard deviation of δ_v . There is no proven method to accurately estimate δ_p . Due to the local stress conditions, geology and velocity fields in

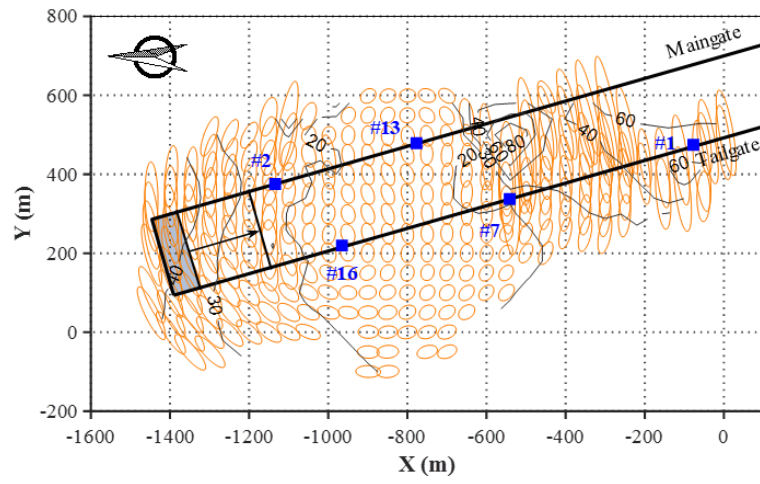
underground mines are highly complex and site-dependent. Many scholars have used the velocity tomography imaging method to investigate velocity distribution in the field. Some mines experience small variations of the P-wave velocity of 200 m/s to 600 m/s (Mason, 1981; Dubiński et al., 2013), while others experience high velocity differences of more than 2 km/s (Cao et al., 2016; Wang et al., 2017). Therefore, further studies to estimate δ_p are still needed. In this study, the standard deviation of δ_p was determined as 100 m/s, which ensures 68% of the emulation tests with δ_p lower than ± 100 m/s (one standard deviation of the mean), and 95% with δ_p lower than ± 200 m/s (two standard deviations of the mean). To ensure the precision of operation in a reasonable computing time, 2000 emulation tests on each grid (a 50 m square) have been adopted. The number of geophones used for emulation testing on each grid point varies from four to seven.

Table 5-1 Input parameters for assessing seismic location error in LW250105

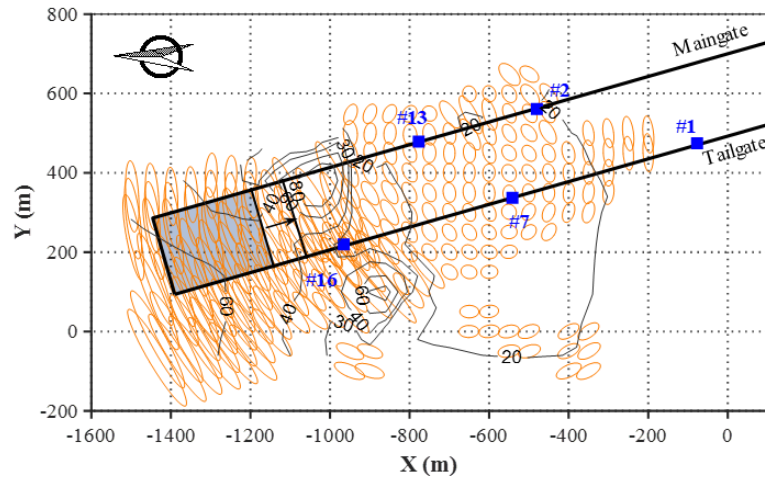
Grid size	Average P-wave velocity	Standard deviation of δ_v	Standard deviation of δ_p	Number of emulation tests
50 × 50 m	3600 m/s	100 m/s	0.006 s	2000

In the back analysis, the location error assessment was only conducted in the mining area where seismicity had occurred. Due to the longwall face approaching, the roadway geophones were regularly moved along with the face to capture mining-induced seismic events in relatively close proximity. As indicated in Figure 3-4, there were four modifications of geophone locations in LW250105 during the study period. As a result, location error assessments were conducted in the panel for four different time periods, and the results are shown in Figure 5-2. In the figure, the arrow indicates the longwall chainage and the location during the time period, the contours are the δ_L distribution calculated by Eq. (5-6), the blue square is the geophone, and the shadow zone behind the longwall face is the goaf zone. The results indicate that large differences of location errors are observed in different zones of the panel. In Figure 5-2a, the zone located between geophones

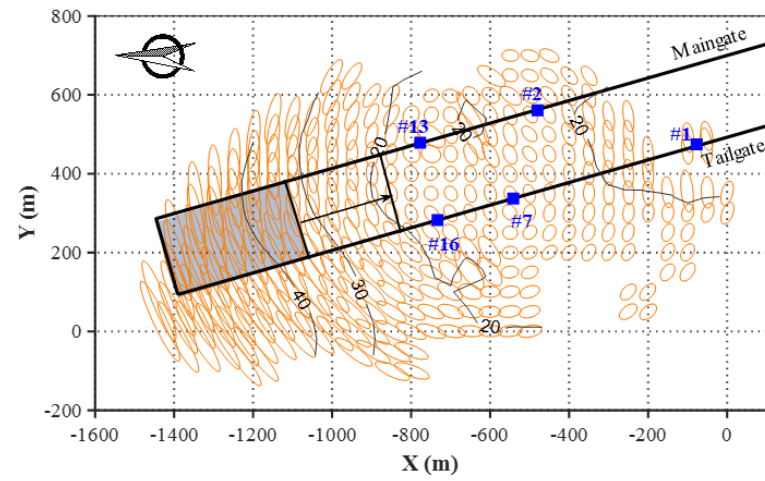
#13 and #16 indicates a relatively high locating accuracy, with δ_L smaller than 20 m. Due to the lack of geophone coverage, the longwall chainage and the goaf zone from 5 April to 4 June 2014 have higher location errors, with δ_L from 30 m to more than 40 m. The zone between geophones #1 and #7 also has large location errors with δ_L more than 80 m, where the location results of seismic events could be highly suspicious. In Figure 5-2b, as geophone #2 was relocated on 5 June 2014, higher location errors occur in both the longwall chainage and goaf zone, with δ_L from 30 m to 80 m. A low location error zone appears to be located between geophones #2 and #13, with δ_L about 20 m. In Figure 5-2c, after relocating geophone #16 on 1 July 2014, geophones were more than 300 m away from the longwall face at the beginning of the time period, but the location errors in the mining area are lower than those in Figure 5-2b. It implies that the geophone layout could be as important as the distance to geophones for location accuracy. In Figure 5-2d, the new geophone layout from 30 September to 11 December 2014 increased the locating accuracy in the mining area, with δ_L of about 20 m. High location errors are detected in the goaf and the zone around geophones #1 and #13, with δ_L about 40 m. Figure 5-2d indicates that the zone with the highest location accuracy is 50 m to 300 m ahead of the longwall face, with δ_L around 20 m. Due to the insufficient geophone coverage, the goaf zone and the longwall chainage progressed over individual periods commonly have higher location errors.



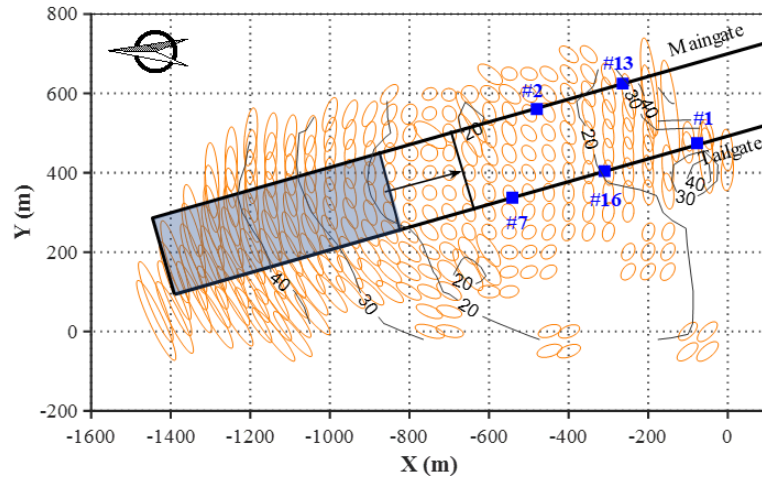
(a) Period I: 5 April to 4 June 2014



(b) Period II: 5 June to 30 June 2014



(c) Period III: 1 July to 29 September 2014



(d) Period IV: 30 September to 11 December 2014

Figure 5-2 Roadway geophones layout, δ_L contours (unit: m) and error ellipses distribution in four time periods during LW250105 recovery in 2014. The blue square is a roadway geophone, the arrow is the mining direction and the longwall chainage during the time period, and the shadow area is the goaf behind the panel face.

The error ellipses in Figure 5-2 also show that location errors have a strong anisotropic pattern. For the north and south parts of the panel, the error ellipses present high a/b ratios with values commonly higher than 4, and the a axis is in the east/west direction. It means that the detected seismic events in these zones have higher location errors on the east/west side but lower errors on the north/south side. In contrast, the error ellipses in the high location accuracy zone in front of the longwall face commonly present a/b ratios of lower than 2. It means that seismic events have similar location errors in a and b axis directions. Since event locating is critical in seismic clustering analysis, these location error characteristics must be considered to constrain the clustering result and improve its accuracy.

5.3 Seismic clustering based on source radius and location error corrections

5.3.1 Location error correction and clustering possibility

Since a seismic event can possibly occur at another place within the local error ellipse rather than its original monitored location, it has the potential to be clustered with adjacent events. Therefore, for risk assessment purposes, it is necessary to consider the location error of seismic events and assess the clustering possibility. As the locating probability of a seismic event in its error ellipse follows the Gaussian distribution, the probability of two seismic events getting clustered is:

$$\eta_{c(ij)} = \frac{p_i}{p_{peak}^i} \cdot \frac{p_j}{p_{peak}^j} \quad (5-7)$$

where $\eta_{c(ij)}$ is the joint cluster probability of event i and event j , ranging from 0 to 1. $p_i(p_j)$ is the probability density of the zone where the event i (event j) is located. $p_{peak}^i(p_{peak}^j)$ is the mode of the probability function, which presents the highest probability of the event location within the error ellipse. Higher η_c indicates a higher cluster possibility between two seismic events. According to Section 2.3.1, for the area with the distance between r_0 and $2r_0$ to the source, the occurrence of a seismic event could still cause a stress change that may affect adjacent fractures. Hence, it is determined that the two seismic events can be clustered if their distance, d , is lower than twice the sum of their source radii $r_{0(1)}$ and $r_{0(2)}$:

$$d \leq 2(r_{0(1)} + r_{0(2)}) \quad (5-8)$$

where $2(r_{0(1)} + r_{0(2)})$ is the critical distance of two events that can be clustered, named d_{max} .

By considering both locating error and seismic source radius, for a pair of seismic events, three possible clustering cases have been identified in Figure 5-3. In case I, the distance between two events at the original locations d is less than d_{max} , thus both events have peak probability densities with $\eta c = 1$ (Figure 5-3a). In case II, d is larger than d_{max} , and two events cannot be clustered at their original locations. However, within their error ellipses, these two events can still be clustered by shifting their locations to make their new distance d' equal to d_{max} (Figure 5-3b). The relocating process of seismic events is an optimisation problem, and the principle is to find the new locations of the two seismic events that can maximise the joint cluster probability ηc . In this case, ηc is between 0 and 1. In case III, two seismic events are too far away from each other to be clustered even after relocating. In this condition, both d and d' are larger than d_{max} , and $\eta c = 0$ (Figure 5-3c).

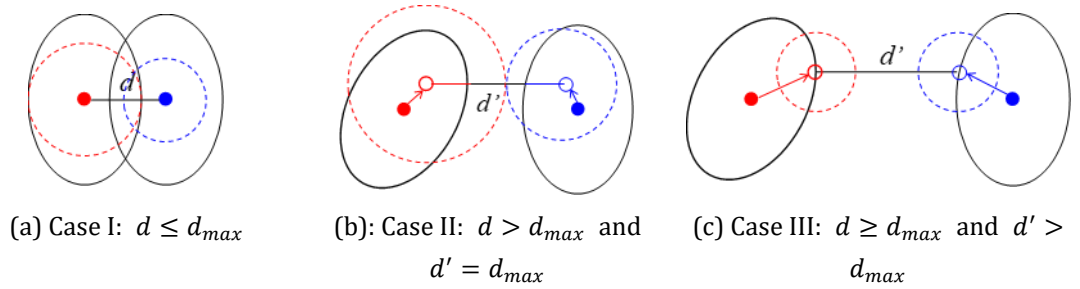


Figure 5-3 Three cases for a pair of seismic events to be considered in clustering probability analysis. Two seismic events at their original locations are represented by filled dots, and their distance is d . The dashed circle shows the zone with two times the source radius ($2r_0$) of each seismic event. After relocating, the new locations of the seismic events are represented by unfilled dots, and their distance becomes d' . d_{max} is the critical distance of two events that can be clustered.

5.3.2 Number of possible clustered events (NPCE)

Based on the concept of clustering possibility proposed above, for a specific

event, the possible number of events to be clustered with it during a given time period can be calculated, which is named the Number of Possible Clustered Events (*NPCE*). As the clustering possibility method considers both location errors and the energy magnitudes (for source size calculation), *NPCE* results can properly represent both seismic intensities and densities in the mining area. *NPCE* is expressed as:

$$NPCE_i = \sum_{j=1}^n y(j) \quad (5-9)$$

$$y(j) = \begin{cases} 1 & (\eta c_{ij} \geq \eta c_{threshold}) \\ 0 & (\eta c_{ij} < \eta c_{threshold}) \end{cases} \quad (5-10)$$

where n is the number of events in the time period, which is assumed as one week in this study, ηc_{ij} is the clustering probability between event i and event j , $\eta c_{threshold}$ is the ηc threshold ranging from 0 to 1 to determine whether clustering exists between a pair of events.

Figure 5-4 gives an example of how the *NPCE* of an event is calculated. In Figure 5-4, there are 5 seismic events (marked in blue) around the target event #0 (marked in red). Events #3 and #4 are far away from event #0, so their ηc are 0. Event #2 can be clustered with event #0 at the original location with ηc of 1. Events #1 and #5 have the possibility of clustering with event #0 after relocation, with ηc of 0.75 and 0.2, respectively. Since the $\eta c_{threshold}$ in the example is set as 0.5, event #5 is determined as non-clustered with event #0. As a result, event #0 is clustered with events #1 and #2, thus its *NPCE* is 2.

Cluster possibility with event 0 ($\eta c_{threshold}=0.5$)

Event No.	ηc	Condition
1	0.75	Clustered
2	1	Clustered
3	0	Uncolstered
4	0	Uncolstered
5	0.2	Uncolstered
NPCE of event 0:		2

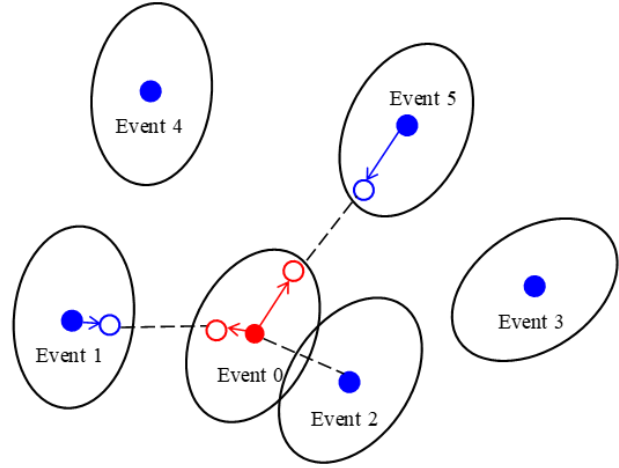


Figure 5-4 An example of the *NPCE* calculation for seismic event #0 (marked in red). Blue dots are the seismic events adjacent to event #0. The ellipse is the location error ellipse of the seismic event, a filled dot is the original event location, an unfilled dot is the possible location of the event within the error ellipse.

$\eta c_{threshold}$ is mainly used for controlling the clustering quality between events. For lower $\eta c_{threshold}$, more seismic events tend to be clustered with lower cluster probability, thus *NPCE* results are commonly higher. On the contrary, a higher $\eta c_{threshold}$ can filter out more seismic events that can be potentially clustered, thus *NPCE* results become lower. Figure 5-5 shows an example of *NPCE* results in LW250105 with different $\eta c_{threshold}$. It shows that the maximum *NPCE* value decreases from 48 to 20 when $\eta c_{threshold}$ increases from 0.3 to 0.9. The area of high *NPCE* zones also narrows along with the increase of $\eta c_{threshold}$. At the same time, more seismic events appear to be isolated from other events, with *NPCE* of 0. Since there is no reference for $\eta c_{threshold}$ determination, $\eta c_{threshold}$ of 0.5 was set in the *NPCE* analysis.

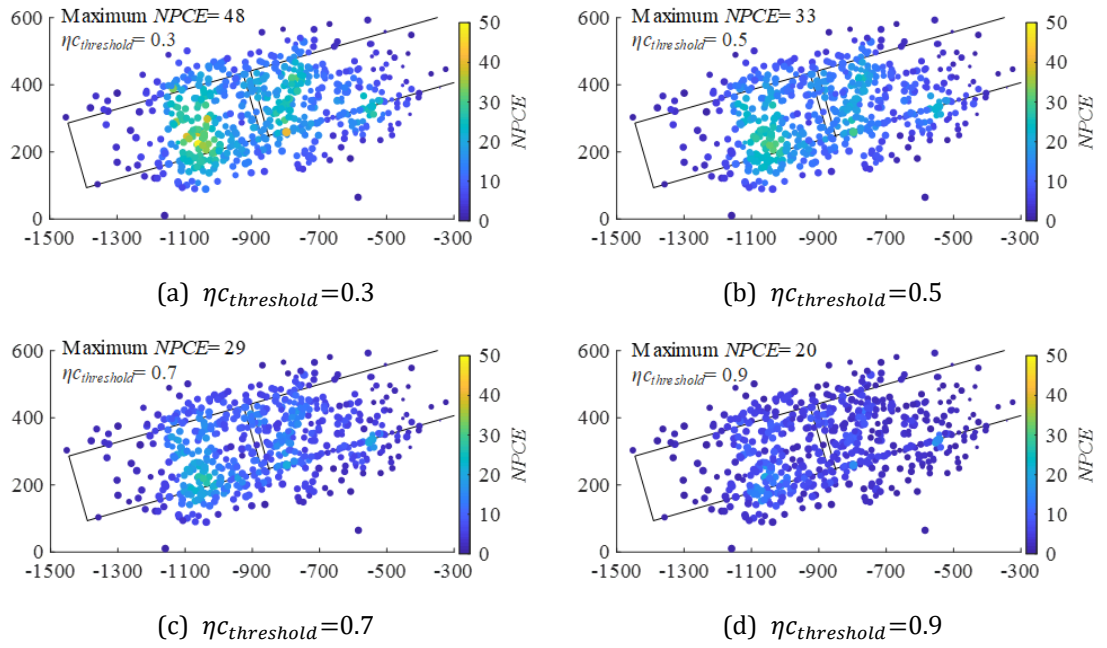
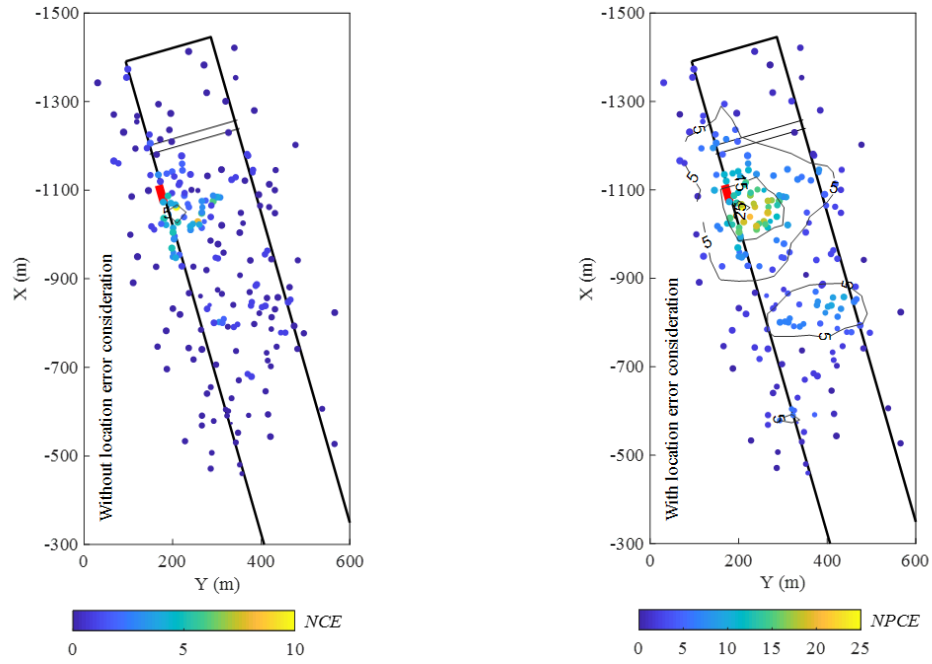


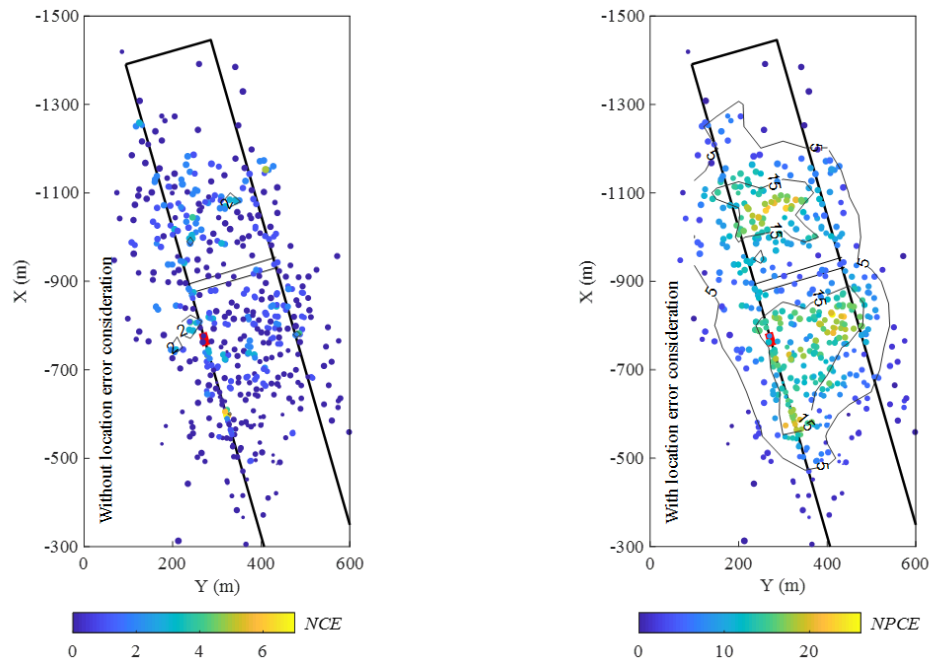
Figure 5-5 An example of *NPCE* results with different $\eta_{C_{threshold}}$

Figure 5-6 shows three typical examples of seismic clustering results without considering location errors (on the left) and *NPCE* results (on the right). The red zone on the tailgate represents the coal burst damage which occurred in the following week. For the clustering results without considering location errors, the number of clustered events is named *NCE* for short. The *NCE* results indicate a significantly lower number of clustered events, with the maximum *NCE* ranging from only 2 to 10. Also, most of the seismic events have no event to cluster with, which indicates that they are isolated from adjacent events. This means high stress concentrations or geological structures, evidenced by seismic clusters, may be rarely detected. In Figure 5-6a and Figure 5-6b, the *NCE* results (on the left) are unable to cover coal burst damage areas. In Figure 5-6c, only one seismic event with the highest *NCE* of 2 is located in the burst damage zone (on the left). The *NCE*-based coal burst risk assessment method is highly unstable due to its significantly low number of clustered events and insensitivity to assess various risk levels. In contrast, *NPCE* results provide a significantly larger range of seismic clustering areas and more robust assessment for different levels of coal burst risk. The *NPCE* values on

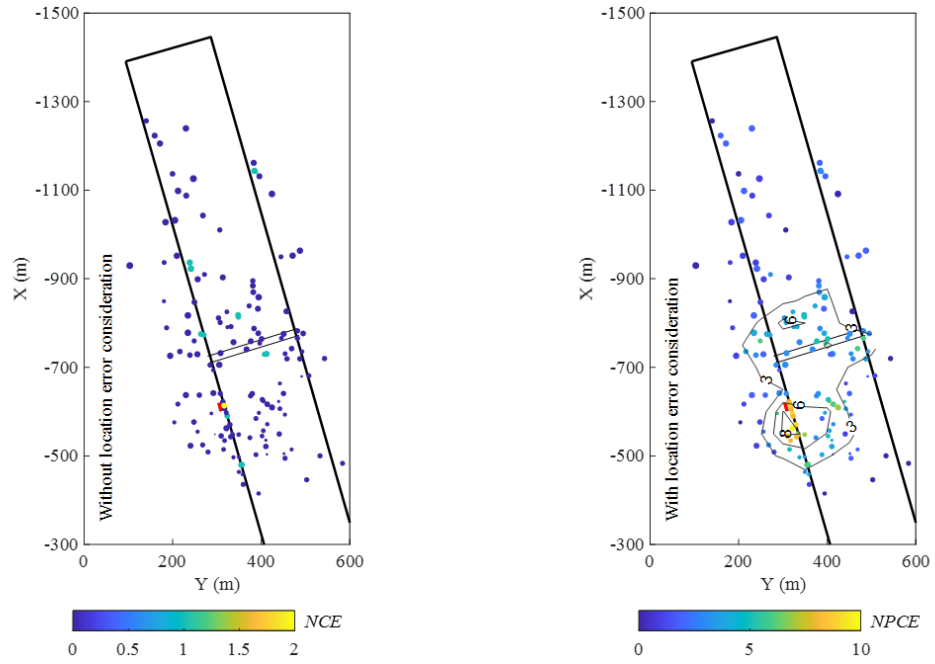
the right in Figure 5-6 range from 10 to 26, which are 2–5 times higher than the *NCE* results. Medium-high *NPCE* zones are mainly located on the tailgate side, where coal burst damage has been recorded several days later. It demonstrates that by considering seismic location errors, *NPCE* results are more applicable in assessing coal burst risks.



(a) Time period: 17–23 May 2014. Coal burst date: 27 May 2014



(b) Time period: 9–15 September 2014. Coal burst date: 22 September 2014



(c) Time period: 4–10 November 2014. Coal burst date: 16 November 2014

Figure 5-6 Examples of clustering results of LW250105 without (left) and with (right) considering location errors. The red zone is the coal burst damage which occurred in the next week, and the contours are the number of clustered events.

5.4 Seismic clusters and coal burst damage

To study the relationship between seismic clusters and coal burst hazards, coal burst damage and the *NPCE* results in LW250105 during the study period were back analysed. *NPCE* analysis was conducted on a weekly basis, using the procedure shown in Figure 5-7. Based on the seismic data of a week, a *NPCE* scatter plot was first derived by using the method in Section 5.3 (see Figure 5-7a). Then, by using a linear interpolation algorithm with grid space of 50 m, the *NPCE* scatter plot was transformed to a contour map (see Figure 5-7b). Finally, the *NPCE* values on the tailgate in front of the longwall face were extracted from the contour map (see

Figure 5-7c). To compare with the coal burst damage that occurred in the next week, a normalised R_{NPCE} is used to represent $NPCE$ distributions on the tailgate:

$$R_{NPCE} = \frac{NPCE}{NPCE_{max}} \quad (5-11)$$

where $NPCE_{max}$ is the maximum $NPCE$ value on the tailgate in front of the longwall face, R_{NPCE} ranges between 0 and 1. The reason for using R_{NPCE} instead of absolute $NPCE$ values is there are multiple factors controlling the number of seismic events. These factors are not only stress conditions and geological structures, but also mining rate, pre-destressing operations, and support conditions. These factors vary along with the mining process, which may result in a large difference in the number of seismic events between different periods. Therefore, it is impractical to directly compare $NPCE$ results or propose a criterion with absolute $NPCE$ values to identify coal burst risks. Instead, the focus should be on the normalised $NPCE$ in each period to assess coal burst hazard potential.

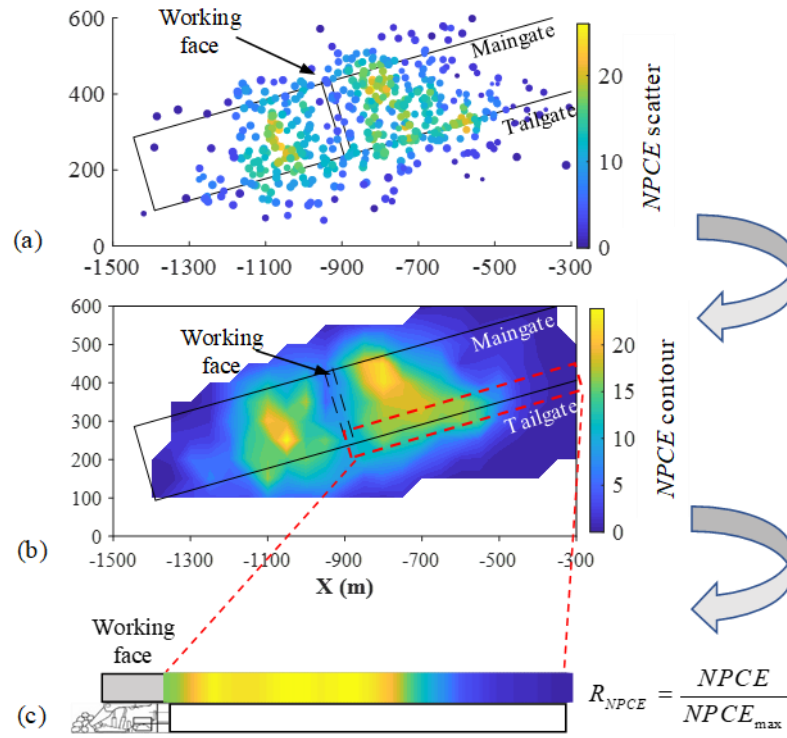


Figure 5-7 Results of (a) $NPCE$ scatter, (b) $NPCE$ contour and (c) R_{NPCE} for 9–15 September 2014

Figure 5-8 is the R_{NPCE} distributions on the tailgate ahead of the longwall face and the corresponding coal burst damage zones in the next week. It shows that 70% of the coal burst damage occurred within 100 m in front of the longwall face (16 of 23 events). This demonstrates that the tailgate within 100 m in front of the panel face had a significant burst hazard potential because of the mining-induced abutment pressure. Three of the studied coal bursts (13 April, 16 September and 13 December) occurred from 600 m to up to 1300 m away from the longwall face. This implies that the coal burst hazard could still be triggered in an area that is far away from the mining activity. But as the damage zones were not covered by enough geophones, these three coal bursts have no R_{NPCE} result due to the lack of seismic events.

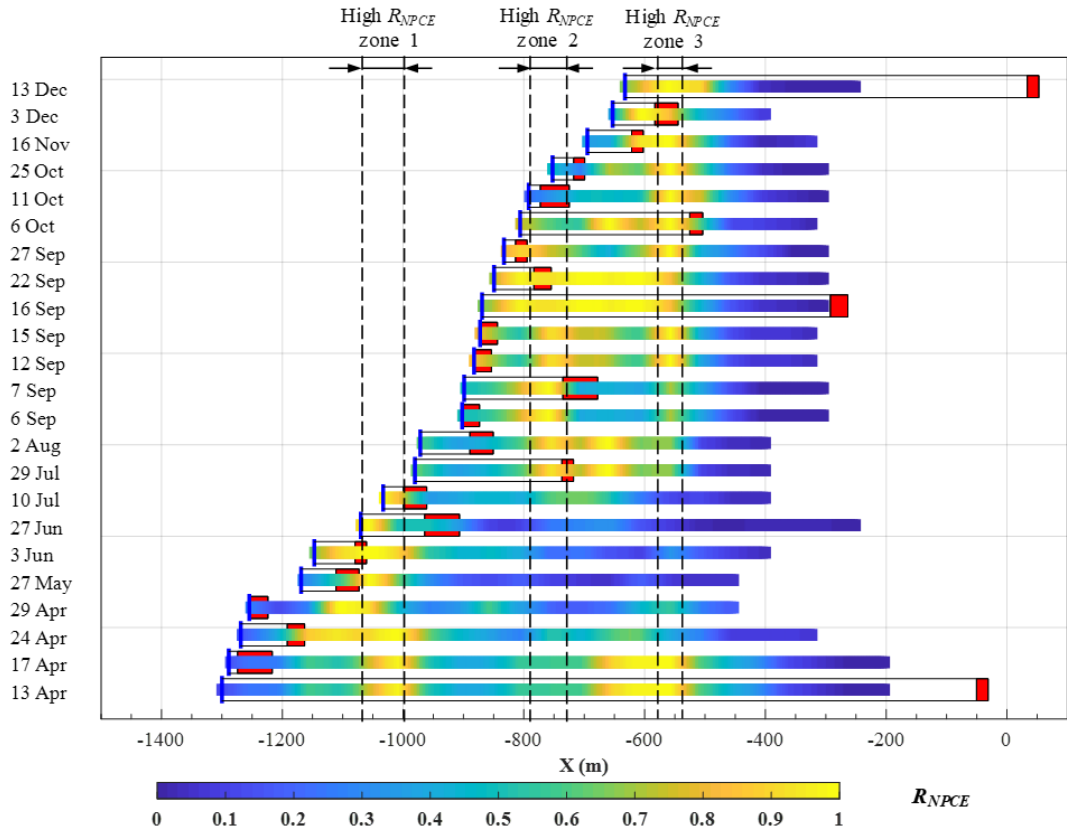


Figure 5-8 Coal burst damage zones and the latest tailgate R_{NPCE} distribution ahead of the longwall face in LW250105. The red zone is the coal burst damage zone. The blue line is the longwall face position.

Based on the result in Figure 5-8, the R_{NPCE} in coal burst damage zones (red shaded areas in this figure) can be extracted for further investigation. Figure 5-9 shows the minimum, average and maximum R_{NPCE} values within damage zones of the remaining 20 coal bursts. In this figure, the results are presented in ascending order of the average R_{NPCE} values rather than chronological order. It shows that 75% of the burst damage zones (15 of 20) are located in the zone with maximum $R_{NPCE} > 0.5$, and 65% (13 of 20) of the burst damage zones have maximum $R_{NPCE} > 0.7$. Similar results occur in the average R_{NPCE} of burst damage zones, where 70% of the burst damage zones (14 of 20) have average $R_{NPCE} > 0.5$, and 45% (9 of 20) have average $R_{NPCE} > 0.7$. It demonstrates a high probability of coal burst hazards in high R_{NPCE} zones.

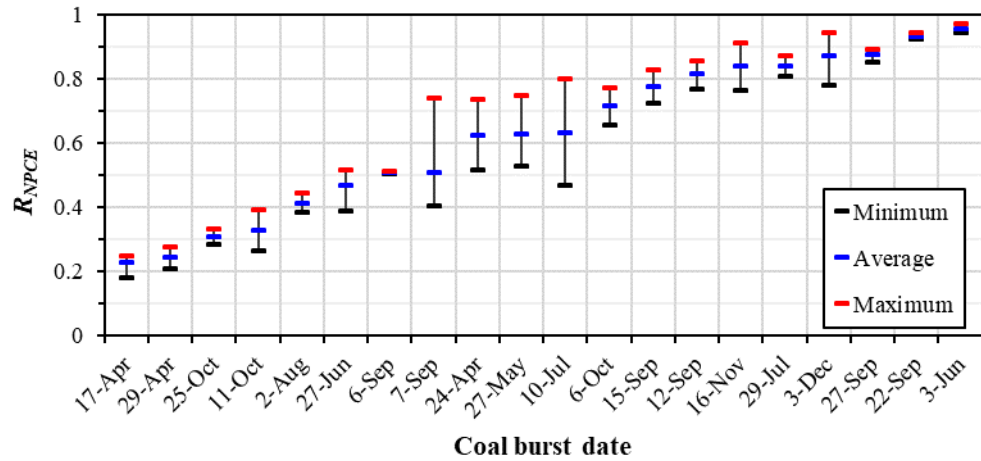


Figure 5-9 Minimum, average and maximum R_{NPCE} in burst damage zones in LW250105

Figure 5-8 also indicates that three tailgate zones with R_{NPCE} of more than 0.8 have lasted more than 2 months during mining. These long-time high R_{NPCE} zones were detected 100 m or even more than 300 m in front of the longwall face. Nearly half (9 of 20) of the coal burst damages occurred within or near these zones. According to the mechanism of the seismic cluster, it can be inferred that these high R_{NPCE} zones are related to minor geological structures. These minor geological structures were hardly detected by a geological survey, but they could cause unexpected high stress concentrations and induce “structurally controlled strainburst”, as referred to in Section 2.2.2. According to the $NPCE$ results, these inferred geological structure zones were identified more than 2 months prior to the longwall passing by. Therefore, $NPCE$ analysis can also be used to assess medium to long term coal burst hazards in roadways.

Figure 5-10 presents the relationship of the maximum R_{NPCE} of the studied coal bursts, and the corresponding distances from the longwall face to the nearest roadway geophone and to the coal burst damage zones. There are five coal burst damage zones located in the zone with maximum $R_{NPCE} < 0.5$, which are marked in red in Figure 5-10. These coal bursts have two common characteristics: (i) the damage zones are near the longwall face, and (ii) the longwall face is far away from

the nearest roadway geophone. According to the geophone location changes indicated by the arrows in Figure 5-10, these five coal bursts all occurred within a month after each change. At the same time, the nearest roadway geophone was placed more than 250 m away from the longwall face. Four of these five coal burst damage zones are located within 50 m in front of the longwall face. As the longwall face approached the nearest geophone with their distance smaller than 200 m, higher R_{NPCE} values in the coal burst damage zones are present. It implies that $NPCE$ analysis could be highly insensitive to the hazards near the longwall face if geophones are distantly placed. This phenomenon can be illustrated by the lower seismic monitoring sensitivity of the area near the longwall face. Restricted by the roadways' layout, the area near the longwall face is generally not well covered by geophones. This deficiency not only causes high location errors but also reduces monitoring sensitivity. As a result, usually only a few seismic events can be recorded around the longwall. This incomplete seismic data leads to limited cluster information in the area near the longwall face, which may cause medium-low R_{NPCE} results.

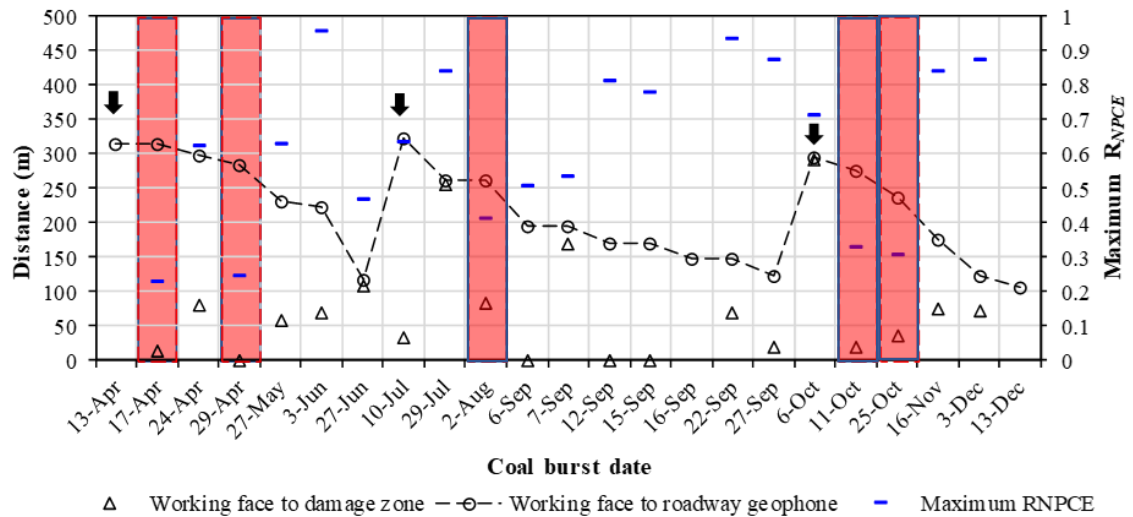


Figure 5-10 Distances from the longwall face to the nearest geophone (triangle) and damage zone (circle). The filled zone indicates coal bursts with maximum R_{NPCE} lower than 0.5. The arrow means the first coal burst before geophone location changes.

In order to determine the risk threshold of R_{NPCE} to identify coal burst hazards, the accuracy and efficiency for predicting coal burst hazards in LW250105 were investigated. The accuracy of hazard prediction, i.e. the true positive, is defined as the number of coal burst events that are reported in the target risk zones. The efficiency of hazard prediction, i.e. the true negative, is defined as the ratio of burst damage length to the identified risk zone length. Since it has been stated in Section 2.4.1 that the burst risks are still difficult to be assessed in the time domain, the research mainly focused on studying the accuracy and efficiency of hazard prediction in the space domain. Therefore, the R_{NPCE} threshold with higher accuracy and efficiency indicates a lower false positive and false negative. Figure 5-11 shows the accuracy (red columns) and efficiency (blue line) for predicting the 20 coal burst cases in LW250105 with different R_{NPCE} thresholds, varying from 0.1 to 0.9. This figure indicates that the accuracy decreases while the efficiency increases with the increase of the R_{NPCE} thresholds. When R_{NPCE} is 0.7, the hazard prediction has both a relatively high accuracy (13/20) and efficiency (0.26). Therefore, it is reasonable to conclude that 0.7 of R_{NPCE} would be the optimal risk threshold to identify coal burst risks.

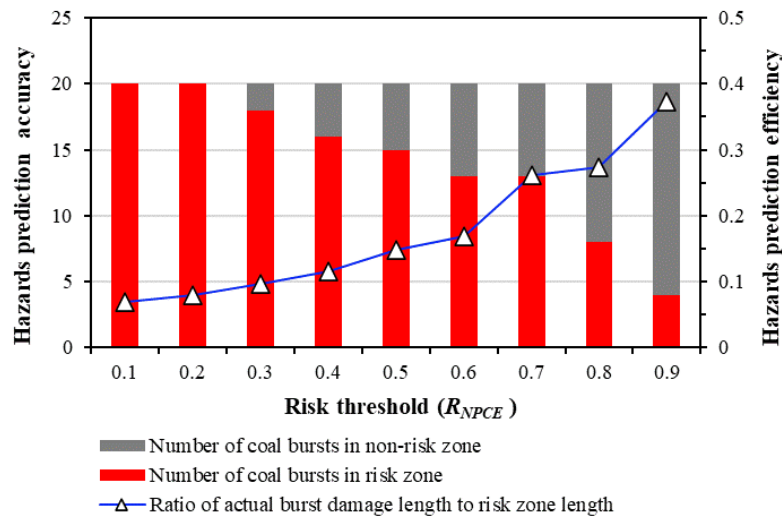


Figure 5-11 Accuracy (marked as red columns) and efficiency (marked as blue line) for hazard prediction when using different R_{NPCE} as the risk threshold in LW250105

5.5 Summary

This chapter investigated the evolution characteristics of location errors during longwall mining and proposed a modified seismic clustering method to eliminate impacts from location errors. In LW250105, different distributions on location errors were found in the panel when the geophone layout was modified. The area located between 50 to 300 m ahead of the longwall face commonly had the highest location accuracy, with a location error of approximately 20 m. Insufficient geophone coverage was evident in the goaf zone and over 300 m ahead of the longwall face, where the location errors can be more than 80 m. Furthermore, the patterns of location errors exhibited strong anisotropic characteristics.

The proposed seismic clustering method, *NPCE* analysis, considers location errors in the clusters of events and reduces the influence of poorer locating accuracy on coal burst hazard predictions. The *NPCE* analysis can provide 2–5 times more seismic clustering information and more robust results than the conventional clustering analyses. A normalised *NPCE* index, R_{NPCE} has been proven to have a positive relationship with coal burst hazards. In addition, long duration high R_{NPCE} zones were identified more than 2 months prior to the longwall face passing by, where nearly half of the coal bursts occurred. Therefore, *NPCE* analysis has the potential to be used as an effective method for coal burst hazard assessment.

This chapter provides a possible solution for minimising locating error and its impacts on seismic analysis in underground mines. Like any other seismic method, the proposed *NPCE* analysis would also be affected by the flaws of seismic monitoring such as greater incompleteness of seismic data and limitations on effective detection range. Therefore, it is more appropriate to combine *NPCE* analyses with other non-seismic techniques for reliable hazard assessment. In Chapter 6, another aspect to appraise the seismic monitoring performance, the

seismic data integrity, will be investigated in LW250105, and its impacts on event counts and seismic energy will be discussed.

Chapter 6. A statistical method to assess data integrity and reliability of seismic monitoring systems

The content of this chapter has been published as a paper in the journal ***Rock Mechanics and Rock Engineering***.

<https://doi.org/10.1007/s00603-021-02597-7>

For the brevity and consistency of the thesis, repeated content has been removed and a concise introduction is presented.

6.1 Introduction

In the previous Chapter, the location error evolution characteristics in LW205015 were analysed, and a new seismic clustering method was proposed to improve forecasting of coal burst risks by considering location errors. In this chapter, another factor that impacts seismic data reliability, the seismic data integrity, is examined.

In Section 2.5.2, various methods for determining m_c in the seismology community were introduced, which can be used to assess seismic data integrity. However, due to the multiple seismic sources in the underground mining environment, it is challenging to determine a robust m_c from a variety of seismic populations in mines. In contrast to the earthquake catalogues that are induced by the same major geological structure, mining-induced seismicity is the mixed response of multiple geological structures around the mining area (Gibowicz and Lasocki, 2001). To follow the Gutenberg–Richter law, i.e. the self-similarity characteristic, mining-induced seismicity needs to be clearly distinguished by different geological sources, which is rare in mining (Mignan et al., 2011). Therefore, it is less likely for mining-induced seismicity to follow the Gutenberg–Richter law if mixed geological sources in space and/or time are present. Also, other seismic sources in underground mines, such as equipment operating noise and drilling and blasting, may further increase the variety of seismic populations in mines.

Therefore, it is essential to develop a method that can effectively assess seismic data integrity and reliability in underground mines that is:

- unconstrained by areas with sparse data and able to provide an acceptable resolution of results in the entire area of interest;
- free from following the Gutenberg–Richter law and insensitive to different sources of seismicity for analysis; and

- using as much raw seismic data as possible for analysis to ensure the reliability of the results.

An innovative method based on the probability of detecting earthquakes was proposed by Schorlemmer and Woessner (2008), referred to as the *PDE* method. Instead of deterministically picking one m_c value from raw seismic monitoring data, the *PDE* method assesses seismic data integrity based on the detection probability analysis of an array of sensors. The wave picking capability of each seismic sensor was firstly assessed based on the identification of wave onset time picking. Then, the detection probability for seismic events within the monitoring area outlined by the sensor array was calculated based on the probability that seismic waves of seismicity could be picked by no less than four sensors at various locations as four sensors is the minimum requirement to detect a seismic event. The *PDE* method assesses the event detection probability of a seismic monitoring system based on the energy magnitudes of events and hypocentral distances. Therefore, it is not limited to the sparse seismic data in space and can calculate detection probabilities in the entire area of interest. Different from giving a certain m_c value, an event detection probability distribution for seismic events with different locations and energy levels can be derived by using the *PDE* method, which provides more detailed information to assess seismic data integrity. Also, as the *PDE* method does not follow the Gutenberg–Richter law assumption, seismic events from all types of sources are acceptable. As a result, most seismic data with an entire energy range can be used for analysis.

This chapter applies the *PDE* method to LW250105 to evaluate the detection probability of its seismic monitoring system. For a better illustration of the method, three months of seismic data from 1 July to 29 September 2014 are selected for analysis. The *PDE* method is first customised to fit the mining context. The wave picking capability of geophones is then evaluated, and the event detection

probability of the seismic monitoring system for seismic events with different locations and energy magnitudes are calculated. Based on the detection probability results, a new method is proposed to enrich the original seismic data and improve data integrity. The outcome of this work can provide an insight into assessing data integrity and improving the accuracy of seismic analyses in underground mines.

6.2 Methodology of the probability of detecting earthquakes (PDE)

6.2.1 Wave picking capability of individual geophones (P_D)

The wave picking capability of an individual geophone is related to the signal intensity of the seismic wave and the associated mining and geological environments. A seismic event picked by a geophone means that the onset time of its seismic wave is picked for locating the event and calculating its source parameters. In this Chapter, the energy of a seismic event is represented by its energy magnitude, referred to as $\log E$. For example, a 1 kJ seismic event has an energy magnitude of 3 ($\log E=3$). For seismic events with higher energy magnitudes and lower hypocentral distances, the seismic wave commonly has higher intensity and signal-to-noise ratio, which is easier to be picked by geophones (see Figure 6-1a). On the other hand, for seismic events with lower energy magnitudes and higher hypocentral distance, the seismic wave tends to have more diffraction and attenuation. In this case, the onset time of the seismic wave is less likely to be picked due to the mixture of high amplitude noise (see Figure 6-1b). Therefore, for an individual geophone, the wave picking capability can be represented by plotting picked and unpicked seismic events in the hypocentral distance–energy magnitude coordinate, referred to as the D-M map, which is shown in Figure 6-2a. In a D-M map, the zone with more picked seismic events indicates a higher wave picking capability of that geophone at the

corresponding distance and energy magnitude, and a lower wave picking capability is present in the zone where more unpicked events are plotted.

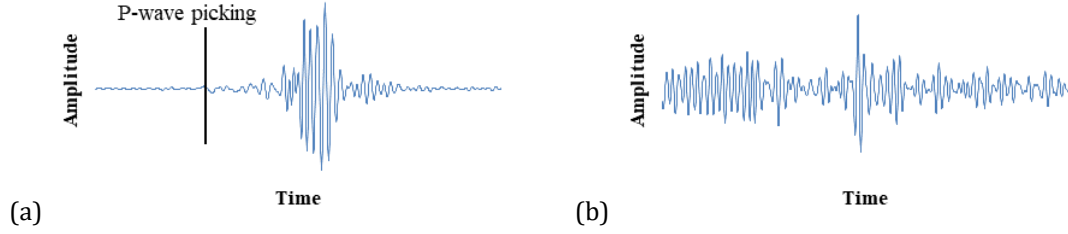


Figure 6-1 Example of pickable (a) and unpickable (b) seismic waves

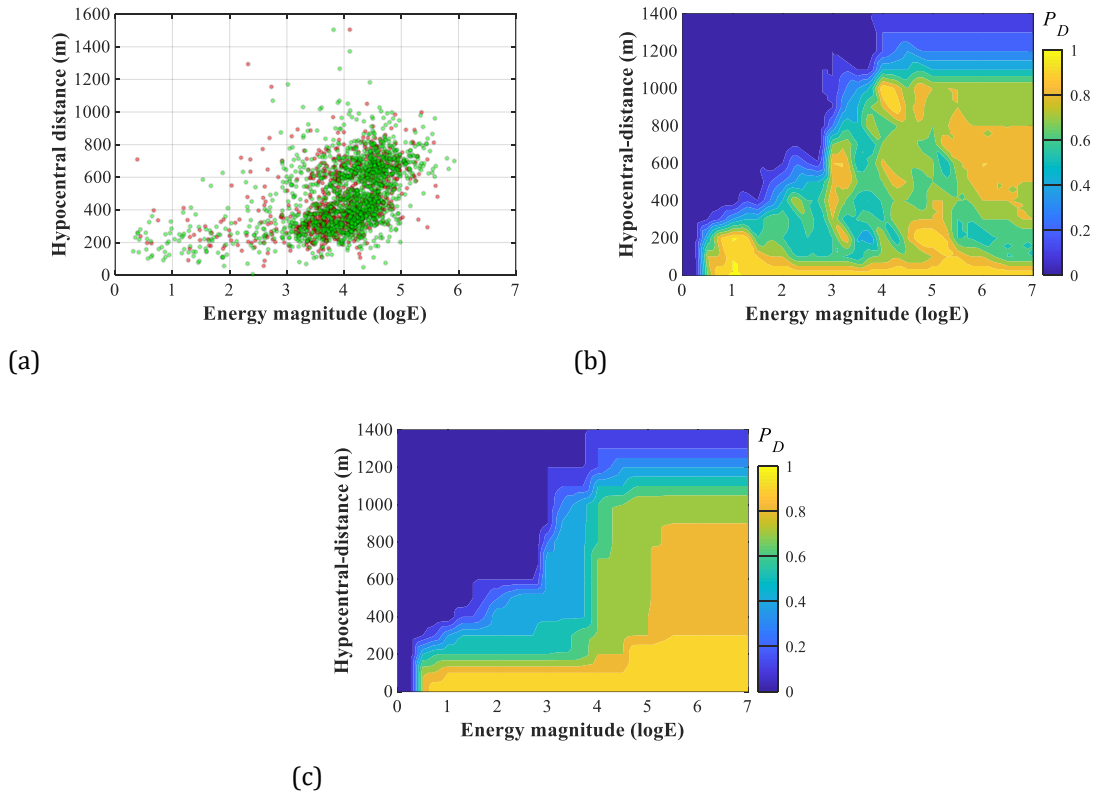


Figure 6-2 Example of (a) D-M map showing distributions of picked (marked with green) and unpicked (marked with red) seismic events by a geophone, (b) P_D distribution calculated from (a), and (c) P_D distribution after applying physical constraints

Before quantifying the wave picking capability of a geophone, it is necessary to unify the units of hypocentral distance and energy magnitude in the D-M map. In

underground mines, the relationship between peak particle velocity of seismic wave (ppv), energy magnitude and hypocentral distance can be simplified as:

$$\log E = c_1 \log(ppv) + c_2 \log R + c_3 \quad (6-1)$$

where c_1 , c_2 and c_3 are constants, which are determined by field observations, and R is hypocentral distance. For two seismic events with the same ppv recordings in a geophone but different hypocentral distances, their energy magnitude difference can be calculated by:

$$\Delta \log E^* = |c_2 \log R_1 - c_2 \log R_2| \quad (6-2)$$

Based on Eq. (6-2), the distance between two events on the vertical axis of the D-M map can be converted to the energy magnitude difference, $\Delta \log E^*$ (see Figure 6-3a). Therefore, the distance between a seismic event $(\log E_1, R_1)$ and another event $(\log E_2, R_2)$ in the D-M map is:

$$R_M = \sqrt{\Delta \log E^2 + \Delta \log E^{*2}} \quad (6-3)$$

where

$$\Delta \log E = \log E_1 - \log E_2 \quad (6-4)$$

The relationships between R_M , $\Delta \log E$ and $\Delta \log E^*$ are shown in Figure 6-3a.

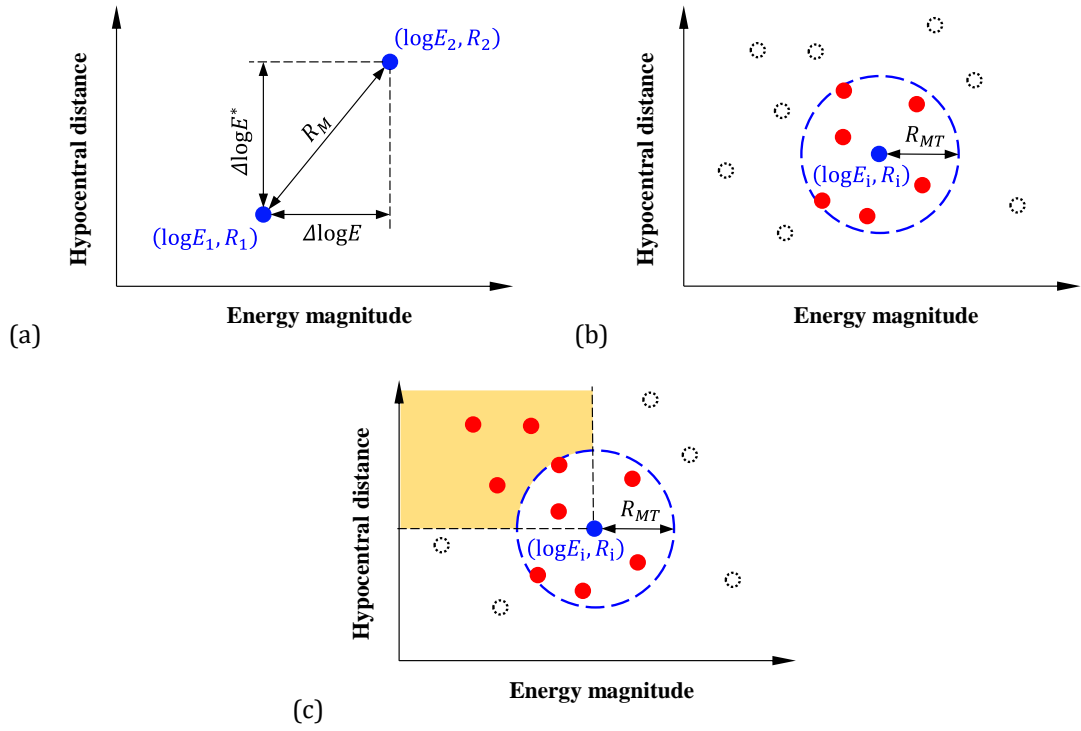


Figure 6-3 In a D-M map: (a) distance (R_M) between two seismic events (marked in blue), (b) selected seismic events (marked in red) for P_D calculation at a point $(\log E_i, R_i)$ within the radius R_{MT} (marked in blue dashed lines), and (c) selected seismic events for P_D calculation at a point $(\log E_i, R_i)$ within the radius R_{MT} and the extended zone (marked in yellow). Dashed dots are the unselected events.

The D-M map is then divided into grids, and R_M can be used to describe the distance from a seismic event to a grid point. At each grid point i , the wave picking capability for a geophone to a given energy magnitude and a hypocentral distance is represented as $P_D(\log E_i, R_i)$. Assume a searching radius R_{MT} in the D-M map, the seismic events with $R_M < R_{MT}$ are selected as sample events to calculate $P_D(\log E_i, R_i)$ (see Figure 6-3b). R_{MT} is related to the magnitude error when the monitoring system measures seismic events. Following Schorlemmer and Woessner (2008), R_{MT} is set as 0.1. For the selected sample events, their number N_{T1} is the sum of the number of sample events whose waves have been picked by the geophone (N_+) and the number of sample events whose waves have not been picked by the

geophone (N_-). $P_D(\log E_i, R_i)$ can be calculated as below, which is a probability parameter with values from 0 to 1:

$$P_D(\log E_i, R_i) = \begin{cases} \frac{N_+}{N_+ + N_-} & (N_+ + N_- \geq N_{min}) \\ \frac{N_+}{N_{min}} & (N_+ + N_- < N_{min}) \end{cases} \quad (6-5)$$

where N_{min} is the minimum number of sample events for P_D calculation at one grid point. The determination of N_{min} should ensure both the robustness and effectiveness of the results. In this study, 9 is adopted as the optimal N_{min} value to calculate the detection capabilities of geophones in the study longwall. The determination procedure of N_{min} is illustrated in Section 6.4.2.

According to the sparse data characteristics in the D-M map, it is possible that at some grid points the N_{T1} will be lower than N_{min} . In this case, the seismic events with $R_M > R_{MT}$ and located on the top-left corner of the grid point i in the D-M map are used as the supplementary sample events for P_D calculation (see Figure 6-3c). The supplementary sample events are sorted in descending order by R_M , and their number is marked as N_{T2} . The $P_D(\log E_i, R_i)$ is then calculated in two scenarios:

- (1) If $N_{T2} > N_{min} - N_{T1}$, select the first $N_{min} - N_{T1}$ supplementary sample events for P_D calculation based on Eq. (6-5) under the condition of $N_+ + N_- \geq N_{min}$.
- (2) If $N_{T1} + N_{T2} < N_{min}$, select all the supplementary sample events for P_D calculation based on Eq. (6-5) under the condition of $N_+ + N_- < N_{min}$, which treats seismic waves of undetected seismic events as unpicked (referred to as dummy events).

The procedure of selecting sample events for P_D calculation is also illustrated in the flow chart presented in Figure 6-4. It should be noted that the detection capability

of geophones is conservatively calculated by using supplementary seismic events. These supplementary seismic events on the top-left corner in the D-M map are the sources with lower energy levels and higher hypocentral distances, which is less likely to be detected by the geophone. Therefore, the calculated $P_D(\log E_i, R_i)$ at each grid point would be lower than the actual detection capability. Since the main purpose of the seismic analyses in mines is to forecast seismic hazards, the underestimation of detection capabilities of geophones will help attract more attention to the potential seismic risks from the undetected seismicity.

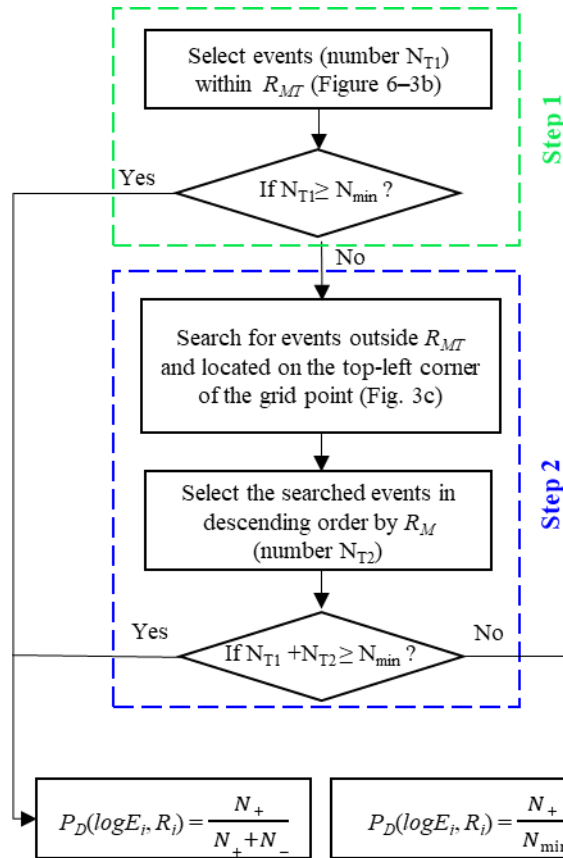


Figure 6-4 Flow chart of sample events selecting procedure for $P_D(\log E_i, R_i)$ calculation

Figure 6-2b is an example of P_D distribution of an individual geophone calculated from Figure 6-2a. It shows that P_D at the bottom-right corner of the D-M map is lower than that at other zones with lower magnitudes or higher hypocentral distance. This result does not obey physics as it is more likely to pick seismic waves

for seismic events with higher energy levels and lower hypocentral distance. This counterintuitive phenomenon is mainly due to conservative algorithms used for P_D calculation in the sparse data zone, and highly heterogenic coal and rock mass in the mining environment. In this study, only the influence of sparse data is considered. Since few strong seismic events have been detected at the bottom-right corner of the D-M map, P_D calculated by the conservative algorithms presents a lower value at higher energy magnitude zones. Therefore, two physical constraints are applied for P_D distribution in the D-M map: (1) P_D at each grid point is not allowed to be higher than that of other grid points with larger energy magnitudes and lower hypocentral distances, and (2) P_D at each grid point is not allowed to be lower than that of other grids with lower energy magnitudes and larger hypocentral distances. Figure 6-2c is the P_D distribution of an individual geophone after applying these constraints, which corrects the false P_D results induced by the sparse data in the D-M map and provides wave picking capability of a geophone that follows the attenuation principles of seismic waves.

6.2.2 Event detection probability of the monitoring system (P_E)

As mentioned above, for locating purposes, a seismic event can only be recorded in the dataset when its seismic waves are picked by at least four geophones. Therefore, the probability of the seismic monitoring system capturing a seismic event with a specific energy magnitude, $P_E(x, y, \log E)$, is equivalent to the probability of its seismic waves being picked by four or more geophones. It also equals one minus the sum of probabilities of a seismic event being picked by less than four geophones:

$$P_E(x, y, \log E) = 1 - \sum_{n=0}^3 P_E^n \quad (6-6)$$

where P_E^n is the probability of a seismic event detected by n geophones. Assume m geophones are active in the monitoring system, the number of geophone combinations is:

$$C_m^n = \frac{n!}{m!(m-n)!} \quad (6-7)$$

For the k^{th} geophones combination among C_m^n , its detection probability $P_E^{n(k)}$ can be calculated as:

$$P_E^{n(k)} = \prod_{p=1}^n P_D^{G(p)} \cdot \prod_{q=1}^{m-n} (1 - P_D^{\bar{G}(q)}) \quad (6-8)$$

where $G(p)$ represents the p^{th} geophone within the combination, $P_D^{G(p)}$ is the detecting probability of the p^{th} geophone, and $\bar{G}(q)$ is the q^{th} geophone that is excluded in the combination. Therefore, P_E^n is the $P_E^{n(k)}$ summation of all geophone combinations:

$$P_E^n = \sum_{k=1}^{C_m^n} P_E^{n(k)} \quad (6-9)$$

Figure 6-5 gives an example of calculating P_E^3 in a five-geophone monitoring system. All P_D values of individual geophones shown here can be calculated using the method explained in Section 6.2.1. According to Eq. (6-7), there are ten possible combinations of three geophones that have picked the seismic waves. For the second combination (seismic event detected by geophones #1, #2 and #4), its detection probability $P_E^{3(k=2)}$ is calculated as 0.0036 in Figure 6-5c by using the parameters listed in Figure 6-5b. According to Eq. (6-9), detection probabilities of all the possible combinations are summed up and P_E^3 turns out to be 0.3618.

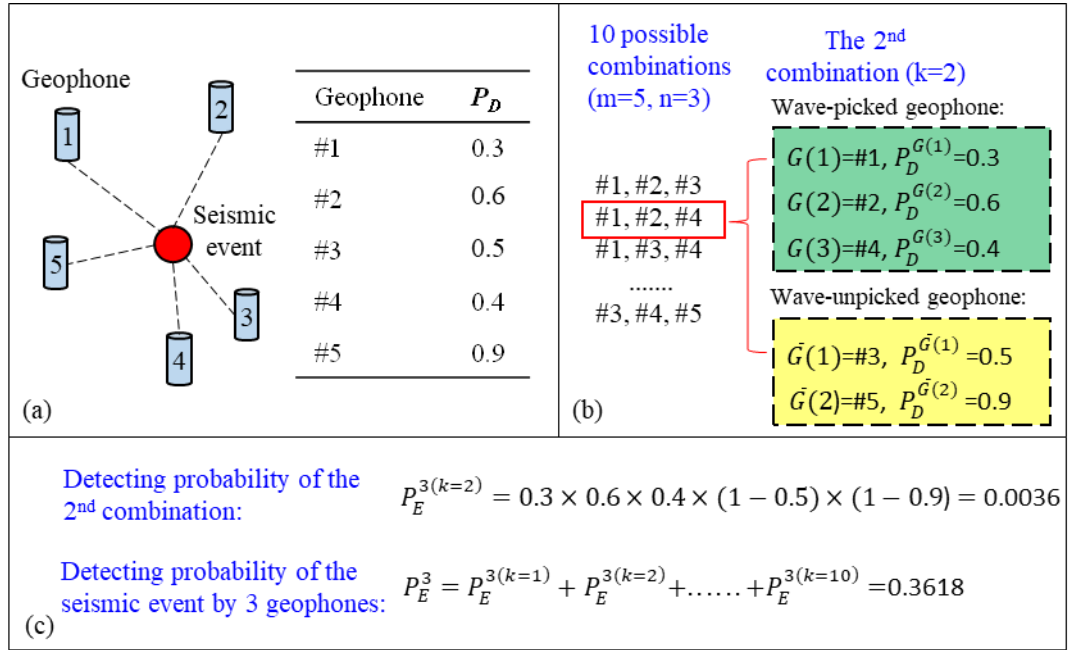


Figure 6-5 Event detection probability of a seismic event by three geophones in a monitoring system with five geophones (P_E^3). (a) P_D of individual geophones for a seismic event. (b) The second geophone combination (geophones #1, #2 and #4) is taken as an example to calculate the probability of the seismic event picked by them. The green-shaded zone marks the parameters of geophones that have picked the seismic waves (geophones #1, #2 and #4), and the yellow-shaded zone marks the parameters of geophones that have not picked the seismic waves (geophones #3 and #5). (c) Calculation of the event detection probability by geophones #1, #2 and #4 ($P_E^{3(k=2)}$) and the summation of detecting probability by three geophones (P_E^3).

The area of interest is gridded and the detection probability P_E for a given energy magnitude $\log E$ is calculated at each grid point using Eq. (6-6). On the other hand, the detectable energy magnitude as a function of P_E can be expressed as $\log E(x, y, P_E)$. For a given P_E , this indicates the distribution of energy magnitudes required for the monitoring system to reach the specified detection probability P_E . If P_E is set as 100%, $\log E(x, y, P_{E(1.00)})$ is then the minimum energy magnitude that can be fully detected by the monitoring system, i.e. the magnitude of completeness.

6.2.3 Correction of event counts and seismic energy based on detection probability

According to the *PDE* method, the seismic data integrity in underground mines is mainly controlled by the event detection probability of the seismic monitoring system. If the detection probabilities for seismic events to be monitored are known, it is possible to back-calculate undetected seismic events and estimate the actual number of seismic events. Assume m seismic events are monitored in a grid zone and their corresponding detection probabilities are $P_E(x_1, y_1, \log E_1)$, $P_E(x_2, y_2, \log E_2)$, $P_E(x_n, y_n, \log E_n)$, the corrected number of events that may have occurred in this grid zone can be calculated as:

$$m' = 1/P_E(x_1, y_1, \log E_1) + 1/P_E(x_2, y_2, \log E_2) \cdots + 1/P_E(x_n, y_n, \log E_n) \quad (6-10)$$

and the corrected sum of seismic energy of these m' seismic events can be calculated as:

$$E_{sum} = E_1/P_E(x_1, y_1, \log E_1) + E_2/P_E(x_2, y_2, \log E_2) \cdots + E_n/P_E(x_n, y_n, \log E_n) \quad (6-11)$$

For example, if ten seismic events with energy magnitudes of 3 (1 kJ) are detected in a grid zone and their corresponding P_E is 0.5, the corrected number of seismic events is 20 and the sum of energy is 20 kJ. Different from conventional m_c analyses, the proposed seismicity correcting method uses the raw seismic data as much as possible to recover undetected seismic events, which can best approximate actual seismic activities. Therefore, this method can be a potential approach to eliminate the bias caused by an incomplete seismic dataset.

6.3 Detection probability assessment in LW250105

6.3.1 Wave picking capabilities of geophones (P_D)

The seismic data during the period from July to August 2014 was used to assess the P_D of active geophones in LW250105. The D-M map for each active geophone was gridded with spacings of 0.25 in energy magnitude and 100 m in hypocentral distance. Figure 6-6 shows the picked and unpicked seismic events distribution in the D-M map of the six active geophones. The results indicated significant differences between geophones in the number of picked events. Geophone #16 picked seismic waves of most of the events, which account for 98% of the total events. In contrast, only 29% of the seismic events were picked by geophone #11. As geophones #1 #2, #7, #13 and #16 were located close to the LW250105 retreat area, seismic events with a wide energy magnitude ranging from less than 1 to more than 6 can be picked (see Figure 6-6a, b, c, e, f). However, due to the increasing distance to the longwall face and a strong anisotropy induced by the large goaf zone in between, geophone #11 can only pick seismic events with energy magnitudes larger than 3 (see Figure 6-6d). Regardless of the sparse seismic data, all geophone D-M maps mostly followed the principle that seismic events with higher energy magnitudes and lower hypocentral distances are more likely to be detected.

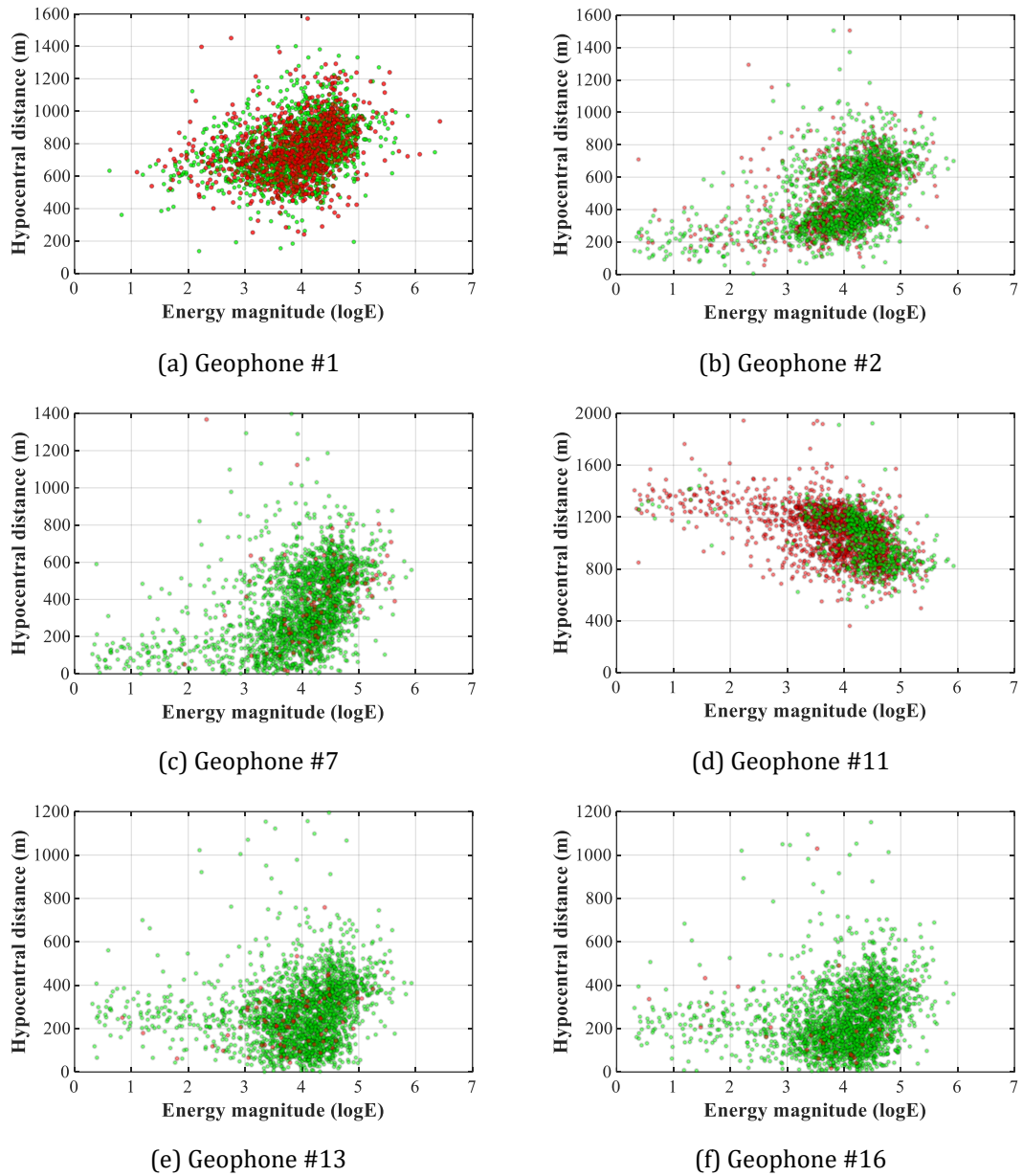


Figure 6-6 Distribution of picked (marked with green) and unpicked (marked with red) events in the D-M map of five active geophones in LW250105

Figure 6-7 is the P_D contours in the D-M map of different geophones, showing a significant difference in seismic detection capabilities between geophones. Geophones #7 and #16 had a relatively higher wave picking capability for seismic events. A 100% seismic detection ($P_D=1.00$) can be achieved for seismic events with energy magnitudes of 2 to 7 (from 0.01 kJ to 10000 kJ) and hypocentral distances of 200 m to 800 m (see Figure 6-7c, f). Geophone #13 had a similar 100% wave picking

capability for seismic events with energy magnitudes of 3 to 7 with hypocentral distance of less than 500 m. However, less than 90% P_D was evident for the seismic events with energy magnitudes of less than 3 and hypocentral distances of less than 300 m for geophone #13. To achieve 100% wave picking capability, seismic events recorded by geophone #2 need to have energy magnitudes of more than 5 and hypocentral distances of less than 800 m (see Figure 6-7b). By analysing historical seismic signals using the *PDE* method, less than 50% P_D of geophone #2 occurred for the seismic events with energy magnitudes of less than 4 (i.e., 10 kJ). It implies that geophone #2 might have missed approximately half of the seismic events in medium-low energy levels. The P_D distribution of geophone #11 indicated its insensitivity in terms of picking waves of seismic events (see Figure 6-7d). The highest P_D of geophone #11 is 70%, which can be achieved only by picking waves of seismic events with energy magnitudes more than 5 (1000 kJ) and hypocentral distances less than 1000 m. Geophone #11 had less than 50% P_D in picking waves of seismic events with energy magnitudes of 4, and it might have missed most of the seismic events with energy magnitudes of less than 4.

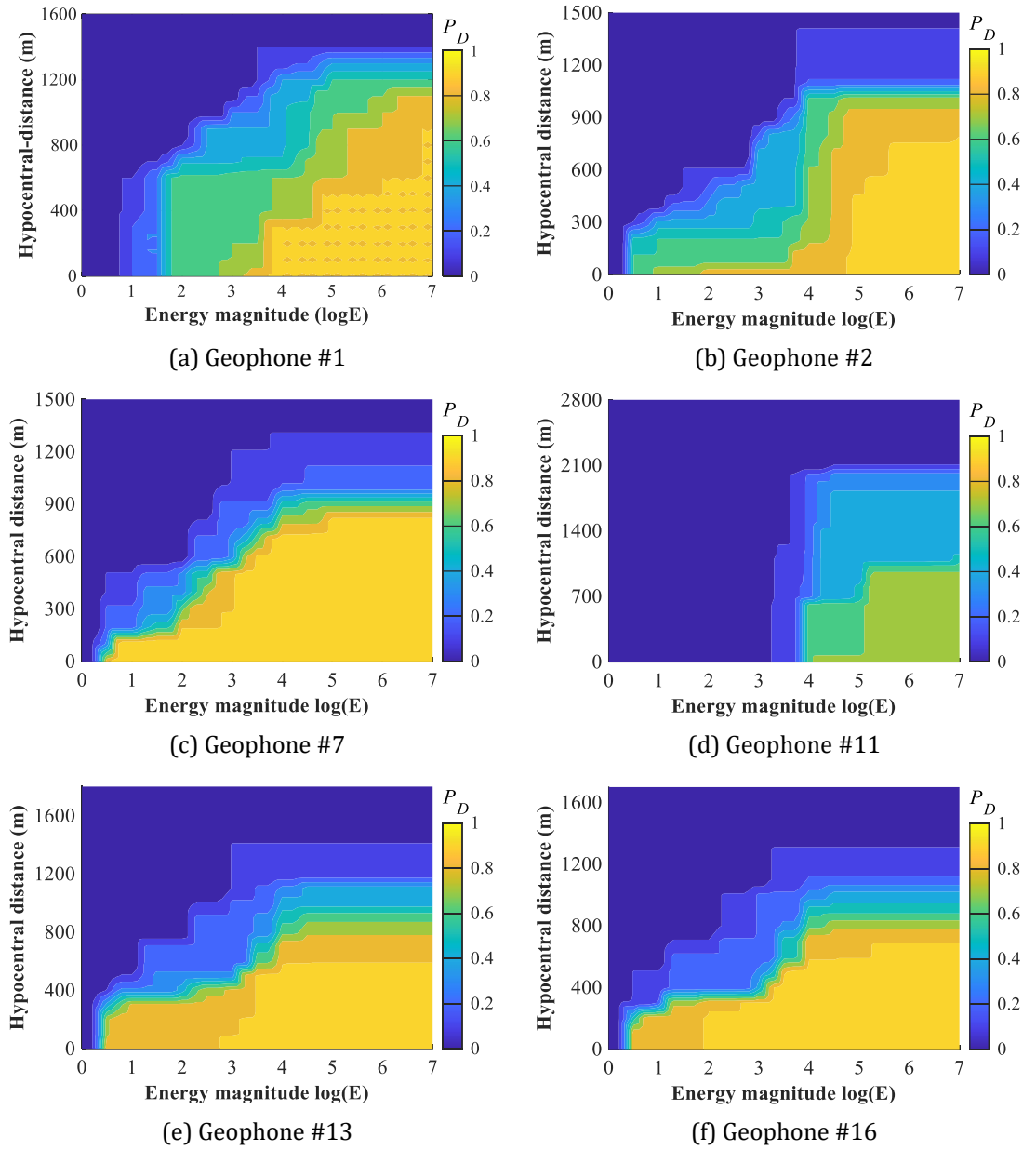


Figure 6-7 Wave picking capability P_D of five active geophones in LW250105

6.3.2 Event detection probability of the seismic monitoring system (P_E)

Based on the P_D results in Figure 6-7, the P_E distribution in LW250105 for seismic events in different energy levels can be derived using the method explained in Section 6.2.2. The area of interest was divided into grids of 50 m for calculation. The results are shown in Figure 6-8. In general, for seismic events with higher energy magnitudes, the seismic monitoring system has a higher event detection

probability and a broader detection range. Also, as the significant abutment pressures and the existence of invisible geological discontinuities, the majority of seismic events are located ahead of the longwall face where relatively high P_E values are presented. In Figure 6-8a, seismic events with an energy level of 0.1 kJ ($\log E=2$) can be detected in a limited zone ahead of the retreat area with P_E mostly less than 70%. For seismic events with energy magnitudes of 3 (1 kJ), the event detection zone with P_E over 50% has covered the retreat area, and the highest P_E at 80% was present (see Figure 6-8b). In Figure 6-8c, seismic events with an energy magnitude of 4 can be detected in most of the panel area, but the highest P_E which can be achieved is 90%, still less than the 100% detection probability. It indicates that in LW250105, seismic events with energy magnitudes less than 4 (<10 kJ) cannot be fully detected by the seismic monitoring system. When energy magnitudes increase to 100 kJ ($\log E=5$), a complete event detection probability is observed around geophone #2 (see Figure 6-8d). Also, the retreat area had a relatively higher detection probability with P_E at more than 90%. For the significant seismic events with energy levels larger than 6 (1 MJ), most of them can be fully detected by the monitoring system, as shown in Figure 6-8e, with P_E over 90% in most areas of interest. The P_E results in Figure 6-8 indicate that the zone surrounded by roadway geophones, which is located between 200 m to 400 m ahead of the longwall face, had the highest detection probability for seismic events with all energy levels. In the retreat area, the monitoring system can monitor most of the events with energy magnitudes over 5, but it was insensitive to the events with energy magnitudes less than 4.

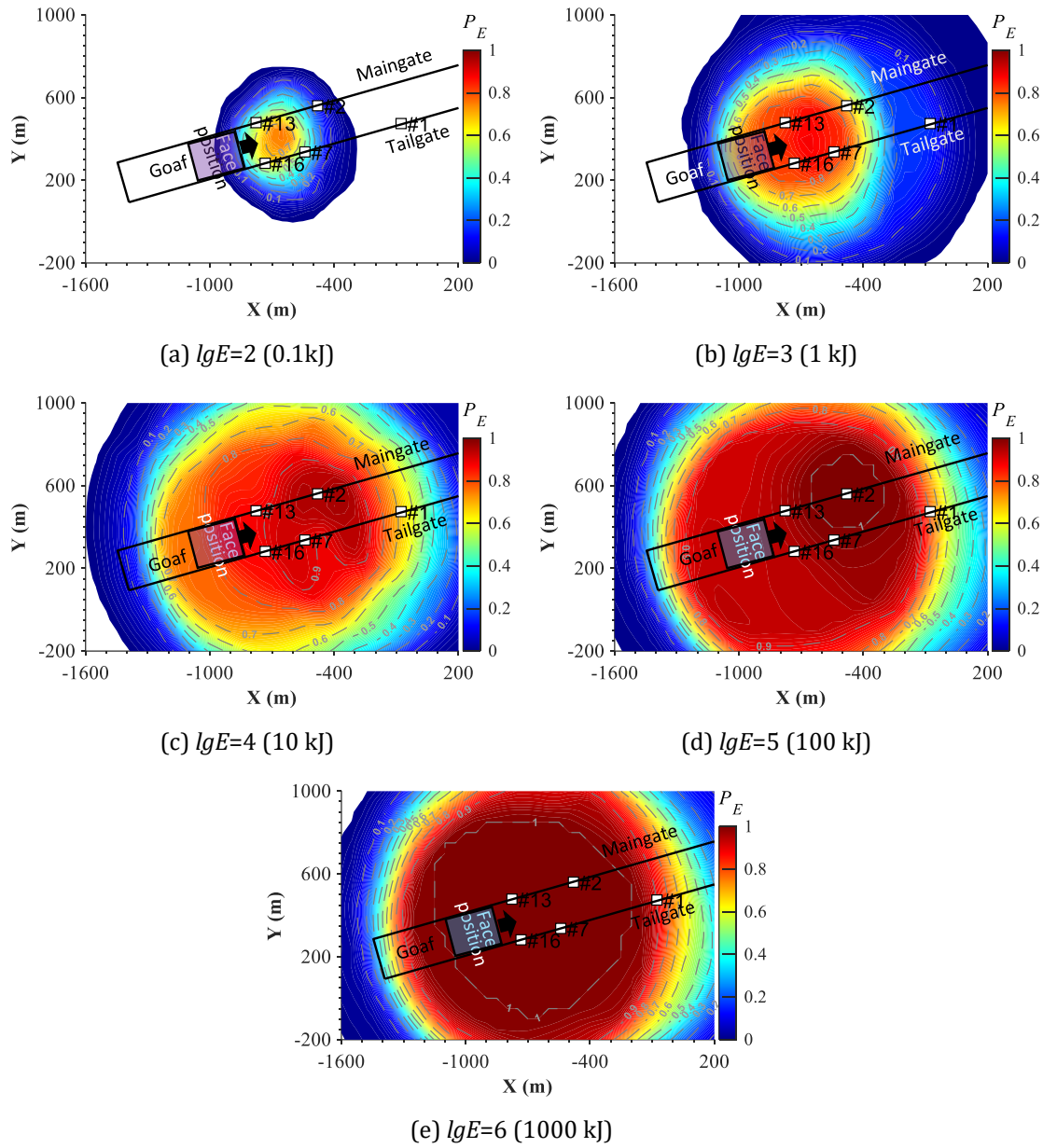


Figure 6-8 Detection probability P_E for seismic events with different energy magnitudes in LW250105. White squares denote active roadway geophones, the shaded zone is the retreat area, and the arrow indicates the mining direction.

The P_E variation of different energy magnitudes of seismic events was also investigated in five specific locations in LW250105, which is shown in Figure 6-9. Compared to other locations, location II at 200–400 m in front of the longwall face had the lowest energy magnitude of 5.3 for a 100% P_E (≈ 200 kJ). It indicates that seismic events are more likely to be detected in the target zone enclosed by

geophones. At location IV, the seismic monitoring system was insensitive to the lower energy events in the goaf, behind the longwall face, where nearly 0% P_E occurred when the energy magnitude was lower than 3 (≈ 1 kJ). The most frequent seismic activities were recorded in locations I, III and V during the panel retreating. Within these zones, the monitoring system had P_E at nearly 60% for the seismic events with energy magnitudes of 2–3 (0.1~1 kJ), and it increased to more than 80% when energy magnitudes approached 4 (10 kJ). Results in Figure 6-9 suggest that seismic events with energy magnitudes over 4 are more likely to be detected. Thus the number of recorded events is closer to the actual number of mining-induced seismicity. However, the detection probability would decrease rapidly if the energy magnitudes of the seismic events were lower than 4.

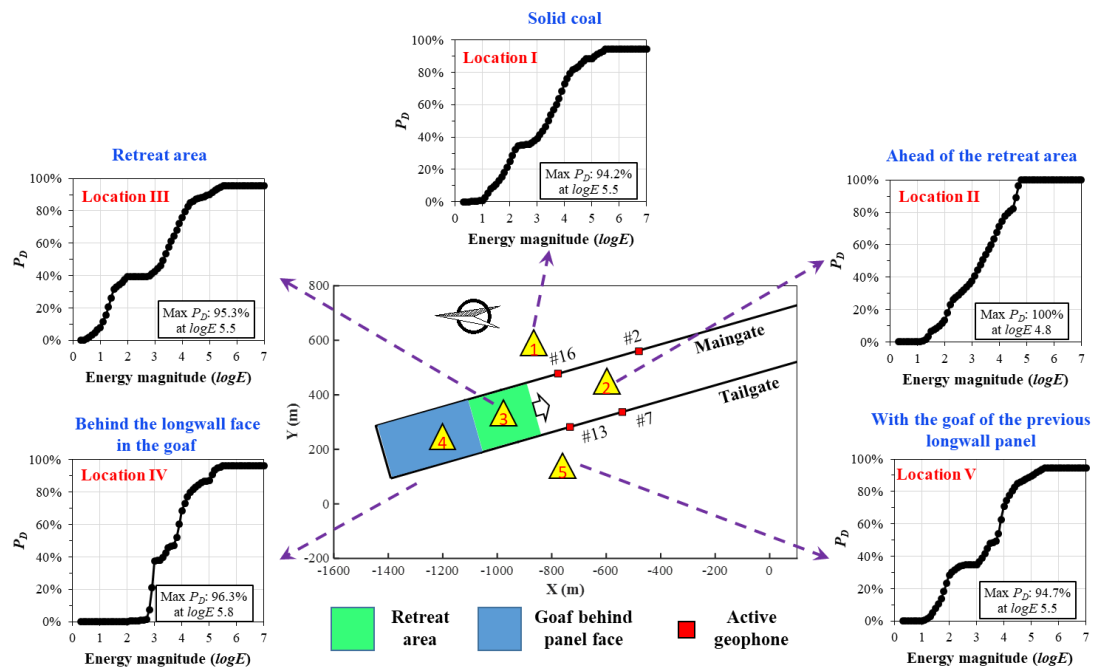


Figure 6-9 Event detection probability in LW250105 at specific locations of (I) solid coal, (II) ahead of the retreat area, (III) retreat area, (IV) behind the longwall face in the goaf, and (V) with the goaf of the previous longwall panel

6.3.3 Energy magnitude distribution at different event detection probabilities

As illustrated in Section 6.2.2, if the P_E of all energy magnitudes is calculated, the spatial distributions of energy magnitudes at different P_E thresholds can be derived. Figure 6-10 shows the energy magnitude distributions in LW250105 at P_E thresholds of 100%, 95% and 90%. Similar to m_c , $P_{E(1.00)}$ in Figure 6-10a can represent the complete event detection characteristics in the study panel. However, this figure indicates that the magnitude of completeness is a function of spatial location rather than a constant value. The complete event detection zone has covered the chainage zone and the zone within 700 m in front of the longwall face, where the energy magnitudes ranged from 4.8 to 6.2. The area around roadway geophone #2 has the best seismic data integrity where the minimum energy magnitude for detection was 4.8. Distributions of energy magnitudes with lower P_E thresholds ($P_{E(0.95)}$ and $P_{E(0.90)}$) shown in Figure 6-10b and 13c can also provide insight into the event detection characteristics of the seismic monitoring system. The detection zone expanded to the goaf zones of the panel, where the minimum energy magnitude for detection was about 4.7 (≈ 50 kJ). This pattern of the energy magnitude distribution is caused by using the distant geophone #11 on the west side of the panel (see Figure 3-3). However, zones with better detection capabilities were consistently around roadway geophones, where the minimum energy magnitude was lower than 5.1. Figure 6-10 demonstrates that the magnitude of completeness, or the energy magnitude with high event detection probabilities, varies in space and depends on the layout of geophones.

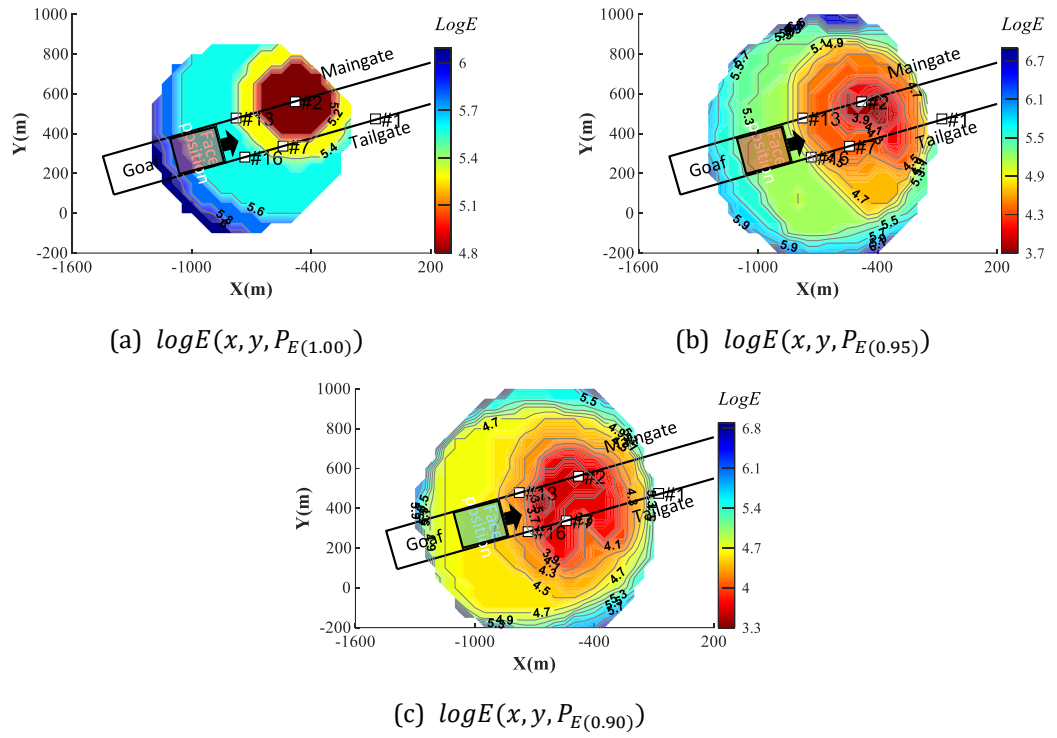


Figure 6-10 Distribution of energy magnitudes with P_E thresholds of 100%, 95% and 90%. White squares denote the active roadway geophones, the shaded zone is the chainage zone, and the arrow indicates the mining direction.

To compare the magnitude of completeness results of the PDE method and conventional m_c methods, the maximum curvature method was used to calculate m_c in LW250105. Figure 6-11 shows the determined m_c based on the FMD and cumulative FMD of the seismic events from 1 July to 29 September 2014. Similar to the earthquake catalogue in volcanic areas as reported by Wiemer and Wyss (2000), a bimodal FMD distribution of seismic events was observed in LW250105, with two peak event counts values of 23 at $\log E$ of 4.24 and 4.48. This uncertainty of m_c may have negative impacts on seismic analysis: overestimating m_c could reduce the amount of available data while underestimating may cause false results (Schorlemmer and Woessner, 2008). $\log E$ of 4.48 was adopted as a conservative estimation of m_c , which is still lower than the minimum energy magnitude for detection determined by the PDE method, 4.8 (see Figure 6-10a). This finding

indicates that the conventional m_c methods may overestimate the event detection capability of the seismic monitoring system.

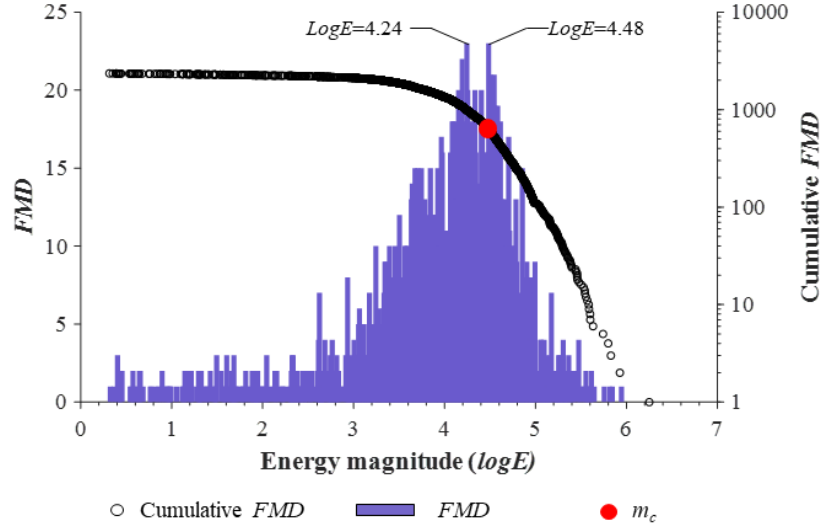


Figure 6-11 *FMD* and cumulative *FMD* of seismic events in LW250105 from 1 July to 29 September 2014. Energy magnitude of completeness (m_c), marked by a red dot, is calculated using the maximum curvature method.

6.4 Discussion

In this section, the seismicity correcting method proposed in Section 6.2.3 is first used to supplement potential undetected seismic events over the monitoring period in LW250105. Then, the procedure to determine a critical parameter for P_D calculation, the minimum number of sample events of a grid (N_{min}), is demonstrated. Finally, the limits of the *PDE* method on rock mass heterogeneity and the deficiency of applying uniaxial seismic data in the proposed method are explicitly discussed.

6.4.1 Seismic data correction in LW250105

The corrected seismic data in LW250105 was calculated and compared in terms of event counts and seismic energy. For comparison purposes, the m_c determined in Figure 6-11 was also tested to improve seismic data reliability by discarding

seismic events with energy magnitudes of smaller than 4.48. Figure 6-12a, b and c show the seismic event density distributions in LW250105 during September 2014 based on the original data, the corrected data, and the data filtered after applying $m_c=4.48$, referred to as the data over m_c , respectively. Compared with the original seismic data (Figure 6-12a), the corrected data had more than twice the density of the events, which provided more detail on their spatial distribution (Figure 6-12b). The corrected data compensated for the poor detection capability of the seismic monitoring system in the goaf behind the retreat area, which had a higher degree of events concentration. Such an event concentration is due to the tensile failure from the roof breakage and caving process in the goaf zone, where medium-low energy magnitude was released. Also, along the tailgate side ahead of the longwall face, shown in Figure 6-12b, more seismic events were detected in a larger area than Figure 6-12a. This result reveals that more seismic activities might have occurred around the tailgate, where more frequent coal burst incidents and higher seismic energy releases were reported. In contrast, the data over m_c shows a much lower density of seismic events in a smaller area around the chainage zone (Figure 6-12c). A concentration of seismic events in the goaf behind the retreat area is evident in this figure; however, ahead of the longwall face, the information is limited.

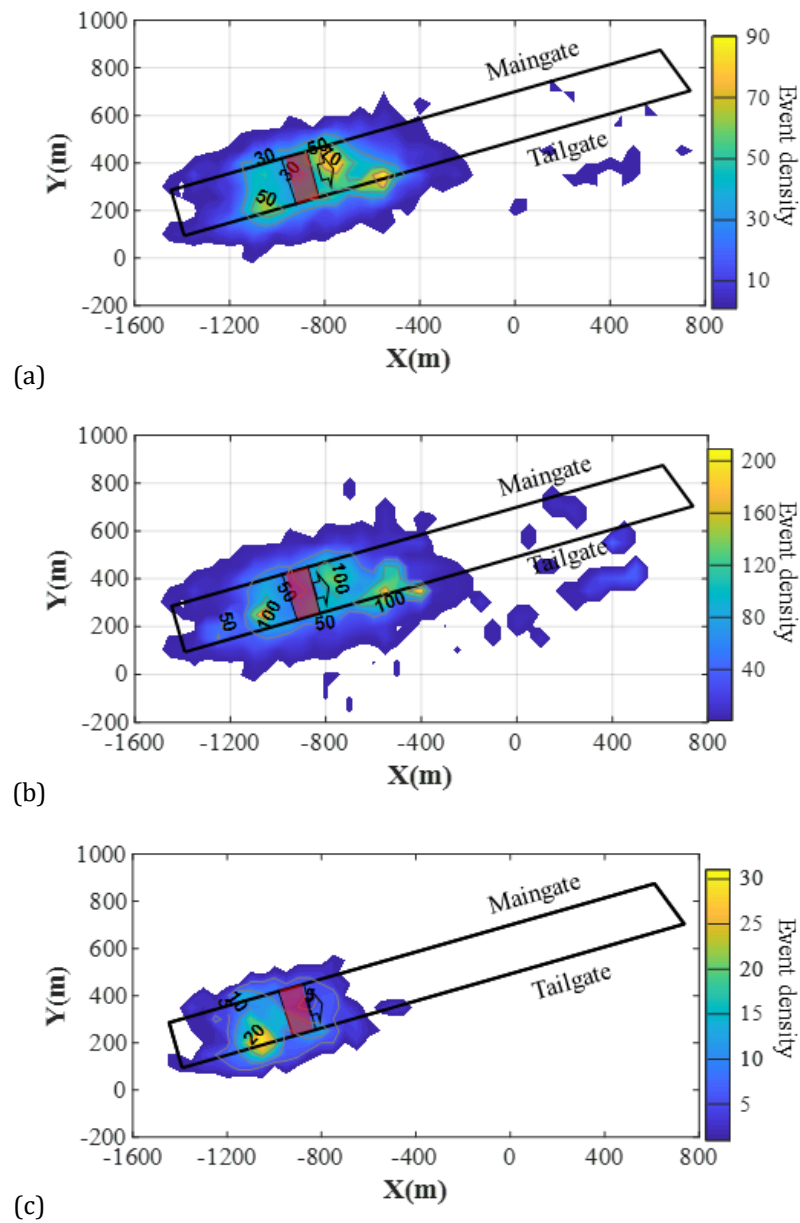


Figure 6-12 Spatial distribution of seismic events in LW250105 during September 2014 based on (a) original data, (b) data after correction, and (c) data over m_c . Shaded area indicates the chainage zone, and the arrow indicates the mining direction.

As indicated in Figure 6-10, due to the layout of roadway geophones, the seismic monitoring system is insensitive to the seismic events with lower energy magnitudes in the zone near the longwall face. Therefore, it is necessary to explore if the proposed *PDE*-based seismicity correcting method can retrieve undetected seismic events near the longwall face. Figure 6-13a compares the average daily event

counts ahead of the LW250105 face in September 2014 based on the original data, the data over m_c and the corrected data after applying the *PDE* method. Both the original data and the corrected data indicated intensive seismic activities within 400 m ahead of the longwall face, with a peak at about 140 m ahead of the longwall face. However, compared with the original data, the corrected data showed a higher counts of seismic events, and a peak of 40 seismic events at about 140 m ahead of the longwall face. It indicates that a large number of seismic events with medium-low energy occurred near the longwall face, where a high stress concentration might exist. The data over m_c shows that few available seismic events were located in front of the longwall face with daily event numbers mostly less than 5, and most of them were within 200 m ahead of the longwall face. Such a limited volume of data shows the limitation of using the conventional m_c method for statistical analyses in mine seismology.

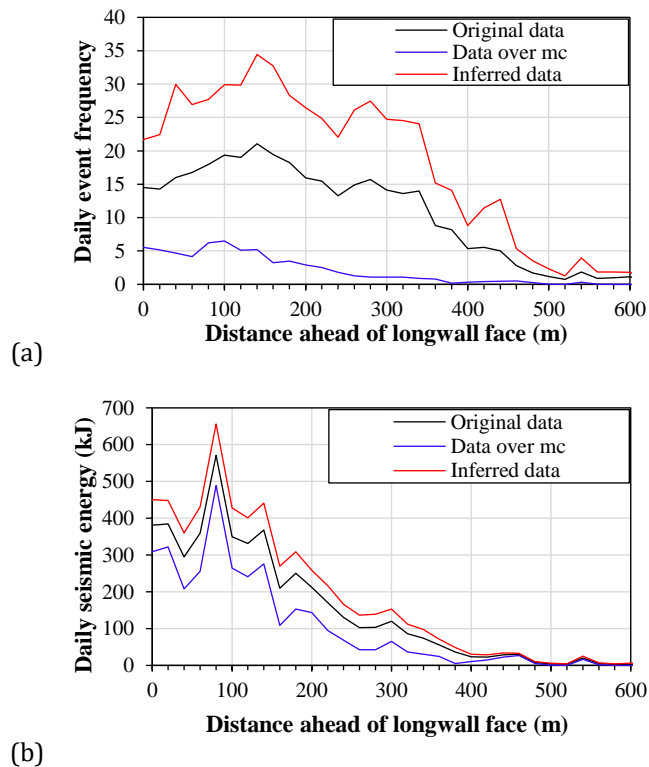


Figure 6-13 (a) Average daily counts and (b) daily seismic energy of seismic events ahead of LW250105 face during September 2014 based on (i) original data (black line), (ii) data over m_c (blue line) and (iii) corrected data (red line).

Figure 6-13b shows the average daily seismic energy in front of the longwall face based on the three different datasets. Most seismic energy was released within 300 m in front of the longwall face. The peak of seismic energy was observed at about 90 m in front of the longwall face for all three cases. Although the three datasets had different energy intensities, they all presented nearly identical trends of seismic energy profiles ahead of the longwall face. This figure indicates that most of the seismic energy was dominated by events with high energy magnitudes. Therefore, the corrected seismic data can provide more information on the number of seismic events at medium-low energy magnitudes. It would present similar seismic energy profiles ahead of the face as using the original data or the data over m_c due to the specific high detection probability of high energy events.

6.4.2 Determination of the minimum number of sample events at a grid point (N_{min})

According to Eq. (6-5), the minimum number of sample events at one grid point, N_{min} , is a key parameter to control the effectiveness of P_D for evaluating the detecting capability of geophones. To calculate the most accurate detection capability for geophones, N_{min} should (1) have enough sample points at each grid to ensure robust P_D results, and (2) improve the effectiveness of P_D calculation by adopting as many grids as possible which have sample events within the searching radius (with the number of N_{T1}). This also means minimising the use of supplementary sample events. To address these two criteria, two indexes were proposed to determine N_{min} : the *Cumulative Grids Number Ratio* (R_C) and the *Sample Events Ratio* (R_T). Assume there are m grid points in the D-M map having sample events within the searching radius ($N_{T1} > 0$), the R_C and R_T values for a geophone are calculated as:

$$R_c = \frac{\sum_{j=1}^m y(j)}{\sum_{j=1}^m z(j)}, \quad y(j) \begin{cases} 1 & N_{T1}(j) \leq N_{min} \\ 0 & N_{T1}(j) > N_{min} \end{cases}, \quad z(j) \begin{cases} 1 & N_{T1}(j) \neq 0 \\ 0 & N_{T1}(j) = 0 \end{cases} \quad (6-12)$$

$$R_T = \frac{\sum_{n=1}^m N_{T1(n)}}{\sum_{n=1}^m N_{min}} \quad (6-13)$$

Figure 6-14 shows the variation of the average R_c (black line) and R_T (red line) from six active geophones in LW250105 with increasing N_{min} from 0 to 50. The R_c trend shows that more than 60% of the grids have N_{T1} less than 6 and only 20% have N_{T1} more than 14, and up to 50 of N_{T1} are in the grid with $R_c = 1$. It implies that a large number of grids are possibly under the influence of sparse seismic data, and it is hard to provide robust P_D results by using the few sample events within the searching radius only. The R_T trend shows a decreasing proportion of using sample events within the searching radius along with the increase of N_{min} . About 80% of R_T is present when N_{min} is 6, and R_T is less than 50% when N_{min} is more than 16. It indicates that a higher N_{min} will adopt more supplementary sample events and dummy events for P_D calculation, which may reduce the effectiveness of the P_D results. To ensure both the robustness and effectiveness of the P_D results, $N_{min}=9$ at the crossing point of the R_c and R_T curves in Figure 6-14 is determined as the optimal value in this study, where 72% of R_c and 71% of R_T are present.

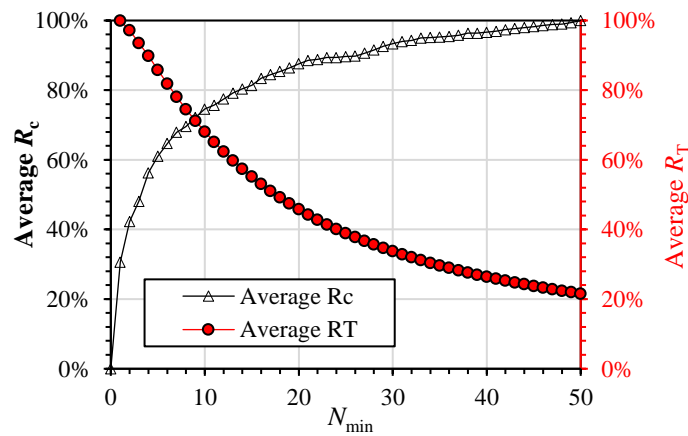


Figure 6-14 Average Cumulative Grids Number Ratio R_c (black line) and Sample Events Ratio R_T (red line) of the six active geophones in LW250105

6.5 Detection probability evolution of the seismic monitoring system in LW250105

Section 6.3 investigated detection probability characteristics of the seismic monitoring system in LW250105 with a fixed geophone layout during July to August 2014. However, the distribution of geophones was regularly modified along with the panel retreat during 2014 (see Figure 3-4). Once the location of a geophone has been modified, the *PDE* method requires a recalibration of the P_D result for a geophone by discarding all its past seismic data. Such a recalculation on P_D results will affect the assessment of detection probability of the seismic monitoring system (P_E), which may reduce the robustness of the assessment results. Therefore, this section conducts weekly P_D and P_E assessments in LW250105 from April to December 2014 to investigate the varying characteristics of the detection probabilities when new seismic data are supplemented and geophones are relocated.

Figure 6-15 shows the evolution of P_D results for geophone #7 in the first six weeks. In Figure 6-15a, only one week of seismic data was used for P_D calculation, and the geophone is only capable of capturing seismic events with $\log E > 5$ and hypocentral distance less than 200 m. Such a poor result of detection capability cannot represent the actual detection capability of the geophone as insufficient seismic data were used. With the second week's seismic data being added for P_D calculation, the result in Figure 6-15b shows a much higher detection capability for the seismic events with medium-low energy and/or long hypocentral distance. From the third week, similar P_D results are obtained, which shows that geophone #7 has a large detection range covering seismic events with $\log E$ from 2 to 7 and hypocentral distances from 0 to 800 m (see Figure 6-15c-f). It indicates that after relocating a geophone, it requires at least three weeks' collection of seismic data to obtain robust P_D results.

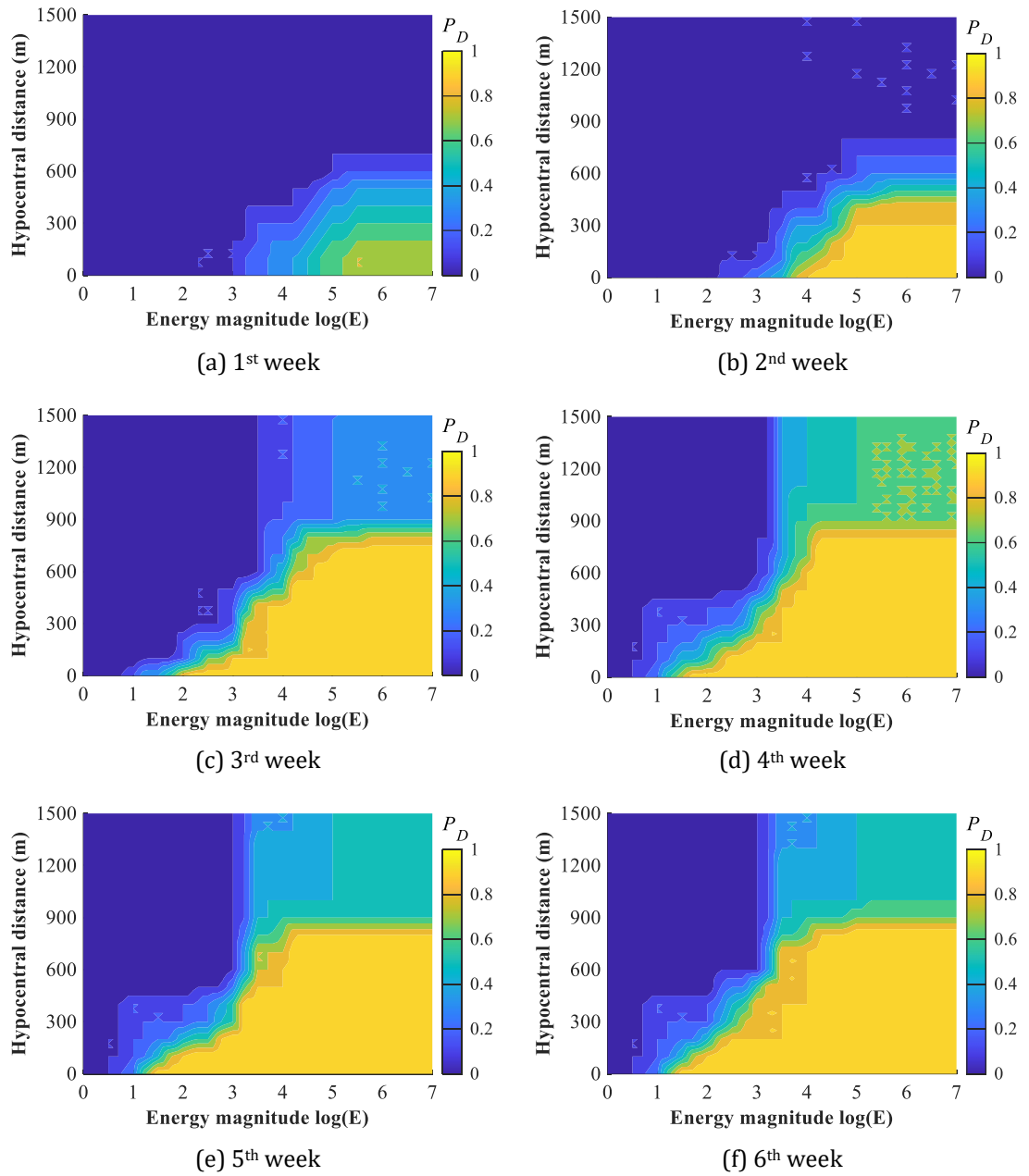


Figure 6-15 Recalculation of P_D results for geophone #7 after its relocation in LW250105 from 7 April to 12 May 2014

Once a geophone is moved to a new location, its P_D recalculation may affect the P_E distribution in the area of interest. Figure 6-16 and Figure 6-17 are two examples showing the difference of P_E results for the seismic events with $\log E=5$ before and after the relocation of geophones. In Figure 6-16, the movement of geophone #2 reduces the overall detection probabilities for seismic events. However, in

Figure 6-17, slight variations in detection probabilities can be observed after moving geophone #16 in July 2014. It demonstrates that the relocation of geophones can lead to different P_E results.

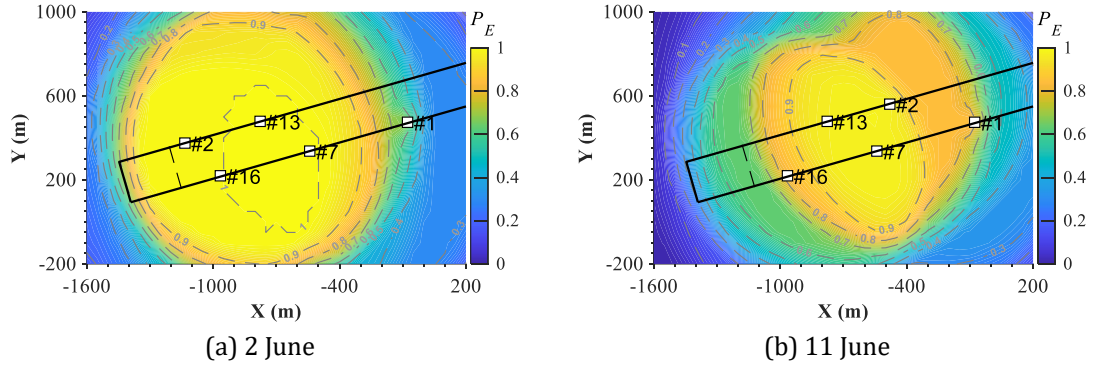


Figure 6-16 P_E distribution in LW250105 during 2014 for the seismic events with $\log E=5$ before (a) and after (b) the relocation of geophone #2

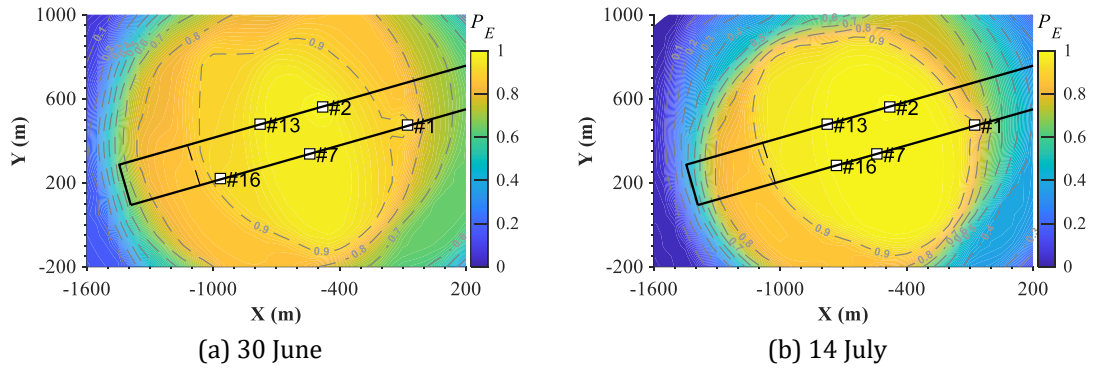


Figure 6-17 P_E distribution in LW250105 during 2014 for the seismic events with $\log E=5$ before (a) and after (b) the relocation of geophone #13 and geophone #16

To quantify the differences in P_E results in LW250105 during different periods, the cosine similarity method is used to calculate their similarity. This method calculates the cosine of the angle between two arrays. The smaller the angle, the higher the similarity between two arrays. The cosine of the angle between the arrays \vec{A} and \vec{B} is calculated as:

$$\cos \theta = \frac{\vec{A} \cdot \vec{B}}{\|\vec{A}\| \|\vec{B}\|} = \frac{\sum_{i=1}^n A_i B_i}{\sqrt{\sum_{i=1}^n A_i^2} \sqrt{\sum_{i=1}^n B_i^2}} \quad (6-14)$$

where n is the length of the arrays. In this study, to investigate the effect of supplementing new seismic data and/or relocating geophones on the P_E distributions, the cosine similarity of each P_E result is calculated by comparing the latest P_E result with the one before relocating geophones. It is further explained by Figure 6-18, which shows the similarity of P_E distributions in LW250105 over the monitoring periods. The red dots are the last P_E results before relocating geophones and the cosine similarity is 1. For example, in this figure, the cosine similarities of the P_E results from 12 April to 26 May 2014 are calculated by using the P_E distribution on 2 June 2014, which is the last P_E result before the relocation of geophone #2 on 5 June 2014. Figure 6-18 indicates that P_E similarity increases rapidly from 0.35 to more than 0.80 within the first three weeks from 12 to 28 April 2014. It indicates that a robust P_E calculation in LW250105 needs at least three weeks for sufficient seismic data collection. After the first three weeks, all P_E results have similarity values that are no less than 0.9 before geophone movement. It verifies the robustness of P_E results in assessing the detection probability of the seismic monitoring system in LW250105, regardless of the relocation of geophones.

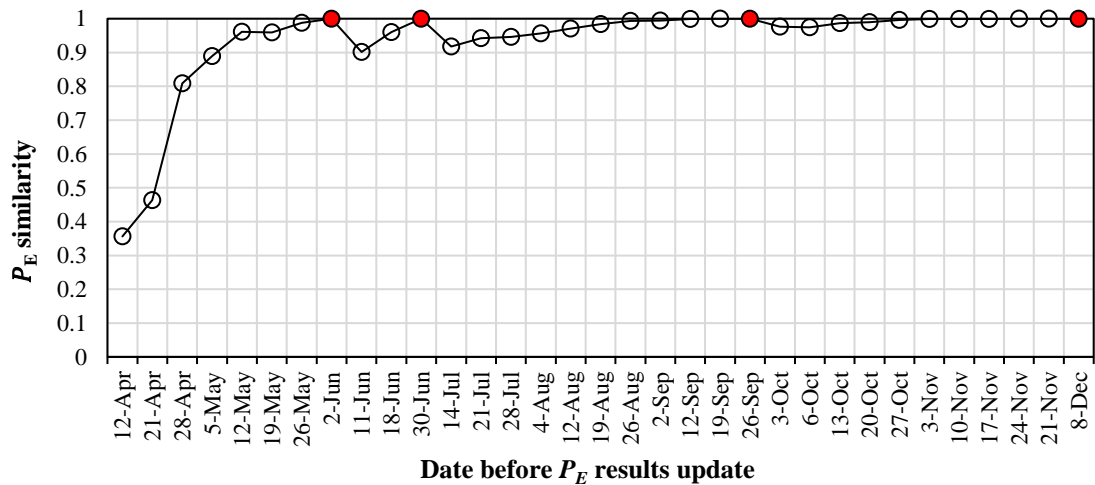


Figure 6-18 Similarity of P_E results for the seismic monitoring system in LW250105 for 12 April to 8 December 2014. Red dots are the last P_E result before the relocation of geophones.

6.6 Summary

This chapter investigated the characteristics of seismic data integrity by analysing the detection probability of the seismic monitoring system implemented in LW250105. A novel method called *PDE* analysis was proposed to evaluate the detection capabilities of individual geophones and the overall seismic monitoring system in the studied mine. Geophones installed at the longwall have various detection capabilities to seismic events with different hypocentral distances and energy magnitudes. Roadway geophones close to the longwall face were more capable of capturing low energy seismic events than the distant geophones that were far from the longwall. The seismic monitoring system showed a better detection capability for the events with higher energy magnitudes, and the highest detection probability zone was located in the zone around active geophones. Based on the detection probability results, a data compensating method was proposed to infer all possible seismic activities. Compared to the original monitoring data, the corrected data had up to twice the event counts, and showed more intensive energy release might have occurred in front of the longwall face.

The *PDE* method has been proven feasible to assess seismic data integrity in underground mines, which can improve the accuracy and effectiveness of seismic monitoring. Other seismic analysis methods using the corrected seismic data can be developed in the future to enhance system performance. However, although the seismic monitoring system is regularly calibrated, the highly heterogeneous environment in mines still causes difficulties to detect seismic events due to the complex velocity field and the reflection and refraction of seismic waves. Therefore, more research is required to understand the influence of rock heterogeneity on the detection capabilities of a seismic monitoring system. Also, the seismic monitoring system using uniaxial geophones in the test mine limited the accuracy in calculating seismic energy, which would affect the detection probability results presented in this

chapter. Therefore, further studies should focus on using more accurate triaxial seismic data to assess the detection probabilities of seismic events in three dimensions. In Chapter 7, based on the results of location errors and detection probability of the seismic monitoring system, the seismic data in LW250105 is further corrected and used in analysing spatial variation of seismicity to assess coal burst risks.

Chapter 7. Spatial variation of seismicity using reinforced seismic data and its application in coal burst prediction

7.1 Introduction

The analysis on the spatial variations of event counts and seismic energy, referred to as “spatial variations of seismicity”, is the most popular method that has been used to assess burst risks in underground mines. Compared with other seismic methods, the spatial variation of seismicity analysis is a simple procedure to implement which only uses basic seismic parameters, such as onset time, location and energy of seismic sources. However, its accuracy in assessing burst risks is limited by the poor seismic data quality due to low location accuracy and poor data integrity.

Therefore, based on the investigations in Chapter 5 and Chapter 6, this chapter proposes a new seismic analysis method to enhance the performance of applying the spatial variation of seismicity to assess coal burst risks. In the new method, a modified *NPCE* analysis is proposed to determine a potential damage zone (*PDZ*), where seismic events are related to the impending burst damage. The concept of ‘reinforced seismic data’ is proposed, which corrects the location errors and improves the detection probabilities of raw seismic data within the *PDZ*. Using the reinforced seismic data, seismic event counts and seismic energy released on a daily basis were calculated to investigate their correlation with coal burst damage in LW250105.

7.2 Methodology

7.2.1 Potential damage zone (PDZ)

For the spatial variation of seismicity, its hazard precursor only works when using the seismic events that are intrinsically related to mining-induced rock damage. It means that the volume of damaged rock needs to be identified prior to the analysis of variations of seismicity (Brady, 1974). Seismic events that are outside the volume of the damaged rock may reduce the result accuracy and make the precursors of impending bursts become inconspicuous. Therefore, it is essential to first identify the potential damage zones which clustered seismic events are associated with.

The $NPCE$ analysis proposed in Chapter 5 is used to identify potential damage zones. According to the R_{NPCE} results of LW250105 in Figure 5-8, three long-term high R_{NPCE} zones were observed from 100 m to more than 300 m away from the longwall face, where a large number of coal bursts occurred. Such high degrees of seismic clusters are attributed to the seismic response of undetected geological structures to mining activities. However, due to the complicated stress loading paths and limited seismic monitoring capabilities in the study mine, a medium-low R_{NPCE} can be present in these long-term high R_{NPCE} zones when the longwall face is approaching, which leads to false results for identifying coal burst hazards. For example, the high R_{NPCE} zone 2 in Figure 5-8 had significant seismic clustering from July to September 2014. But after October 2014, the high R_{NPCE} zone 2 only had a medium-low R_{NPCE} , where a coal burst occurred on 11 October 2014 with the maximum R_{NPCE} of 0.4. Therefore, to enhance the effectiveness of identifying potential damage zones, it is essential to record the highest historical R_{NPCE} value

at each grid in the area of interest. Assuming m times of $NPCE$ analyses have been conducted, among all results for the m^{th} R_{NPCE} , the maximum R_{NPCE} at grid i is:

$$\max R_{NPCE}^m(i) = \max (R_{NPCE}^1(i), R_{NPCE}^2(i), \dots, R_{NPCE}^m(i)) \quad (7-1)$$

Figure 7-1 shows the R_{NPCE} and $\max R_{NPCE}$ results in LW250105 for 28 May to 3 June 2014. The R_{NPCE} result shows that R_{NPCE} zones larger than 0.8 are located within 100 m ahead of the longwall face on the tailgate side (see Figure 7-1a). Compared to the R_{NPCE} result, the $\max R_{NPCE}$ result shows an extended high R_{NPCE} zone (>0.8) within about 200 m ahead of the longwall face (see Figure 7-1b). It indicates that more zones have experienced intensive seismic activities, where the coal and rock mass can be highly unstable. Coal bursts in these high R_{NPCE} zones are more likely to be triggered by the mining disturbance as the longwall face approaches.

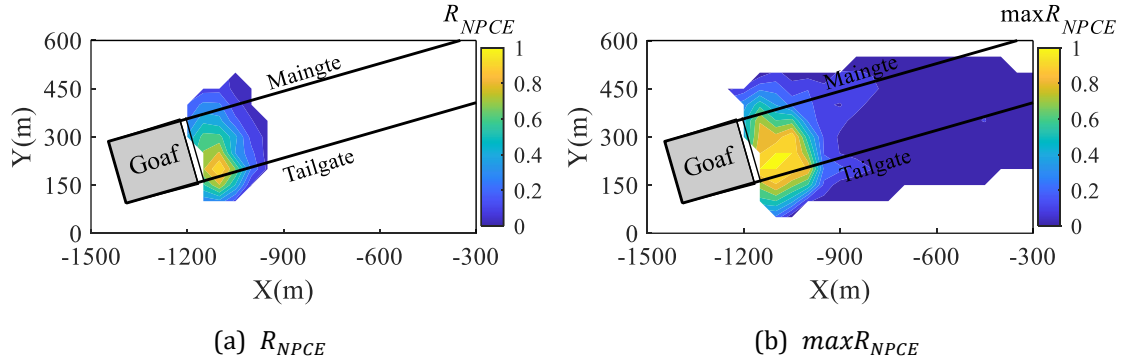


Figure 7-1 (a) R_{NPCE} and (b) $\max R_{NPCE}$ results in LW250105 for 28 May to 3 June 2014. The grey zone is the goaf behind the longwall face.

Based on the $\max R_{NPCE}$ result in the longwall, the potential damage zone (PDZ) is first identified if the $\max R_{NPCE}$ per grid is higher than a certain threshold. Then within the identified PDZ , the spatial variations of seismicity will be further analysed to investigate coal burst precursors. The PDZ threshold is an empirical parameter indicating the overall burst propensity of the longwall, which is related to the mine layout, background seismicity, material properties and mining speed. Since there is

no reference for the determination of $maxR_{NPCE}$, $maxR_{NPCE}=0.5$ was set as the threshold for PDZ identification. It should be noted that the optimal $maxR_{NPCE}$ threshold for PDZ may vary among different mining and geological conditions, which can be determined by back analysing historical coal burst damage.

Figure 7-2 shows the example of the R_{NPCE} and $maxR_{NPCE}$ distributions in LW250105 for 5–11 November 2014. To compare the two results, PDZ is also identified using the R_{NPCE} result with the same threshold of 0.5 (see Figure 7-2a). Similar to Figure 7-1a, the R_{NPCE} distribution in Figure 7-2a also shows fewer zones with significant $R_{NPCE}>0.5$. The impending coal burst which occurred on 16 November 2014 is located outside of the identified PDZ , where R_{NPCE} is only 0.4. Different from R_{NPCE} , the $maxR_{NPCE}$ distribution in Figure 7-2b shows that a much larger zone has been detected with $maxR_{NPCE}>0.5$. These high $maxR_{NPCE}$ grids have covered the area about 300 m ahead of the longwall face on the tailgate side. The impending coal burst is located in the identified PDZ , where the $maxR_{NPCE}$ is also larger than 0.9. It suggests that $maxR_{NPCE}$ has a higher accuracy in assessing coal burst risks than R_{NPCE} as it covers the impending burst damage area.

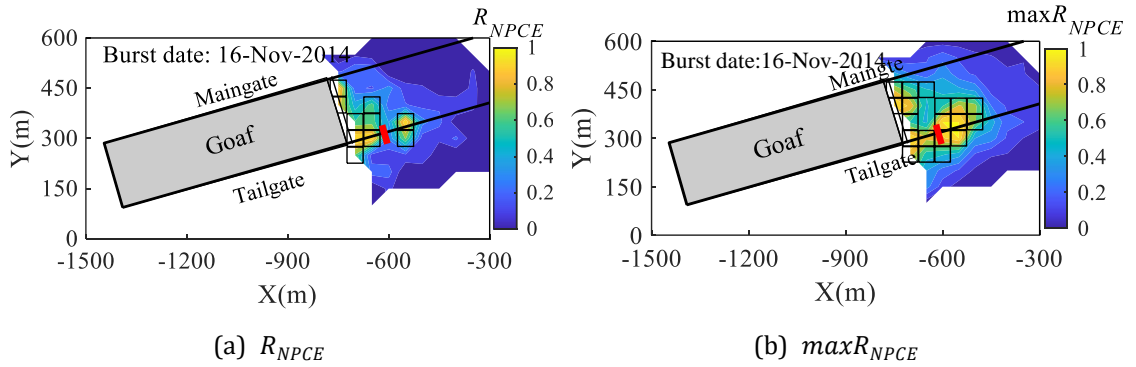


Figure 7-2 PDZ identification in LW250105 for 5–11 November using the (a) R_{NPCE} results and (b) $maxR_{NPCE}$ results. The red zone indicates a roadway section damaged by an impending coal burst which occurred in the following week (16 November 2014). Black rectangles outline the identified PDZ . The grey zone is the goaf.

7.2.2 Reinforced seismic data

Based on the identified *PDZ* in Section 7.2.1, the spatial variation of seismicity can be further analysed to investigate its relationship with coal burst hazards. As illustrated in Chapter 5 and Chapter 6, significant location errors and poor detection capabilities of the seismic monitoring system are the two main factors that limit the performance of seismic analyses in assessing coal burst risks. To improve accuracy and effectiveness in the identified *PDZ*, the concept of ‘reinforced seismic data’ is proposed. It describes the reprocessed seismic data by eliminating the defects of poor locating accuracy and improving the seismic data integrity in the area of interest. Assuming n seismic events are monitored during a study period, their corresponding detection probabilities are $P_E(x_1, y_1, \log E_1)$, $P_E(x_2, y_2, \log E_2)$, $P_E(x_n, y_n, \log E_n)$ (see Section 6.3.2). For a *PDZ* grid i , the probabilities of these n seismic events being located in the grid are $\eta_{1(i)}$, $\eta_{2(i)}$, $\eta_{n(i)}$. The possible number of events at the *PDZ* grid i , i.e. event counts, is calculated as:

$$m_{reinf(i)} = \sum_{j=1}^n \eta_{j(i)} / P_E(x_j, y_j, \log E_j) \quad (7-2)$$

The possible seismic energy released at the grid i is calculated as:

$$E_{reinf(i)} = \sum_{j=1}^n E_j \cdot \eta_{j(i)} / P_E(x_j, y_j, \log E_j) \quad (7-3)$$

Similar to *NHGM* proposed in Section 4.4.1 and *NPCE* proposed in Section 5.3.2, m_{reinf} and E_{reinf} are also seismic related parameters, which may be affected by the active degree of seismic events. The variations of geological and mining conditions during different periods may cause a significant difference in the active degree of seismic events, which usually leads to bias in seismic parameters. Therefore, to evaluate coal burst risks, normalisations of m_{reinf} and E_{reinf} are

also required. Assuming a *PDZ* grid i in the area of interest, its normalised m_{reinf} and E_{reinf} , represented by $Rm_{reinf(i)}$ and $RE_{reinf(i)}$, respectively, are calculated as:

$$Rm_{reinf(i)} = \frac{m_{reinf(i)}}{m_{reinf(max)}} \quad (7-4)$$

$$RE_{reinf(i)} = \frac{E_{reinf(i)}}{E_{reinf(max)}} \quad (7-5)$$

where $m_{reinf(max)}$ and $E_{reinf(max)}$ are the maximum event counts and seismic energy at all *PDZ* grids in the study period, respectively.

Figure 7-3 and Figure 7-4 are two examples showing the improvement from using reinforced seismic data to forecast impending coal burst hazards. For comparison purposes, the normalised event counts and seismic energy using raw seismic data are referred to as Rm_{raw} and RE_{raw} , respectively. Figure 7-3 shows similar degrees of event counts in the impending coal burst zones between Rm_{reinf} and Rm_{raw} , with values of 0.6. However, the Rm_{reinf} result identifies a 50 m long zone in the tailgate as the high burst risk zone with $Rm_{reinf} > 0.6$ (see Figure 7-3a), while the Rm_{raw} result presents a nearly 100 m long zone in the tailgate having burst damage potential $Rm_{raw} > 0.6$ (see Figure 7-3b). It indicates that compared with raw seismic data, using the reinforced seismic data narrows down the range of an evaluated burst risk zone, which enhances the efficiency (precision) in coal burst forecasting.

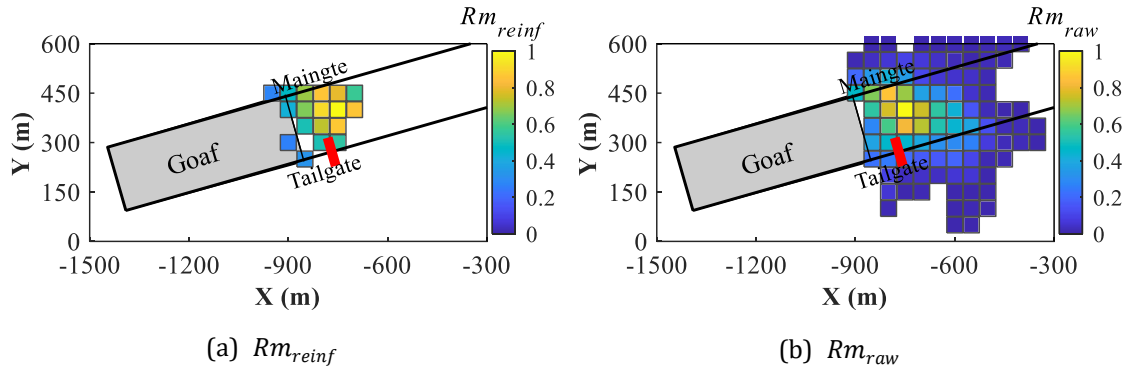


Figure 7-3 Event count distributions in LW250105 on 21 September 2014 using reinforced seismic data (Rm_{reinf}) (a) and raw seismic data (Rm_{raw}) (b). The red zone is the roadway section damaged by an impending coal burst which occurred in the following week. The grey zone is the goaf.

Figure 7-4 shows the seismic energy distributions in LW250105 on 11 September 2014 using reinforced seismic data and raw seismic data. The impending coal burst on 12 September 2014 occurred at the inbye of the tailgate corner. The RE_{reinf} result shows that the burst damage zone is located in the high RE_{reinf} grids with values larger than 0.9 (Figure 7-4a). However, only 0.3 of RE_{raw} is present in the burst damage zone when raw seismic data are used (Figure 7-4b). It indicates that analysis on the spatial variations of seismicity using reinforced seismic data can provide more accurate results in assessing coal burst risks than using raw seismic data.

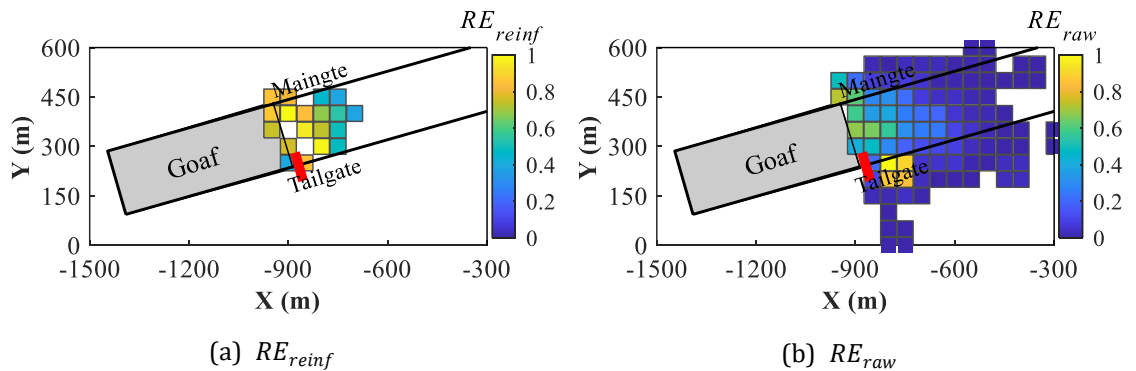


Figure 7-4 Seismic energy distributions in LW250105 on 11 September 2014 using reinforced seismic data (RE_{reinf}) (a) and raw seismic data (RE_{raw}) (b). The red zone is the roadway section damaged by an impending coal burst which occurred on 12 September 2014. The grey zone is the goaf.

7.3 Spatial variation of seismicity in LW250105 using reinforced seismic data

Based on the location error assessment results in Chapter 5 and the P_E results in Chapter 6, the reinforced seismic data for April to December 2014 in LW250105 are calculated, and the spatial variation of seismicity on the day before the occurrence of a coal burst is used to analyse its accuracy and efficiency in assessing coal burst hazards.

7.3.1 *PDZ* identification in LW250105

As introduced in Section 3.3, reliable seismic monitoring in LW250105 commenced in April 2014 and the geophone layout was modified on 4 April 2014. Therefore, weekly *PDZ* identification was conducted from 4 April to periodically assess coal burst risks in the panel. The coal burst event which occurred on 8 April was not included in the analysis since less than one week of seismic data was collected before the coal burst onset, which is insufficient for *PDZ* calculation. Similar to the R_{NPCE} method in Section 5.4, the accuracy of hazard prediction for *PDZ* is defined as the number of coal burst incidents that are reported in the identified *PDZ*. Figure 7-5 shows the damage zones of 23 coal bursts and the latest *PDZ* results (before burst occurrence) in the tailgate ahead of the longwall face. It implies that 16 coal bursts were located in the *PDZ*, which constitutes 70% of the total (16 of 23). Similar to the R_{NPCE} results in Figure 5-8, *PDZ* results also failed to detect the damaged areas caused by coal bursts on 13 April, 16 September and 13 December 2014, where almost no seismic events were recorded nearby. It indicates that seismic analyses cannot be used in areas with low seismic activities (or very few event counts). Therefore, by only considering the coal bursts located in the seismically active areas, the accuracy of *PDZ* in forecasting coal bursts can be up to 80% (16 of 20). Such hazard prediction accuracy is higher than that of R_{NPCE} with

the same index threshold of 0.5, which shows 75% accuracy in coal burst hazard prediction (see Figure 5-11). It demonstrates that adopting maximum R_{NPCE} in the proposed PDZ identification can further enhance the performance of R_{NPCE} analysis for weekly hazard risk assessment.

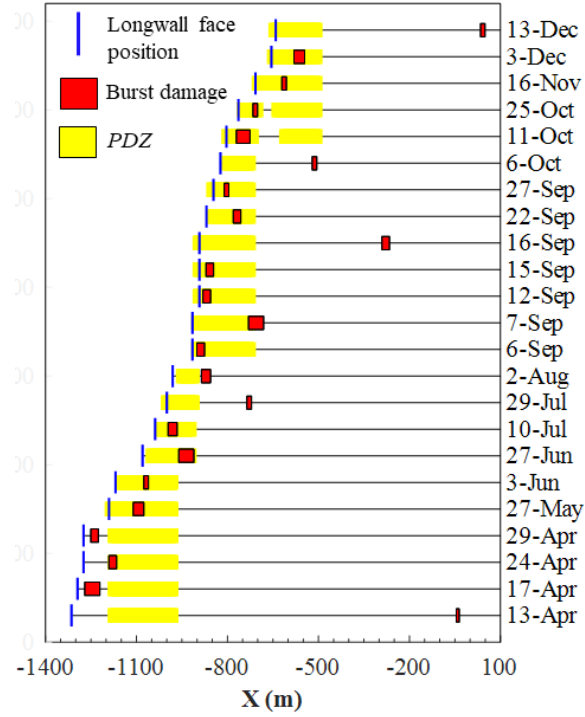


Figure 7-5 Coal burst damage zones and the latest PDZ in the tailgate ahead of the longwall face in LW250105. The red zone is the coal burst damage zone. The blue line is the longwall face position. The yellow zone is the PDZ calculated per production date.

In field applications, the hazard prediction efficiency (precision) is also an important factor to evaluate the performance of seismic analysis. Here, a simple equation is introduced to assess the hazard prediction efficiency for a given seismic index. Assume a given burst risk threshold k for a seismic index, its efficiency η_k is calculated as the ratio of the burst damage length $L_{damage(k)}$ to the total length of high-risk zone L_k identified by the seismic index:

$$\eta_k = \frac{L_{damage(k)}}{L_k} \quad (7-6)$$

It should be noted that the burst damage length outside the identified high-risk zone will not be included in $L_{damage(k)}$. As 0.5 is set as the threshold for PDZ identification, $k=0.5$ is used to assess the hazard prediction efficiency for PDZ . Figure 7-6 shows the hazard prediction efficiency results for the 16 coal bursts located in the PDZ in LW250105, which range from 0.02 to 0.27. The average hazard prediction efficiency of PDZ is about 11%, which is lower than that of R_{NPCE} , reported at 15% with the threshold $k=0.5$ (see Figure 5-11). A k threshold larger than 0.5 will lead to a higher accuracy but lower efficiency of PDZ in predicting burst hazard. Inversely, a k threshold lower than 0.5 will lead to a lower accuracy but higher efficiency for hazard prediction. Since only the spatial hazard prediction is conducted in the study, the false positive of the PDZ results is equal to one minus the accuracy. Although PDZ has higher accuracy in predicting coal burst hazards, such a low prediction efficiency does not meet the requirement for field applications as the cost and time would be unfavourable. Therefore, it is necessary to further improve the hazard prediction efficiency based on the PDZ results.

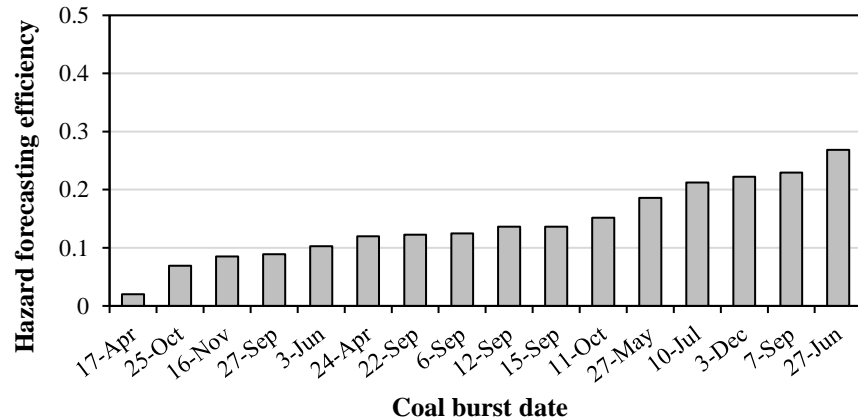


Figure 7-6 Efficiency of coal burst prediction using PDZ identification (with $k=0.5$) in LW250105

7.3.2 Results of spatial variation of seismicity using reinforced seismic data

Within the identified *PDZ*, the normalised event counts and seismic energy using reinforced seismic data, represented by Rm_{reinf} and RE_{reinf} respectively, were calculated on a daily basis in LW250105. The latest Rm_{reinf} and RE_{reinf} results were calculated before the occurrence of the 16 coal bursts located in the *PDZ*. To compare the difference between using reinforced seismic data and raw seismic data, the normalised event counts and seismic energy using raw seismic data, referred to as Rm_{raw} and RE_{raw} , were also used to assess coal burst risks. Figure 7-7 shows the daily event counts in burst damage zones in LW250105 assessed by Rm_{reinf} and Rm_{raw} . Ten coal bursts have Rm_{reinf} larger than 0.5, accounting for 63% of the total (10 of 16), while 8 coal burst damage are located in the zones with Rm_{raw} larger than 0.5, constituting 50% of the total (8 of 16). It indicates that Rm_{reinf} has a higher correlation with the coal burst damage than Rm_{raw} . However, similar Rm_{reinf} and Rm_{raw} are present in the burst damage zones when their values are larger than 0.7. Such characteristics imply that Rm_{reinf} has limited effect in improving the accuracy of assessing coal burst risks.

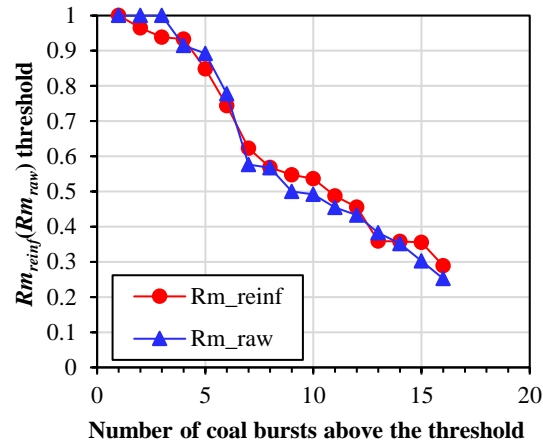


Figure 7-7 Number of coal bursts in LW250105 above different thresholds of Rm_{reinf} (red) and Rm_{raw} (blue)

Figure 7-8 shows the daily seismic energy in burst damage zones in LW250105 assessed by RE_{reinf} and RE_{raw} . Compared with RE_{raw} , RE_{reinf} shows stronger correlations with coal burst damage. Two-thirds (69%) of the coal bursts (11 of 16) occurred in the high RE_{reinf} zone (>0.8). In contrast, only 5 coal bursts were located in the zone with $RE_{raw} >0.8$, which constitutes 31% of the total (5 of 16). It indicates that by using the reinforced seismic data, daily seismic energy analysis can significantly increase the accuracy in forecasting coal burst risks.

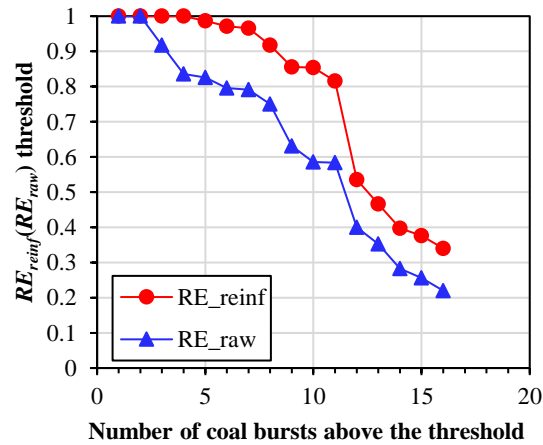


Figure 7-8 Number of coal bursts in LW250105 above different thresholds of RE_{reinf} (red) and RE_{raw} (blue)

According to Eq. (7-6), the efficiency of using Rm_{reinf} and RE_{reinf} to predict coal burst hazards in LW250105 was calculated at different thresholds. Figure 7-9 shows the hazard prediction efficiency when the Rm_{reinf} and RE_{reinf} thresholds vary between 0.1 to 0.9. In the figure, the blue dots at a given threshold represent the burst hazard prediction efficiency for the 16 coal bursts with damage located in the *PDZ*, and the red cross is the average efficiency for all 16 cases at that threshold. In Figure 7-9a, the hazard prediction efficiency using Rm_{reinf} has a general rising trend when the Rm_{reinf} threshold increases from 0.1 to 0.9. The prediction efficiency is larger than 0.2 when the Rm_{reinf} threshold is 0.3, and the maximum approaches 0.36 when Rm_{reinf} is 0.9. Similar to Rm_{reinf} , the burst hazard prediction efficiency using RE_{reinf} shown in Figure 7-9b also has a rising trend with the increase of the RE_{reinf} thresholds. The burst hazard prediction efficiency is larger than 0.3 when the RE_{reinf} threshold is larger than 0.7. The results indicate that the spatial variation of seismicity using reinforced seismic data can achieve more than 0.3 in burst hazard prediction efficiency.

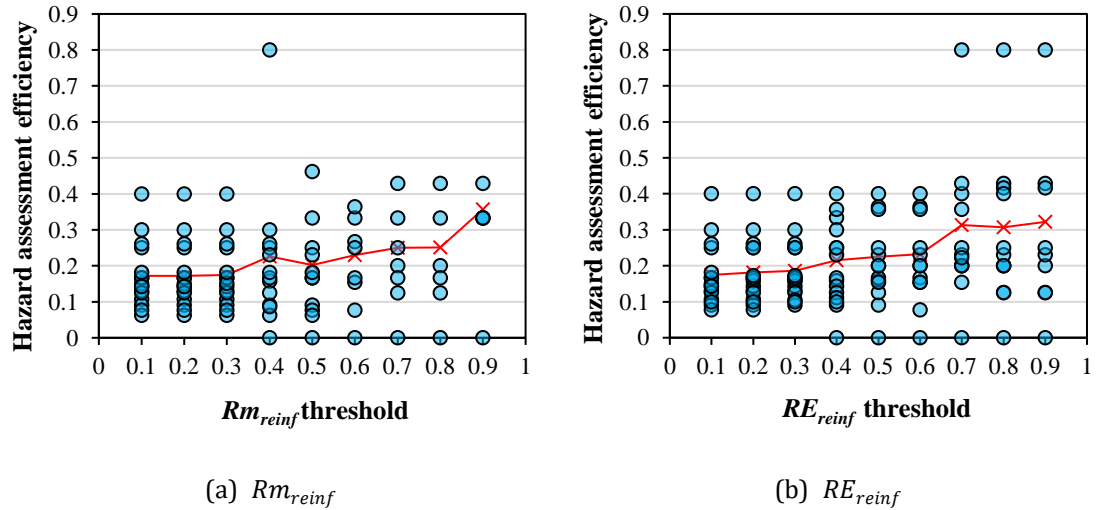


Figure 7-9 Coal burst prediction efficiency using Rm_{reinf} (a) and RE_{reinf} (b) with different thresholds. Each blue dot is the prediction efficiency for one coal burst case at a given Rm_{reinf} or RE_{reinf} threshold, and red line is the average prediction efficiency at different Rm_{reinf} or RE_{reinf} thresholds.

To demonstrate the improvement from using reinforced seismic data, the hazard prediction efficiency at different Rm_{raw} (RE_{raw}) thresholds was calculated in LW250105, which is shown in Figure 7-10. Compared to Rm_{reinf} and RE_{reinf} , Rm_{raw} and RE_{raw} have downward trends in burst hazard prediction efficiency with the increase of the Rm_{raw} (RE_{raw}) thresholds. Also, the burst hazard prediction efficiencies of Rm_{raw} and RE_{raw} are much lower than that of Rm_{reinf} and RE_{reinf} , and their average values fluctuate at 0.1. According to Eq. (7-6), there are two reasons for such phenomena: (1) the PDZ identification adopted in the reinforced seismic data narrows down the size of the high-risk zones, which yields a smaller L_k , and (2) the reinforced seismic data have a stronger correlation with the coal burst damage than the raw seismic data, which results in a higher $L_{damage(k)}$.

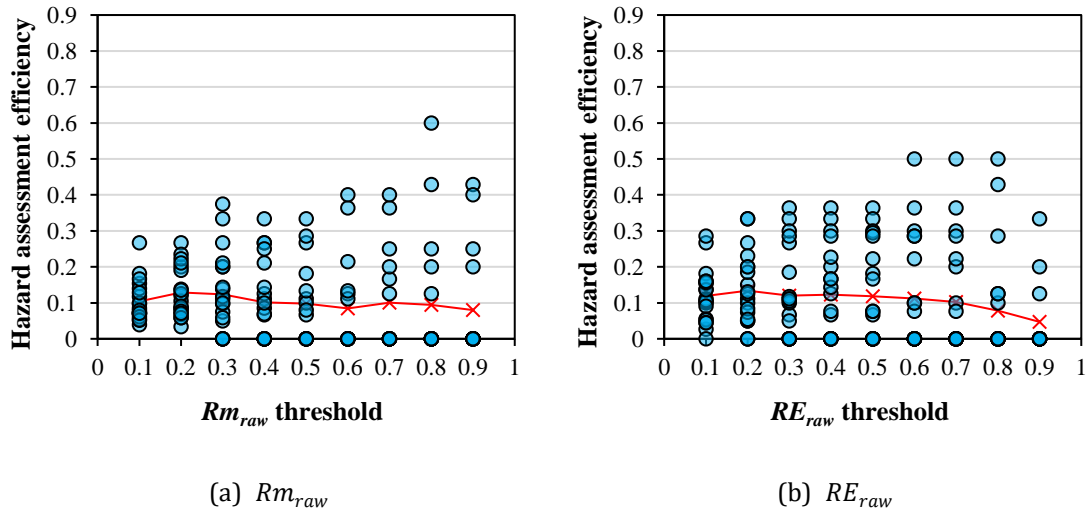


Figure 7-10 Coal burst prediction efficiency using Rm_{raw} (a) and RE_{raw} (b) with different thresholds. Each blue dot is the prediction efficiency for one coal burst case at a given Rm_{raw} or RE_{raw} threshold, and red line is the average prediction efficiency at different Rm_{raw} or RE_{raw} thresholds.

To identify coal burst risk zones using reinforced seismic data, the Rm_{reinf} (RE_{reinf}) threshold should be determined which can balance the accuracy and efficiency in predicting coal burst hazards. Similar to the R_{NPCE} in Section 5.4, only the accuracy and efficiency of hazard predictions in the space domain were

investigated. Therefore, the Rm_{reinf} (RE_{reinf}) threshold with higher accuracy and efficiency indicates a lower false positive and false negative. In this study, the multiplication of the accuracy and efficiency at a given Rm_{reinf} (RE_{reinf}) threshold, referred to as AmE , is used as an indicator to determine the optimal threshold. A higher value of AmE indicates a better accuracy and efficiency of using reinforced seismic data for hazard prediction at the corresponding Rm_{reinf} (RE_{reinf}) threshold. Figure 7-11 and Figure 7-12 show the accuracy and efficiency of using Rm_{reinf} and RE_{reinf} in predicting coal burst hazard, respectively. Figure 7-11 implies that the optimal threshold for Rm_{reinf} is 0.4 with the AmE at the maximum of 0.17, which can achieve 0.75 accuracy and 0.23 efficiency. Compared with Rm_{reinf} , RE_{reinf} has the optimal threshold of 0.7 with a higher AmE (0.22), which gives 0.69 accuracy and 0.31 efficiency. It suggests that RE_{reinf} generally has a better performance than Rm_{reinf} in coal burst hazard prediction. One main reason is that seismic noises may have more impact on event counts than seismic energy. Seismic noises are the seismic events which are unrelated to rock mass response to mining activities, such as equipment operating noise, drilling and blasting. These seismic noises commonly have lower seismic energy and lower detection probabilities. Therefore, the number of seismic noises in the Rm_{reinf} can be significantly increased after applying PDE correction, which intensifies the adverse impact of seismic noises in the event count analysis. In contrast, RE_{reinf} is less affected by the seismic noises as their energy only constitutes a minor fraction of the total energy even after PDE correction. Thus, RE_{reinf} can produce more reliable prediction for coal burst hazards than Rm_{reinf} .

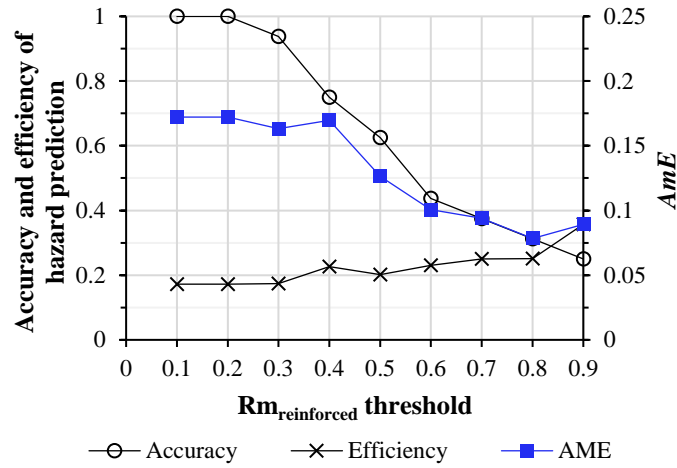


Figure 7-11 Accuracy and efficiency of using $Rm_{reinforced}$ in predicting coal burst hazard with different thresholds

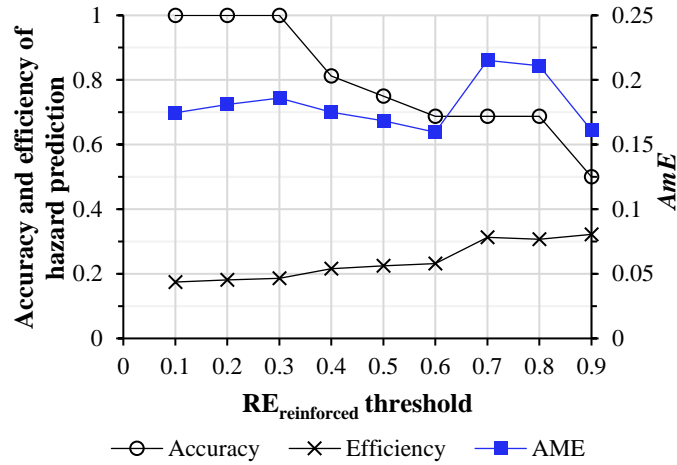


Figure 7-12 Accuracy and efficiency of using $RE_{reinforced}$ in predicting coal burst hazard with different thresholds

7.3.3 Guidelines for method application

Section 7.3 proved that $RE_{reinforced}$ is the optimal index to provide both high accuracy and efficiency in assessing coal burst risks in LW250105. The roadway with $RE_{reinforced} > 0.7$ is suggested as the high-risk zone, where 69% of the coal bursts have occurred in PDZ , which can be predicted with the maximum accuracy and efficiency. Compared with the high-risk zone, the roadway zone with $RE_{reinforced} < 0.7$ shows a lower burst risk and a reduced hazard prediction performance in accuracy and

efficiency. Therefore, the roadway zone with $RE_{reinf} < 0.7$ is suggested as the medium-risk zone where 31% of the coal bursts have occurred in *PDZ*. For the roadway zone out of *PDZ*, i.e. the roadway zone with no RE_{reinf} values, a low-risk level is suggested because 15% burst cases occurred there (see Section 7.3.1). When applying the proposed method in other mines, the optimal RE_{reinf} threshold can be determined by back analysing historical high-energy seismic events to find the RE_{reinf} with the maximum AmE .

It is ideal to use strong supports and take stress-relief measures in all the risky zones. However, burst hazard management in field practice has to balance the seismic hazard with the budget available for burst control. Therefore, the high-risk zone identified by RE_{reinf} should be the first priority for burst control, where a relatively higher accuracy and efficiency can be achieved in assessing coal burst risks. However, for burst-prone mines that have experienced several intensive coal bursts, both high-risk and medium-risk zones, i.e. the *PDZ* zone, should undertake essential burst control to maximise the hazard prediction accuracy for safe production. Also, as discussed in Section 5.5, seismic methods may not fully assess hazard potential due to the limited detection range of seismic monitoring in mines. Therefore, for burst risks in the low-risk zone, i.e. the zone outside *PDZ*, other non-seismic techniques should be used as a supplement for a more reliable hazard assessment.

7.4 Summary

To achieve enhanced performance of spatial variation of seismicity in predicting coal burst hazards in LW250105, this chapter proposed a method to reinforce raw seismic data, which can improve data quality in terms of location errors and detection probabilities. In this method, the potential damage zone (*PDZ*) was first identified by the modified *NPCE* analysis to reduce the size of the high-risk zones in the longwall. Compared with the *NPCE* analysis in Chapter 5, the modified *NPCE*

analysis records the maximum historical R_{NPCE} ahead of the longwall face, which can cover more zones that are susceptible to impending coal burst damage. Within the PDZ , the possible event counts and seismic energy in the longwall were calculated by using reinforced seismic data after correcting the corresponding location errors and detection probabilities. Compared with using raw seismic data, the spatial variation degree of seismic energy using reinforced seismic data, RE_{reinf} , has been proven to have a higher correlation with the impending coal burst hazards. In contrast, a limited improvement on the correlation with coal burst hazards was made by Rm_{reinf} , which is the spatial variation degree of event counts using reinforced seismic data. Therefore, it is more suitable to use RE_{reinf} as a daily index for coal burst risk assessment. In LW250105, RE_{reinf} of 0.7 is determined as the optimal threshold for identifying coal burst hazards, which can achieve 0.69 prediction accuracy and 0.31 efficiency. When the method is applied in other mines, the RE_{reinf} threshold can be determined by back analysing historical high-energy seismic events.

Chapter 8. Conclusions and recommendations

The main objective of this thesis was to investigate seismic impacts on dynamic failures and improve seismic data quality in seismic analyses when assessing seismic hazards in underground mines. The literature review in Chapter 2 demonstrated the role of seismic impacts in triggering burst damage and the importance of seismic information in assessing hazard potential. Based on the overview of the case study longwall, Chapter 2 comprehensively analysed the ground motion characteristics of seismic events and their relationship with coal burst damage. Chapter 5 to Chapter 7 analysed the location errors and detection probability of the case study seismic monitoring system. The analysis results were further used to correct seismic data to be applied in seismic methods to improve the performance in assessing hazard potential. Section 8.1 summarises the main findings and contribution of each chapter and Section 8.2 makes recommendations for further research.

8.1 Conclusions

From the literature review in Chapter 2 and the case study site overview in Chapter 2, the main conclusions are:

- According to the damage mechanism, coal bursts and rockbursts can be classified as direct burst or indirect burst. The excessive strain energy released in the loading environment is the main energy source for both burst types. Seismic energy transmitted via strong ground motions is the additional energy source for indirect bursts.
- The studied longwall was exposed to significant coal burst risks. The large mining height and caving height caused an elevated abutment stresses ahead of the longwall face. Also, it is postulated that the coal to be extracted in LW250105 was under significant side abutment stresses

on the goaf side due to the narrow, 6 m wide rib pillar between the tailgate and goaf.

- In the studied longwall, the zone within 80 m ahead of the longwall face had peak event counts and seismic energy release, where about half of the burst damage occurred. Several burst damage zones are located hundreds of metres away from the longwall face, which may be attributed to high stress concentration around undetected geological structures.

Based on the investigations on the ground motion characteristics in Chapter 2, the main conclusions are:

- Ground motions in the near-field zone of the seismic events have an overall much higher intensity than those in the far-field zone.
- Coal bursts have lower intensities on ground motions than rockbursts. However, for the seismic events at the same energy level, the induced ground motion in coal mines can be much higher than that in hard rock mines.
- Most ground motions only generate negligible dynamic impacts on roadways. Coal bursts are usually triggered when the coal and rock mass is already critically stressed. Some significant ground motions may contribute to producing considerable stress increment and initiating dynamic failure.
- The roadway zones that have experienced more cumulative damage from past intensive ground motions have a higher possibility of incurring coal burst damage.

From the location error characteristics in the longwall and the modified seismic clustering method in Chapter 5, it is concluded that:

- Different distributions of location errors occur in the panel when the geophone layout is modified. The patterns of location errors have strong anisotropic characteristics.
- The lowest location error of approximately 20 m is located between 50 to 300 m ahead of the longwall face. Location errors of more than 80 m can be detected in the goaf zone and further than 300 m ahead of the longwall face, where geophone coverage is insufficient.
- After considering location errors, the proposed *NPCE* analysis can provide 2–5 times more seismic clustering information and more robust results than the conventional clustering analyses. *NPCE* analysis can achieve 65% accuracy and 26% efficiency using the optimised threshold for risk identification.

Chapter 6 investigated the characteristics of the seismic data integrity in the longwall. It is that:

- Geophones have various capabilities to detect seismic events with different hypocentral distances and energy magnitudes. The zone surrounded by geophones in the longwall has the highest detection probability.
- The seismic monitoring system shows a better detection capability for events with higher energy magnitudes. Compared with the distant geophones that are far from the longwall, roadway geophones close to the longwall face are more capable of capturing low energy seismic events.

- After corrections by applying the *PDE* method, seismic data integrity is improved, with up to twice the event counts and more intensive energy released in front of the longwall face.
- A robust calculation on the detection probability of the seismic monitoring system (*PE*) needs at least three weeks of seismic data collection. After the first three weeks, all *PE* results present similarities no less than 0.9 before the relocation of geophones.

Chapter 7 proposed the concept of “reinforced seismic data” aiming to improve the data quality in analysing the variation of seismicity for burst hazard assessment. The main conclusions are:

- The potential damage zone (*PDZ*) can identify the area where seismic events are related to the impending burst damage. Most (80%) of the burst damage zones are located in the *PDZ*.
- By considering the location errors and detection probabilities of the seismic monitoring system, the reinforced seismic data improves the performance of using a spatial variation of seismicity to assess coal burst risks. The normalised seismic energy using reinforced data (RE_{reinf}) has a strong correlation with the coal burst damage, which can be an effective precursor to assess the hazard potential.
- The optimal RE_{reinf} threshold to identify high-risk zones is determined as 0.7, which can achieve 69% accuracy and 31% efficiency in assessing coal bursts in the *PDZ*.
- Three risk levels are determined based on the RE_{reinf} index: high-risk zone with $RE_{reinf} > 0.7$, medium-risk zone with $RE_{reinf} < 0.7$ but

within the *PDZ*, and low-risk zone located outside the *PDZ*. The identified high-risk zone has the optimal accuracy and efficiency in assessing coal burst risks, which can aid decision-making for burst control and prevention in field practice. A RE_{reinf} threshold <0.7 may induce higher accuracy but lower efficiency in hazard prediction. Inversely, A RE_{reinf} threshold >0.7 may induce higher efficiency but lower accuracy in assessing coal burst risks.

8.2 Recommendations for future research

The research of this thesis provides insights into the dynamic impacts of mining-induced seismicity and the improvement of seismic data quality used for assessing dynamic failure risks in underground coal mines. However, several issues were also encountered during the study which need further investigation. The issues and the recommendations are:

- The effect of heterogenic mining environments

All proposed methods in this research are based on a homogeneous mining environment with a constant wave velocity. However, real mining environments are highly heterogenic with many voids, backfilled zones and highly fractured zones. Seismic waves in a heterogenic medium have complex propagating pathways and attenuation characteristics due to wave scattering, reflection and refraction. Thus, it is hard for a geophone to detect seismic signals from any seismic source events, even if the events have high magnitudes and/or low hypocentral distances. It may cause unreliable results and bias when assessing location errors and the detection probability of the seismic monitoring system. Therefore, it is recommended future studies investigate the heterogeneity of the mining environment, especially the material properties over the pathway of seismic wave transport.

- Seismic data captured by uniaxial geophones

This study is based on the seismic data purely recorded by a uniaxial geophone system. Most underground coal mines in China are largely dependent on seismic monitoring systems with uniaxial geophones only. This situation is caused by a series of issues such as intrinsic safety requirements, weak or noisy seismic signals and difficulties of installing portable sensors in fast-moving coal mining conditions. In contrast to using triaxial sensors to capture 3D waveforms, uniaxial sensors can only record seismic vibration in one direction. This intrinsic limit of the uniaxial sensor makes it difficult to calculate accurate seismic energy. Also, as P-, SH- and SV-waves cannot be distinguished by uniaxial seismic data, it is challenging to conduct seismic analysis on source mechanisms and then use that to infer geological discontinuities. Therefore, it is recommended future studies investigate the proposed methods by using triaxial seismic data monitored in mine sites.

- Artificial influences on mining-induced seismicity

Although the *PDE* method proposed in this study can accept all types of seismic sources, the existence of artificial events, such as blasting and drilling, still limits the accuracy of seismic methods in assessing dynamic failure risks. For example, the seismic clustering analysis may mis-locate an invisible geological structure near the mine opening where blasting or drilling work is undertaken. Many seismic studies in hard rock mines have filtered out artificial events before the analysis, but research in coal mines has rarely been aware of such a problem. Therefore, it is recommended further studies focus on developing techniques to identify artificial events and further refine the seismic data catalogue in coal mines. Apart from that, as seismic events are the response of rock mass to mining activities, the mining speed also controls the rate of mining-induced seismicity. In this study, normalised parameters are adopted as a simple way to reduce the influence of mining speed on the seismic indexes, but it may still induce bias on hazard potential evaluations. Therefore,

future studies should link the rate of seismicity with mining speed and consider that in the seismic methods.

References

- Aki K (1965) Maximum likelihood estimate of b in the formula $\log N = a - bM$ and its confidence limits. *Bulletin of the Earthquake Research Institute, University of Tokyo* 43:237-239.
- Bai J, Shen W, Guo G, Wang X, Yu Y (2015) Roof deformation, failure characteristics, and preventive techniques of gob-side entry driving heading adjacent to the advancing working face. *Rock Mechanics and Rock Engineering* 48:2447-2458.
- Bender B (1983) Maximum likelihood estimation of b values for magnitude grouped data. *Bulletin of the Seismological Society of America* 73:831-851.
- Bieniawski ZT (1970) Time-dependent behaviour of fractured rock. *Rock Mechanics* 2:123-137.
- Blake W, Hedley DG (2003) Rockbursts: case studies from North American hard-rock mines. Society for Mining, Metallurgy, and Exploration, Colorado.
- Boatwright J (1988) The seismic radiation from composite models of faulting. *Bulletin of the Seismological Society of America* 78:489-508.
- BP (2020) Statistical review of world energy. <https://www.bp.com/content/dam/bp/business-sites/en/global/corporate/pdfs/energy-economics/statistical-review/bp-stats-review-2020-full-report.pdf>.
- Brady BT (1974) Seismic precursors before rock failures in mines. *Nature* 252:549-552.
- Brady BT (1977) An investigation of the scale invariant properties of failure. *International Journal of Rock Mechanics and Mining Sciences & Geomechanics Abstracts* 14:121-126.
- Brady BT (1978) Prediction of failures in mines: an overview. United States Department of the Interior.
- Brady BT, Leighton F (1977) Seismicity anomaly prior to a moderate rock burst: a case study. *International Journal of Rock Mechanics and Mining Sciences & Geomechanics Abstracts* 14:127-132.
- Bräuner G (2017) Rockbursts in coal mines and their prevention. A.A.Balkema, Rotterdam.
- Brune JN (1970) Tectonic stress and the spectra of seismic shear waves from earthquakes. *Journal of Geophysical Research: Atmospheres* 75:4997-5009.
- Bukowska M (2013) Post-peak failure modulus in problems of mining geo-mechanics. *Journal of Mining Science* 49:731-740.
- Cai M, Kaiser PK (2018) Rockburst Support Reference Book, Volume I: Rockburst phenomenon and support characteristics. MIRARCO, Canada.

- Cai W, Bai X, Si G, Cao W, Gong S, Dou L (2020a) A monitoring investigation into rock burst mechanism based on the coupled theory of static and dynamic stresses. *Rock Mechanics and Rock Engineering* 53:5451-5471.
- Cai W, Dou L, Si G, Cao A, Gong S, Wang G, Yuan S (2019) A new seismic-based strain energy methodology for coal burst forecasting in underground coal mines. *International Journal of Rock Mechanics and Mining Sciences* 123:104086.
- Cai W, Dou L, Si G, Cao A, He J, Liu S (2016) A principal component analysis/fuzzy comprehensive evaluation model for coal burst liability assessment. *International Journal of Rock Mechanics and Mining Sciences* 81:62-69.
- Cai W, Dou L, Si G, Hu Y (2020b) Fault-Induced coal burst mechanism under mining-induced static and dynamic stresses. *Engineering* 7:687-700.
- Cao A, Dou L, Wang C, Yao X, Dong J, Gu Y (2016) Microseismic precursory characteristics of rock burst hazard in mining areas near a large residual coal pillar: a case study from Xuzhuang Coal Mine, Xuzhou, China. *Rock Mechanics and Rock Engineering* 49:4407-4422.
- Cao A, Gao SS (2002) Temporal variation of seismic b - values beneath northeastern Japan island arc. *Geophysical Research Letters* 29:48-41-48-43.
- China University of Mining and Technology (2016) Huating coal mine 5# coal seam burst proneness identification report. China University of Mining and Technology.
- Cichowicz A (2001) The meaningful use of peak particle velocity at excavation surface for the optimisation of the rockburst support criteria for tunnels and stopes. Mine Health and Safety Council, Johannesburg.
- Cook NGW (1963) The seismic location of rockbursts. In: *Proceedings of the Fifth rock Mechanics Symposium*. Pergamon Oxford, pp 493-516.
- Cook NGW (1965) A note on rockbursts considered as a problem of stability. *Journal of the Southern African Institute of Mining and Metallurgy* 65:437-446.
- Cook NGW (1976) Seismicity associated with mining. *Engineering Geology* 10:99-122.
- Cortolezzis DM (2018) Characterization of seismic sources using sequential spatial clustering and fractal dimension. PhD Thesis, Laurentian University of Sudbury.
- Cortolezzis DM, Hudyma MR (2018) Application of sequential spatial clustering and fractal dimension to caving seismic event parameters of time, distance, and intensity. In: *Proceedings of the Fourth International Symposium on Block and Sublevel Caving*. Australian Centre for Geomechanics, pp 799-814.
- Coulson AL (2009) Investigation of the pre to post peak strength state and behaviour of confined rock masses using mine induced microseismicity. PhD Thesis, University of Toronto.

- Debski W (2015) Using meta-information of a posteriori Bayesian solutions of the hypocentre location task for improving accuracy of location error estimation. *Geophysical Journal International* 201:1399-1408.
- Dębski W, Klejment P (2016) The new algorithm for fast probabilistic hypocenter locations. *Acta Geophysica* 64:2382-2409.
- Diederichs M (2014) When does brittle failure become violent? Spalling and rockburst characterization for deep tunneling projects. In: *Proceedings of the World Tunneling Conference*. pp 1-8.
- Dou L, Cao A, Gong S, Cai W (2016) *Mining geophysics and vibration*. China University of Mining and Technology Press, Xuzhou, China.
- Dubiński J, Lurka A, Mutke G (2013) Seismic hazard assessment using bendray and rectilinear passive tomography in the Polkowice-Sieroszowice copper mine. In: *Proceedings of 8th International Symposium on Rockburst and Seismicity in Mines*. pp 1-7.
- Dubinski J, Mutke G (1997) Characteristics of near-field peak velocity in the Upper Silesian Coal Mines. In: *Proceedings of 4th International Symposium on Rockburst and Seismicity in Mines, Kraków, Poland*. Balkema, pp 343-347.
- Dubiński J, Mutke G (1996) Characteristics of mining tremors within the near-wave field zone. *Induced Seismic Events*. Birkhäuser Basel, pp 249-261.
- Eberhardt E, Stead D, Stimpson B (1999) Quantifying progressive pre-peak brittle fracture damage in rock during uniaxial compression. *International Journal of Rock Mechanics and Mining Sciences* 36:361-380.
- Ester M, Kriegel H-P, Sander J, Xu X (1996) A density-based algorithm for discovering clusters in large spatial databases with noise. In: *KDD-96 Proceedings*. vol 34. pp 226-231.
- Falmagne V (2002) *Quantification of rock mass degradation using micro-seismic monitoring and applications for mine design*. PhD Thesis, Queen's University.
- Feng X, Xiao Y, Feng G (2012) Mechanism, warning and dynamic control of rockburst evolution process. In: *ISRM Regional Symposium-7th Asian Rock Mechanics Symposium*. OnePetro.
- Galvin J (2016) *Ground engineering-principles and practices for underground coal mining*. Springer.
- Geiger L (1912) Probability method for the determination of earthquake epicenters from the arrival time only. *Bulletin of St Louis University* 8:56-71.
- Georgoulas G, Konstantaras A, Katsifarakis E, Stylios CD, Mavroulakis E, Vachtsevanos GJ (2013) "Seismic-mass" density-based algorithm for spatio-temporal clustering. *Expert Systems with Applications* 40:4183-4189.

- Gibowicz S, Harjes H-P, Schäfer M (1990) Source parameters of seismic events at Heinrich Robert mine, Ruhr Basin, Federal Republic of Germany: evidence for nondouble-couple events. *Bulletin of the Seismological Society of America* 80:88-109.
- Gibowicz SJ, Kijko A (1994) An introduction to mining seismology. Polish Academy of Sciences: Warsaw, Poland.
- Gibowicz SJ, Lasocki S (2001) Seismicity induced by mining: Ten years later. *Advances in Geophysics* 44:39-181.
- Glazer S (2018) Mine seismology: seismic warning concept. Springer.
- Gong S, Dou L, Cao A, He H, Du T, Jiang H (2010a) Study on optimal configuration of seismological observation network for coal mine. *Chinese Journal of Geophysics* 53:457-465 (in Chinese).
- Gong S, Dou L, Ma X, Liu j (2010b) The method to identify the optimal channel numbers for increasing the location accuracy of microseismic events in coal mine. *Journal of China Coal Society* 35:2017-2021 (in Chinese).
- Gu R (2013) Distinct element model analyses of unstable failures in underground coal mines. PhD thesis, Colorado School of Mines.
- Gutenberg B, Richter CF (1944) Frequency of earthquakes in California. *Bulletin of the Seismological Society of America* 34:185-188.
- Hebblewhite B, Galvin J (2017) A review of the geomechanics aspects of a double fatality coal burst at Austar Colliery in NSW, Australia in April 2014. *International Journal of Mining Science Technology* 27:3-7.
- Hedley DG (1992) Rockburst handbook for Ontario hardrock mines. Canmet.
- Hudyma MR (2008) Analysis and interpretation of clusters of seismic events in mines. University of Western Australia.
- Iannacchione AT, Tadolini SC (2016) Occurrence, predication, and control of coal burst events in the US. *International Journal of Mining Science Technology* 26:39-46.
- International Energy Agency (2020) Coal 2020. Analysis and forecast to 20205. <https://www.iea.org/reports/coal-2020>.
- Ishimoto M (1936) Observations of earthquakes registered with the microseismograph constructed recently. *Journal of Bulletin Earthquake Research Institute, University of Tokyo* 17:443-478.
- Jaeger JC, Cook NGW, Zimmerman R (2009) Fundamentals of rock mechanics. John Wiley & Sons.
- Jager A, Ryder J (1999) A handbook on rock engineering practice for tabular hard rock mines. Safety in Mines Research Advisory Committee: Johannesburg.

- Jia C, Luan H, Chen Z (2014) Supporting technique of gob-side entry driving in asymmetric island coal face in deep and its application. *Electronic Journal of Geotechnical Engineering* 19:Z3.
- Jiang Y, Pan Y, Jiang F, Dou L, Ju Y (2014) State of the art review on mechanism and prevention of coal bumps in China. *Journal of China Coal Society* 39:205-213 (in Chinese).
- Ju W, Zheng J, Wei D, Sun L, Li W (2019) Study on the causes and control technology about the coal bump in multi-layered mining roadway in steep-thick coal seams. *Journal of Mining & Safety Engineering* 36:280-289.
- Kaiser PK (1996) *Canadian Rockburst Support Handbook*: 1996. Geomechanics Research Centre, Canada.
- Kaiser PK, Cai M (2013a) Critical review of design principles for rock support in burst-prone ground—time to rethink! In: *Proceedings of the 7th International Symposium on Ground Support in Mining and Underground Construction*, Australia. Australian Centre for Geomechanics, pp 3-37.
- Kaiser PK, Cai M (2013b) Keynote lecture: rockburst damage mechanisms and support design principles. In: Malovichko A, Malovichko D (eds) *Proceedings of the 8th International Symposium on Rockbursts and Seismicity in Mines*. Geophysical Survey of Russian Academy of Sciences, pp 349-370.
- Kaiser PK, Cai M (2013c) Rockburst damage mechanisms and support design principles. In: *Proceedings of the 8th International Symposium on Rockbursts and Seismicity in Mines*. Saint-Petersburg: Moscow, pp 349-370.
- Kaiser PK, MacCreath D, Tannant D (1996a) *Canadian rockburst support handbook: prepared for sponsors of the Canadian rockburst research program 1990-1995*. Geomechanics Research Centre.
- Kaiser PK, Maloney SM (1997) Scaling laws for the design of rock support. *Pure and Applied Geophysics* 150:415-434.
- Kaiser PK, McCreath DR, Tannant DD (1996b) *Rockburst research handbook vol 2*. CAMIRO Mining Division, Mining Research Directorate.
- Kaiser PK, Vasak P, Suorineni F, Thibodeau D (2005) New dimensions in seismic data interpretation with 3-D virtual reality visualization for burst-prone mines. In: *Proceedings of 6th International Symposium on Rockburst and Seismicity in Mines*, Australia. Australian Centre for Geomechanics, pp 33-45.
- Karri NA, Ansari MY, Pathak A (2018) Identification of seismic zones of India using DBSCAN. In: *2018 International Conference on Computing, Power and Communication Technologies (GUCON)*. IEEE, pp 65-69.
- Kijko A, Sciocatti M (1995) Optimal spatial distribution of seismic stations in mines. *International Journal of Rock Mechanics and Mining Sciences & Geomechanics Abstracts* 32:607-615.

- Leśniak A (2015) Seismic network configuration by reduction of seismic source location errors. *International Journal of Rock Mechanics and Mining Sciences* 80:118-128.
- Leśniak A, Pszczoła G (2008) Combined mine tremors source location and error evaluation in the Lubin Copper Mine (Poland). *Tectonophysics* 456:16-27.
- Li N, Ge M, Wang E (2014) Two types of multiple solutions for microseismic source location based on arrival-time-difference approach. *Natural Hazards* 73:829-847.
- Li X, Wang E, Li Z, Liu Z, Song D, Qiu L (2016) Rock burst monitoring by integrated microseismic and electromagnetic radiation methods. *Rock Mechanics and Rock Engineering* 49:4393-4406.
- Liu F, Ma T, Chen F (2018) Prediction of rockburst in tunnels at the Jinping II hydropower station using microseismic monitoring technique. *Tunnelling and Underground Space Technology* 81:480-493.
- Madariaga R (1976) Dynamics of an expanding circular fault. *Bulletin of the Seismological Society of America* 66:639-666.
- Mark C (2016) Coal bursts in the deep longwall mines of the United States. *International Journal of Coal Science and Technology* 3:1-9.
- Martin CD (1993) The strength of massive Lac du Bonnet granite around underground openings. PhD Thesis, University of Manitoba.
- Martin CD, Young RP (1993) The effect of excavation-induced seismicity on the strength of Lac du Bonnet granite. In: *Proceedings of the 3rd International Symposium on Rockbursts and Seismicity in Mines*. Balkema, pp 367-371.
- Mason I (1981) Algebraic reconstruction of a two-dimensional velocity inhomogeneity in the High Hazles seam of Thoresby colliery. *Geophysics* 46:298-308.
- McGarr A (1976) Seismic moments and volume changes. *Journal of Geophysical Research* 81:1487-1494.
- McGarr A (1991) Observations constraining near-source ground motion estimated from locally recorded seismograms. *Journal of Geophysical Research: Solid Earth* 96:16495-16508.
- McGarr A (1993) Keynote address: Factors influencing the strong ground motion from mining-induced tremors. In: Young RP (ed) *Proceedings of the 3rd International Symposium on Rockbursts and Seismicity in Mines*. Balkema, pp 3-12.
- McGarr A (1994) Some comparisons between mining-induced and laboratory earthquakes. *Pure and Applied Geophysics* 142:467-489.
- McGarr A (1997) A mechanism for high wall-rock velocities in rockbursts. *Pure and Applied Geophysics* 150:381-391.
- McGarr A (1999) On relating apparent stress to the stress causing earthquake fault slip. *Journal of Geophysical Research: Solid Earth* 104:3003-3011.

- McGarr A, Green R, Spottiswoode S (1981) Strong ground motion of mine tremors: some implications for near-source ground motion parameters. *Bulletin of the Seismological Society of America* 71:295-319.
- Mendecki AJ (1993) Keynote address: Real time quantitative seismology in mines. In: *Proceedings of the 6th International Symposium on Rockburst and Seismicity in Mines*, Rotterdam. Balkema, pp 287-295.
- Mendecki AJ (1996) *Seismic monitoring in mines*. Chapman & Hall, London.
- Mendecki AJ (2016) *Mine seismology reference book: seismic hazard*. Institute of Mine Seismology.
- Mignan A, Werner M, Wiemer S, Chen C, Wu Y (2011) Bayesian estimation of the spatially varying completeness magnitude of earthquake catalogs. *Bulletin of the Seismological Society of America* 101:1371-1385.
- Milev A, Spottiswoode S, Noble B, Linzer L, Van Zyl M, Daehnke A, Acheampong E (2002) Meaningful use of peak particle velocities at excavation surfaces for the optimisation of the rockburst criteria for tunnels and stopes (GAP709). *Safety in Mines Research Advisory Committee*.
- Mutke G, Masny W, Prusek S (2016) Peak particle velocity as an indicator of the dynamic load exerted on the support of underground workings. *Acta Geodynamica et Geomaterialia* 4:367-378.
- Ogata Y, Katsura K (1993) Analysis of temporal and spatial heterogeneity of magnitude frequency distribution inferred from earthquake catalogues. *Geophysical Journal International* 113:727-738.
- Ortlepp W (1985) Rockbursts in South African gold mines: A phenomenological view: *Proc 1st International Congress on Rockbursts and Seismicity in Mines*, Johannesburg, Sept 1982 P165–178. Publ Johannesburg: SAIMM, 1984. In: *International Journal of Rock Mechanics and Mining Sciences & Geomechanics Abstracts*. vol 6. Pergamon, p 198.
- Ortlepp W (1993) High ground displacement velocities associated with rockburst damage. In: Young RP (ed) *Proceedings of the 3rd International Symposium on Rockburst and Seismicity in Mines*. AA.Balkema: Rotterdam, pp 101-106.
- Ortlepp W (1997) *Rock fracture and rockbursts: an illustrative study*. South African Institute of Mining and Metallurgy.
- Ortlepp W (2005) RaSiM comes of age—a review of the contribution to the understanding and control of mine rockbursts. In: *Proceedings of the 6th International Symposium on Rockburst and Seismicity in Mines*, Australia. Australian Centre for Geomechanics, pp 3-20.
- Ortlepp W, Stacey T (1994) Rockburst mechanisms in tunnels and shafts. *Tunnelling and Underground Space Technology* 9:59-65.

- Ouchterlony F, Nie S, Nyberg U, Deng J (1997) Monitoring of large open cut rounds by VOD, PPV and gas pressure measurements. *Fragblast* 1:3-26.
- Owen ML (2005) Calibrating a Semi-Quantitative Seismic Risk Model Using Rockburst Case Studies from Underground Metalliferous Mines. In: *Proceedings of 6th International Symposium on Rockburst and Seismicity in Mines, Australia*. Australian Centre for Geomechanics, pp 191-204.
- Patyńska R, Mirek A, Burtan Z, Pilecka E (2018) Rockburst of parameters causing mining disasters in Mines of Upper Silesian Coal Basin. In: *E3S Web of Conferences*. EDP Sciences, p 03005.
- Peng S (1973) Time-dependent aspects of rock behavior as measured by a servocontrolled hydraulic testing machine. *International Journal of Rock Mechanics and Mining Sciences & Geomechanics Abstracts* 10:235-246.
- Potvin Y, Hudyma MR (2001) Seismic monitoring in highly mechanized hardrock mines in Canada and Australia. In: *The Fifth International Symposium on Rockburst and Seismicity in Mines*. South African Institute of Mining and Metallurgy, pp 267-280.
- Ptáček J (2017) Rockburst in Ostrava-Karvina Coalfield. *Procedia Engineering* 191:1144-1151.
- Qian D, Sasaoka T, Shimada H, Wahyudi S, Tsedendorj A, Wang C, Matsui K (2014) Analysis of coal pillar width and stability control of gob-side entry driving in deep island coal face. In: *ISRM International Symposium-8th Asian Rock Mechanics Symposium*. OnePetro.
- Rezaei M (2016) Clustering validation. *Itä-Suomen Yliopisto*.
- Roberts MKC, Brummer RK (1988) Support requirements in rockburst conditions. *Journal of the Southern African Institute of Mining and Metallurgy* 88:97-104.
- Rorke A (1992) Measurement of the direct effects of preconditioning blasts. Monitored results from the first test blast. Internal report, prepared for D. Adams.
- Ryder JA, Jager AJ (2002) A textbook on rock mechanics for tabular hard rock mines. The Safety in Mines Research Advisory Committee, Johannesburg.
- Schorlemmer D, Woessner J (2008) Probability of detecting an earthquake. *Bulletin of the Seismological Society of America* 98:2103-2117.
- Shearer PM (2009) *Introduction to seismology*. Cambridge University Press, New York.
- Shimazaki K, Nakata T (1980) Time - predictable recurrence model for large earthquakes. *Geophysical Research Letters* 7:279-282.
- Singh H, Paudyal H, Shanker D, Panthi A, Kumar A, Singh V (2010) Anomalous seismicity and earthquake forecast in western Nepal Himalaya and its adjoining Indian region. *Pure and Applied Geophysics* 167:667-684.

- Srinivasan C, Arora S, Benady S (1999) Precursory monitoring of impending rockbursts in Kolar gold mines from microseismic emissions at deeper levels. *International Journal of Rock Mechanics and Mining Sciences* 36:941-948.
- Stec K (2007) Characteristics of seismic activity of the Upper Silesian Coal Basin in Poland. *Geophysical Journal International* 168:757-768.
- Tannant DD, McDowell GM, Brummer RK, Kaiser PK (1993) Ejection velocities measured during a rockburst simulation experiment. In: Young RP (ed) *Proceedings of the 3rd International Symposium on Rockburst and Seismicity in Mines*. pp 129-133.
- Utsu T (1965) A method for determining the value of "b" in a formula $\log n = a - bm$ showing the magnitude-frequency relation for earthquakes. *Geophysical bulletin of the Hokkaido University* 13:99-103.
- Van Aswegen G, Butler A (1993) Applications of quantitative seismology in South African gold mines. In: Young RP (ed) *Proceedings of the 3rd International Symposium on Rockbursts and Seismicity in Mines*. pp 261-266.
- Vardar O, Tahmasebinia F, Zhang C, Canbulat I, Saydam S (2017) A review of uncontrolled pillar failures. *Procedia Engineering* 191:631-637.
- Vasak P, Suorineni F, Kaiser PK, Thibodeau D (2004) Hazard map approach using space-time clustering analysis of mining-induced microseismicity. In: *Canadian Institute of Mining and Metallurgy Annual General Meeting*, Edmonton.
- Wagner H (1984) Support requirements for rockburst conditions. *Canadian Journal of Earth Sciences* 21:1410-1414.
- Wang C, Cao A, Zhu G, Jing G, Li J, Chen T (2017) Mechanism of rock burst induced by fault slip in an island coal panel and hazard assessment using seismic tomography: a case study from Xuzhuang colliery, Xuzhou, China. *Geosciences Journal* 21:469-481.
- Wang C, Si G, Zhang C, Cao A, Canbulat I (2021) Location error based seismic cluster analysis and its application to burst damage assessment in underground coal mines. *International Journal of Rock Mechanics and Mining Sciences* 143:104784.
- Wang G, Gong S, Dou L, Wang H, Cai W, Cao A (2018) Rockburst characteristics in syncline regions and microseismic precursors based on energy density clouds. *Tunnelling and Underground Space Technology* 81:83-93.
- Wesseloo J, Woodward KR, Pereira J (2014) Grid-based analysis of seismic data. *Journal of the Southern African Institute of Mining and Metallurgy* 114:815-822.
- Wiemer S, Wyss M (2000) Minimum magnitude of completeness in earthquake catalogs: Examples from Alaska, the western United States, and Japan. *Bulletin of the Seismological Society of America* 90:859-869.

- Woessner J, Wiemer S (2005) Assessing the quality of earthquake catalogues: Estimating the magnitude of completeness and its uncertainty. *Bulletin of the Seismological Society of America* 95:684-698.
- Woodward KR, Tierney SR (2017) Seismic hazard estimation using databases with bimodal frequency-magnitude behaviour. In: *Proceedings of the first international conference on underground mining technology*. Australian Centre for Geomechanics, pp 219-232.
- Woodward KR, Wesseloo J, Potvin Y (2017) The spatial and temporal assessment of clustered and time-dependent seismic responses to mining. In: *Proceedings of The Eighth International Conference on Deep and High Stress Mining*. pp 28-30.
- Woodward KR, Wesseloo J, Potvin Y (2018) A spatially focused clustering methodology for mining seismicity. *Engineering Geology* 232:104-113.
- Wu R, He Q, Oh J, Li Z, Zhang C (2018) A new gob-side entry layout method for two-entry longwall systems. *Energies* 11:2084.
- Xie H, Pariseau WG (1993) Fractal character and mechanism of rock bursts. In: *International Journal of Rock Mechanics and Mining Sciences & Geomechanics Abstracts*. vol 4. Elsevier, pp 343-350.
- Xu Y, Cai M (2017) Influence of strain energy released from a test machine on rock failure process. *Canadian Geotechnical Journal* 55:777-791.
- Yi X, Kaiser PK (1993) Mechanisms of rockmass failure and prevention strategies in rockburst conditions. In: Young RP (ed) *Proceedings of the 3rd International Symposium on Rockburst and Seismicity in Mines*. AA.Balkema: Rotterdam, pp 141-145.
- Zhang C, Canbulat I, Hebblewhite B, Ward CR (2017) Assessing coal burst phenomena in mining and insights into directions for future research. *International Journal of Coal Geology* 179:28-44.
- Zhang H, Ma C, Li T (2019) Quantitative evaluation of the “non-enclosed” microseismic array: A case study in a deeply buried twin-tube tunnel. *Energies* 12:2006.
- Zhou Y, Zhao J (2011) *Advances in rock dynamics and applications*. CRC Press.
- Zhu M, Wang L, Liu X, Zhao J (2018) Accurate identification of microseismic P-and S-phase arrivals using the multi-step AIC algorithm. *Journal of Applied Geophysics* 150:284-293.
- Zúñiga FR, Wyss M (1995) Inadvertent changes in magnitude reported in earthquake catalogs: Their evaluation through b-value estimates. *Bulletin of the Seismological Society of America* 85:1858-1866.